

# Contact Binary Stars in Survey Data

A *thesis submitted in partial fulfillment of the requirements of a degree of Bachelor of Arts in Physics at Pomona College*



Franklin M. Marsh  
*with advisor*  
Philip I. Choi, Ph.D.  
Professor of Astronomy  
Pomona College

May 1, 2017

## Abstract

We present the study of contact binary stars, using data from contemporary all-sky surveys. The contact binary is introduced as a binary system with two main-sequence components. The most common spectral types of contact binaries are F,G,K, and M, giving them temperatures ranging from 4000K to 8000K. The vast majority of contact binary systems have orbital periods ranging from 0.22 to 1.0 days, giving them the shortest orbital periods of two non-degenerate objects. Even though the two components of a contact binary have unequal masses (and in fact prefer to), they share a common photospheric envelope with a temperature that differs by less than  $\approx 100\text{K}$  across its surface [Webbink, 2003]. The isothermal nature of the envelope, (despite differing component masses) can only be maintained via energy transport from the more massive primary to the secondary, through the neck ( $L_1$  point) of the binary. It has been shown that for such a system to be stable, one of the components must be close to zero-age main-sequence, while the other must be close to terminal-age main-sequence. Due to their rapid rotation, contact binaries exhibit dramatic magnetic phenomena, such as starspots and flares.

In a published paper provided as an appendix to this thesis, we use data from the Catalina Real-Time Transient Survey (CRTS), and Sloan Digital Sky Survey (SDSS), to characterize a large sample of contact binary stars in visible wavelengths. We find that more than 2000 binaries exhibit a linear change in mean brightness over the 8-yr timespan of observations with at least  $3\sigma$  significance. We note that 25.9 per cent of binaries with convective outer envelopes exhibit a significant change in brightness, while only 10.5 per cent of radiative binaries exhibit a significant change in brightness. In 205 binaries (2.2 per cent), we find that a sinusoid model better describes the luminosity trend within the 8-yr observation timespan. For these binaries, we report the amplitudes and periods (as estimated using observed half-periods) of this sinusoidal brightness variation and discuss possible mechanisms driving the variation.

In our most recent work, we further refined techniques to ascertain changes in brightness of contact binaries in survey data. We find that the brightness changes are not uniform across orbital phase. For cool stars with deeper convective envelopes, the brightness changes of each of the components are found to be the most independent. We find that the convective layer depth strongly affects the way starspots form on contact binaries. For cooler binaries with deeper convective layers, we find that starspot formation on the two components is uncorrelated. For solar-temperature contact binaries with shallow convective layers, starspot formation on the two components is correlated. This suggests that in binaries with deep convective envelopes, the dynamo mechanisms for each of the components are independent, whereas for binaries with shallow convective envelopes, the dynamo mechanisms are related.

## Acknowledgments

First, I'd like to thank Dr. Thomas Prince, Dr. Ashish Mahabal, and Dr. Eric Bellm for being fantastic mentors and collaborators at the California Institute of Technology. I thank veterans of the field Slavek Rucinski and Andrej Prsa for their advice about studying these unique systems. I'd like to thank Jay Skuban, Tom and Edith Auchter, Charlie and Susie Klingel, and Darren Drake for fostering my love of astronomy. I'd like to thank Dr. Philip Choi for being a fantastic undergraduate advisor. Finally thank you to my mother Sarah, father John, and brother Elliott for all of their support.

# Contents

<b>1</b>	<b>Introduction</b>	<b>1</b>
<b>2</b>	<b>Theory</b>	<b>4</b>
2.1	Discovery . . . . .	4
2.2	The Main-Sequence Star . . . . .	6
2.3	The Main-Sequence Homology Relations . . . . .	9
2.4	ZAMS to TAMS . . . . .	9
2.5	Metallicity . . . . .	11
2.6	The Roche Potential . . . . .	11
2.7	The Geometrical Elements of Contact Binary Systems . . . . .	14
2.8	Thermal Equilibrium Models . . . . .	17
2.9	Interior Structure . . . . .	21
2.10	The Period-Color Relation . . . . .	26
2.11	Mechanisms of Formation . . . . .	30
2.12	Evolution in the Contact State . . . . .	32
2.13	Evolution out of the Contact State . . . . .	35
2.14	Frequency and Space Density . . . . .	39
2.15	Early-Type Contact Binaries . . . . .	40
2.16	Magnetic Activity . . . . .	40
<b>3</b>	<b>Observations and Analysis Techniques</b>	<b>43</b>
3.1	Images of Contact Binaries . . . . .	43
3.2	Photometry of Contact Binaries . . . . .	44
3.3	Spectra of Contact Binaries . . . . .	46
3.4	X-ray and Ultraviolet Data on Contact Binaries . . . . .	47
3.5	Physical Light-Curve Modeling . . . . .	48
3.6	Nomographic Light-Curve Solutions . . . . .	51
3.7	O-C Analysis . . . . .	53
3.8	Working with Survey Data . . . . .	56
<b>4</b>	<b>Motivation</b>	<b>63</b>
<b>5</b>	<b>Methods</b>	<b>66</b>
5.1	Sample Description . . . . .	66
5.2	Measuring Photospheric Temperature with SDSS . . . . .	68
5.2.1	SDSS Photometry Data Cuts . . . . .	70

5.3	Light-Curve Harmonic Fitting . . . . .	70
5.3.1	Light-Curve Harmonic Fit Filters . . . . .	71
5.4	Division of the Light-Curve . . . . .	71
5.4.1	Light-Curve Division Data Quality Cuts . . . . .	73
5.5	Regression of the Residuals . . . . .	75
5.5.1	Regression of the Residuals Data Quality Cuts . . . . .	76
5.6	Computation of a Uniformity Metric . . . . .	77
<b>6</b>	<b>Results</b>	<b>79</b>
6.1	$\dot{F}$ and Photospheric Temperature . . . . .	79
6.2	Region Disagreement and Photospheric Temperature . . . . .	80
6.3	Correlation of Changes between Light-Curve Regions . . . . .	82
6.4	Conclusions . . . . .	86
<b>7</b>	<b>Future Projects</b>	<b>87</b>
7.1	Coronal Rotation with GALEX . . . . .	87
7.2	Period Changes with Evryscope . . . . .	88
7.3	$H\alpha$ Fluxes in PTF . . . . .	88
7.4	Future Surveys . . . . .	88

# 1 Introduction

A contact binary is a system that contains two main-sequence stars (like our sun) in the closest possible proximity. These systems are shaped like peanuts, with a bridge of stellar material connecting the two components. The two components can transfer mass and energy through the bridge, allowing them to maintain their stability over billions of years. Throughout their lifetime, mass transfers from the less massive secondary component, to the more massive primary component, while energy is pumped into the secondary component from the primary. When the secondary transfers almost all of its mass to the primary, the system becomes unstable, and the two components merge, releasing a large amount of energy. The contact binary star is placed at the intersection of some of the most interesting questions in modern astronomy. In this introduction, we will see how contact binaries connect to a range of issues in modern astrophysics.

Modern observational techniques have allowed for the detection of transients (light sources that appear for a brief time and then disappear) in vast quantities. The supernova is a common example of a transient. By observing hundreds of supernovae, astronomers discovered that not all supernovae are the same - some are brighter than others, some last longer than others. Astronomers have also discovered transients that are not supernovae. In recent years, astronomers have been gaining information about transients that are much brighter than classical novae, but dimmer than supernovae. They named this class “Intermediate Luminosity Red Transients” (ILRT). Until recently, there was not a viable physical model for these transients. In late 2008, an ILRT emerged in the constellation of Scorpius. When astronomers looked in archival data - they found a contact binary in the spot where the nova was to occur. The leading theory is that the merger of the two components of a contact binary system causes these Intermediate Luminosity Red Transients.

While contact binaries systems are very different than the sun, they are important tools for testing the solar-stellar connection: the idea that the sun is similar to other stars and that we can learn about other stars by observing the sun, and vice-versa. While the sun takes almost a month to rotate, almost all contact binaries complete a full orbit in less than a day. Contact binaries have strong magnetic fields (as much as 1000 times stronger than the sun’s) because they are moving about their rotational axis much more quickly. We will see that each component of a solar type contact binary exhibits a similar structure to the sun: a radiative inner layer surrounded by a convective envelope. For this reason, contact binaries exhibit the same magnetic phenomena (such as starspots, and flares) as the sun does, except these phenomena on contact binaries are much more dramatic, owing to their stronger magnetic fields. The dramatic magnetic phenomena in contact binaries is observable from large distances. From the earth, we can monitor the magnetic activity of thousands of

contact binary stars, which can possibly teach us about our own sun. This is the subject of much of the original work in this thesis.

With the recent direct observation of gravitational waves by LIGO, there has been renewed interest in gravitational wave sources. The source of the first gravitational wave detection was two intermediate mass ( $20 - 30M_{\odot}$ ) black holes, which was an unexpected result. Astronomers were uncertain about how two intermediate mass black holes could get close enough to each other to merge. Short-lived, massive contact binary stars offer a solution to this problem. The vast majority of contact binary stars have components with similar masses to the sun. However, a few consist of two very massive O or B type stars. When a O or B type star ends its life, it undergoes a supernova explosion, resulting in a black hole. Each of the two stellar components in a O or B type contact binary is massive enough to form its own black hole at the end of its life. In this way, O and B type contact binaries provide a mechanism for producing two intermediate black holes in a close orbit.

As we will learn, contact binaries are a well-defined class with strict relationships between parameters like mass, luminosity, temperature, and orbital period. This means that by measuring a few parameters, many others can be accurately predicted. There are theoretically and empirically defined relationships between a contact binary's period, temperature, and luminosity. This means that by measuring a contact binary's orbital period (which can be done easily and precisely) astronomers can predict the contact binary's absolute luminosity (which is difficult to measure with traditional methods). For this reason, contact binaries are important *standard candles*. Contact binaries are much more common than other standard candles like Cepheid Variables, or RR Lyrae variables. They can be used to trace the structure of the Milky Way galaxy, and accurately determine distances to other galaxies, like the Andromeda galaxy.

In these ways, the contact binary stands at the intersection of time-domain, solar, gravitational wave, and stellar astronomy. Right now, the study of contact binaries also stand at another important intersection: the intersection of “old” and “new” observational techniques.

We roughly can split observational astronomy into roughly two modes: “Exploration Mode”, where we look out and see what there is to see, without a particular target in mind; and “Target Mode”, where we observe a very specific set of objects in a way tailored to learn about known phenomena.

In the 20th century, much of the science of astronomy operated in “target mode”. The science of astronomy was “data poor”. The limiting factor of discovery was observations from large telescopes of the day. If a scientist had new, proprietary data, science would come out of it. At the turn of the 21st century (enabled by advances in data storage, data processing and robotics) observational astronomical science began to shift modes.

Old telescopes were being remodeled: old gears, motors and lenses were being replaced with robotic systems, enabling their autonomous operation. New telescopes were being constructed with the express purpose of deeply surveying the sky - with minimal human interaction. No longer inhibited by human operators, telescopes could image the sky continuously - dawn to dusk. Data poured from these telescopes like water from a firehose. Since the 1990s, the new images filled massive stacks of servers: for the first time, astronomers were “data rich”.

The monstrous stream of data provided by these new systems had to be filtered. The most productive scientist was no longer the scientist with access to the best data, it became the scientist with the best techniques for filtering, stacking, folding, combining, or otherwise analyzing the data. Astronomers started shifting back to “Exploration Mode”.

Asteroids were discovered by the thousands. The rate of supernova discovery accelerated from one every few years to approximately *one every night*. The number of known eclipsing binaries ballooned from just over a thousand, to tens of thousands. The number of galaxies with known distances was increased dramatically by the Sloan Digital Sky Survey. This progress is accelerating: within the decade, at least three major sky surveys of unprecedented depth and cadence will come online.

In the 21st century, we can study thousands of contact binary systems at once, using data from all-sky surveys. This approach presents huge advantages over taking painstaking observations of single contact binary systems. Due to the sheer number of systems studied, conclusions about contact binary behavior can be supported by robust statistics. However, there are also weaknesses to this approach. Many of the techniques that have been developed for extracting physical information out of observational data do not work well with survey data, because survey data tends to be of lower quality. We are forced to develop new techniques, and ask different questions.

In §2 I provide a brief history of the discovery of the first contact binary star, and outline major leaps of understanding in the field. In §3, I discuss the types of observations that can be used to learn about contact binary systems. In §3.5, I describe some ways that astronomers use models to convert raw observational data into measurements of physical parameters. We are introduced to survey data in §3.8. In §4, §5, and §6, I present original research that I have undertaken with Dr. Tom Prince, Dr. Ashish Mahabal, Dr. Eric Bellm, and Dr. Andrew Drake at the California Institute of Technology. In §7, I provide three projects that a student can undertake right now to continue the study of contact binary stars.

In this thesis, my main objectives are to provide an introduction to the field of contact binary study, and to provide a roadmap that a future student can use to continue this work.

## 2 Theory

### 2.1 Discovery

To understand the history of the study of contact binaries, we must start at the source: the advent of a precise way of measuring the brightness of a celestial object.

In 1861, J.K.F. Zöllner, developed the first practical photometer. In Zöllner's photometer, the image of a real star as focused by a 5-inch objective lens was compared with the light of an artificial star, produced by a bunsen-like gas burner, in the same field of view (Fig. 1) [Staubermann, 2000]. The brightness of this artificial star could be adjusted by changing the relative orientation of two prisms until it matched that of the real star. By recording the relative angle of the prisms when the brightness of the artificial and real star were equal, a photometric measurement could be obtained. In the 1860s, Zöllner supplied 22 photometers to the great observatories throughout the western world. One of these photometers arrived at the Potsdam Observatory, 15 miles southwest of Berlin's city center [Krisciunas, 2001].

Karl Hermann Gustav Müller, and Paul Friedrich Ferdinand Kempf collaborated on observations for the Potsdam *Photometrische Durchmusterung des Nördlichen Himmels* (Photometric Catalogue of the Northern Heavens), one of the three great photometric catalogues of the late nineteenth century [Bolt et al., 2007]. When it was completed, it contained the brightnesses and colors of roughly 14,000 stars down to visual magnitude 7.5 - a monumental undertaking.

While Kempf and Müller were making the initial observations for Part III of their *Durchmusterung*, they discovered that two measurements of an otherwise inconspicuous star (the first made in 1899, the second made in 1901) differed by an amount that was greater than was expected. In their survey, each star that showed the potential for variability was continuously observed at a later date to verify the nature of variability.

At the Potsdam Observatory on January 14th, 1903, the sun set at 4:20pm. At 5:56pm, Kempf and Müller began constructing a complete light-curve of  $BD+56^{\circ}.1400$ , which would later be named W Ursae Majoris. They observed until 10:30pm. Follow-up observations three nights later allowed for the construction of the first light-curve of a contact binary star (Figure 2).



Figure 1: Fig. 4 from Staubermann [2000], showing a modern reproduction of a Zöllner photometer. The tube is the refractor telescope.

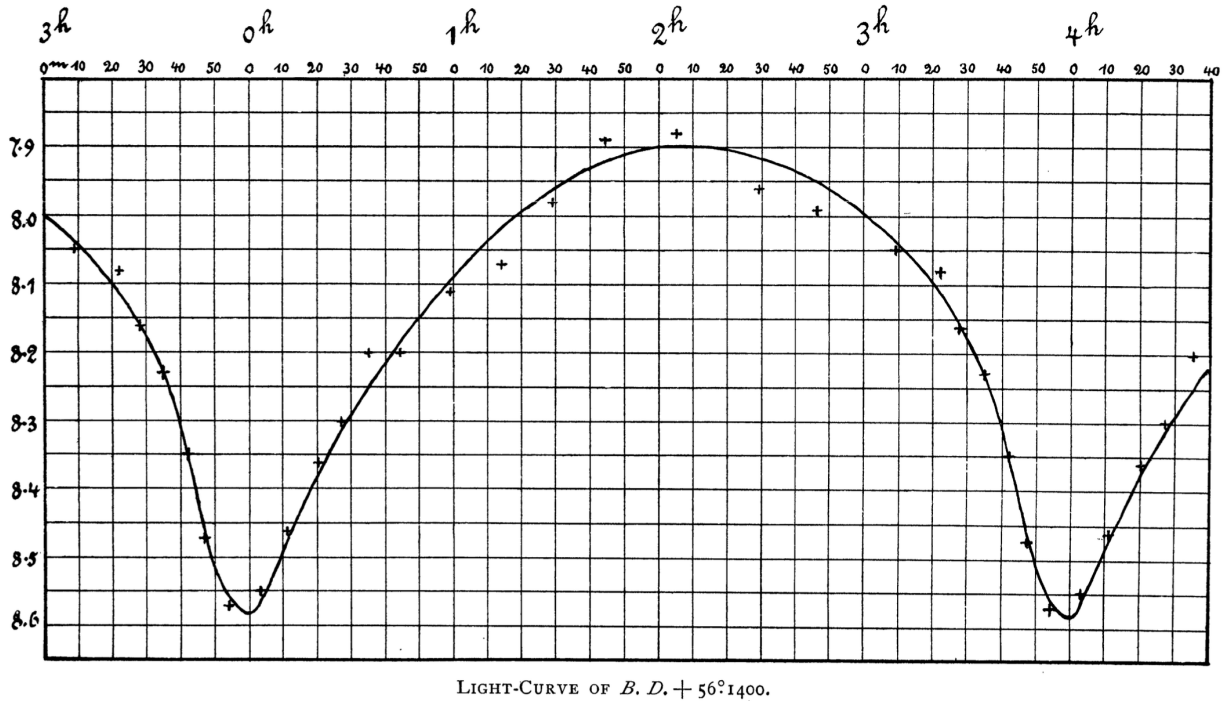


Figure 2: The first light-curve of a contact binary star. The solid curve is interpolated by eye and drawn carefully in pen. (Fig. 1 from Müller and Kempf [1903]).

The shape of the light-curve was unlike anything that Müller and Kempf had seen before, and they struggled to think of a physical system that could produce such a light-curve, rejecting many hypotheses, before speculating:

*“We may finally consider the hypothesis that the light-variation is produced by two celestial bodies almost equal in size and luminosity whose surfaces are at a slight distance from each other, and which at times almost centrally occult each other in their revolution... On this hypothesis we have only one difficulty, and the not inconsiderable one, as to whether such a system is mechanically possible and can remain stable for any length of time.”*

This passage marks the beginning of the formal study of contact binary stars. In this thesis (written 114 years after the initial discovery), we will journey to the forefront of contact binary research.

## 2.2 The Main-Sequence Star

In order to understand the internal structure of contact binaries, we must first understand the structure of their two components: main-sequence stars. The main sequence was an empirically derived group: As astronomers started recording the luminosity and color of large numbers of stars, they observed that most stars obeyed a relationship between luminosity and color. The reason for this relationship is that all of the stars within the main-sequence created energy using the same reaction. This relationship can be visualized in an *Hertzsprung-Russell Diagram* (or H-R Diagram), as in Fig. 3. Hertzsprung and Russel called the main cluster of points on this diagram the “Main Sequence”. The most familiar example of a main sequence star is our Sun. When a star is fusing hydrogen into helium at its core, we say that it is on the main sequence.

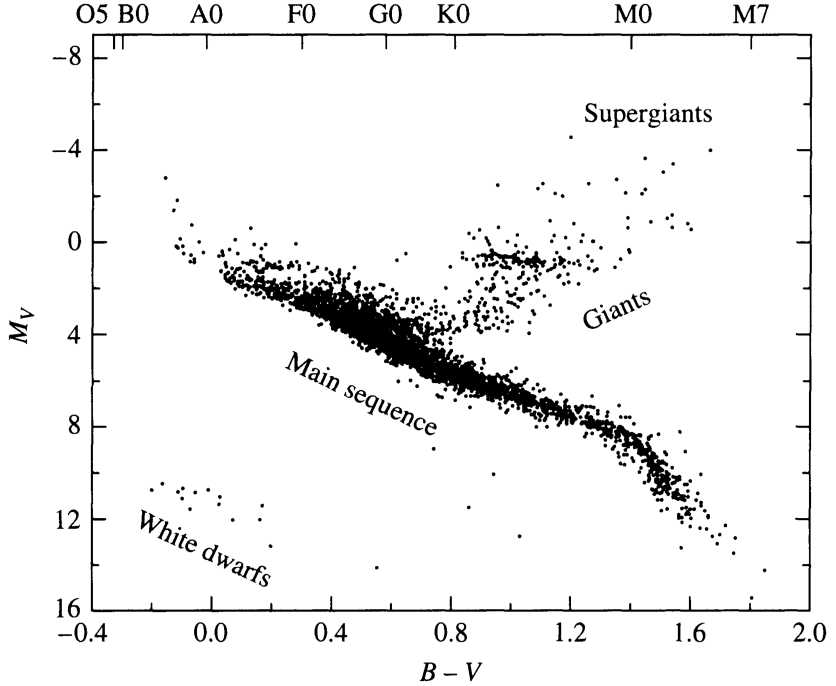


Figure 3: An observer’s Hertsprung-Russel (H-R) diagram. The data are from the Hipparcos catalog. (Fig. 8.13 from Carroll and Ostlie [2006]).

Astronomers have an excellent understanding of the properties (like mass, luminosity, or temperature) of main-sequence stars. Models of main-sequence stars that rely on basic time-independent equations of stellar structure have been successful.

The time-independent equations of stellar structure are a set of relationships between the properties of main sequence stars. They specify pressure ( $P$ ), enclosed mass ( $M_r$ ), enclosed luminosity ( $L_r$ ), and temperature ( $T$ ) as a function of radius  $r$ . You will notice that all of the following equations are actually derivatives. When we supply the appropriate boundary condition (e.g. “the temperature  $T$  at 1 solar radius is 5800K”), the equations allow for the complete solution of the profile of temperature, pressure, and mass through the star. While for our purposes it is not important to understand how to find a simultaneous solution for this example, it is instructive to see the role that various constants like the stellar opacity  $\kappa$ , density  $\rho$ , or nuclear reaction efficiency  $\epsilon$ , play in the profile of temperature, pressure, or enclosed luminosity.

$$\frac{dP}{dr} = -G \frac{M_r \rho}{r^2} \quad (2.1)$$

$$\frac{dM_r}{dr} = 4\pi r^2 \rho \quad (2.2)$$

$$\frac{dL_r}{dr} = 4\pi r^2 \rho \epsilon \quad (2.3)$$

$$\frac{dT}{dr} = -\frac{3}{4ac} \frac{\bar{\kappa} \rho}{T^3} \frac{L_r}{4\pi r^2} \quad (2.4)$$

In the preceding equations,  $c$  is the speed of light, and  $a = \frac{4\sigma}{c}$  is known as the radiation constant. Energy is generated at the core of low-mass main sequence stars via the Proton-Proton Chain, or *pp-chain*. The pp-chain has three branches, each producing helium out of Hydrogen (H), Helium (He) and Beryllium (Be). At each juncture in the chain a photon ( $\gamma$ ) is emitted, releasing energy into the inner layers of the star (Fig. 4).

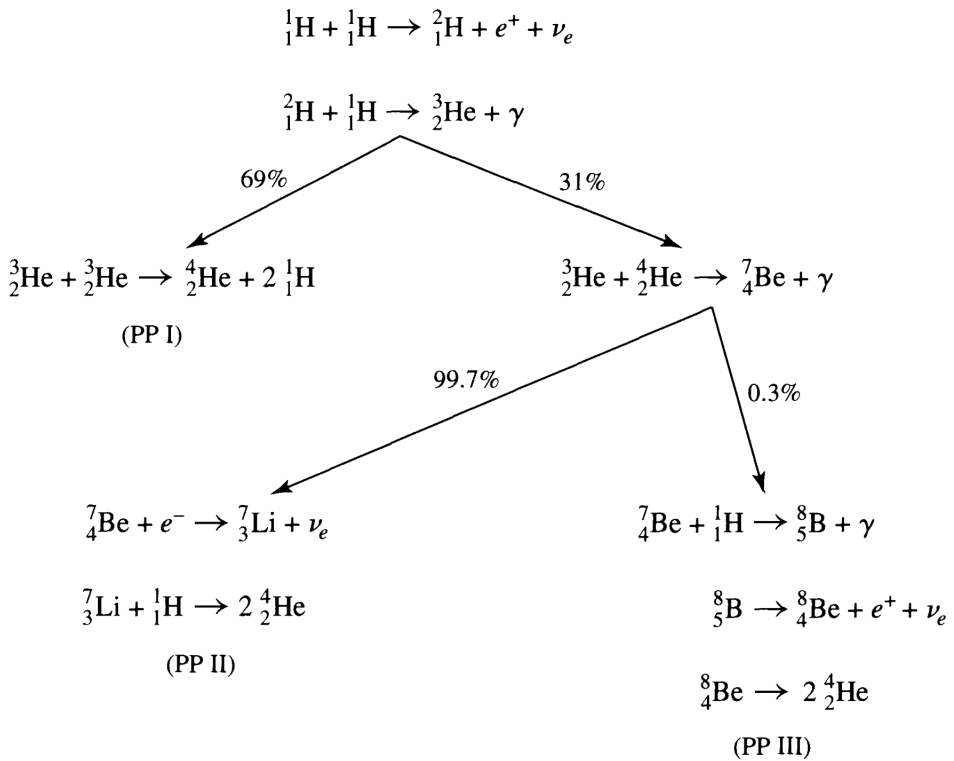


Figure 4: A diagram of pp-chain reactions. Percentages by the arrows indicate the branching ratios, revealing that the PP I and PP II chains occur much more frequently than the PP III chain. (Fig. 10.8 from Carroll and Ostlie [2006]).

At temperatures near the temperature of the solar core, the efficiency  $\epsilon$  of the pp-chain is proportional to  $T^4$ , so hotter stars can get more energy out of the pp-chain. For stars with higher core temperatures than the sun, another reaction (the CNO-cycle) becomes much more efficient than the pp-chain. Through the conversion of mass to energy via the pp-chain, low-mass main-sequence stars shine. For the rest of this thesis, we can treat the

core of the main-sequence star as a black-box that pumps energy into the outer layers of the star.

### 2.3 The Main-Sequence Homology Relations

The Main-Sequence Homology Relations (sometimes called the Main-Sequence Scaling Relations) are relationships between the Luminosity  $L$ , Mass  $M$ , Radius  $R$ , and temperature  $T$  of zero-age main-sequence (ZAMS) stars. These relationships exist because main sequence stars with the same reaction mechanism at their cores (e.g. the pp-chain) are homologous. Two stars that both produce the vast majority of their energy through the pp-chain and obey the same equations of stellar structure have homologous structures, i.e. the smaller star is just a “scaled-down” version of the larger star.

We can calculate these homology relations by using models based on the time-independent equations of stellar structure. Researchers have used models to derive the following relationships for newly-born stars with a mass of than 1.66 solar masses ( $M < 1.66M_{\odot}$ ):

$$\frac{L_{\text{ZAMS}}}{L_{\odot}} \approx 1.03 \left( \frac{M}{M_{\odot}} \right)^{3.42} \quad (2.5)$$

$$\frac{R_{\text{ZAMS}}}{R_{\odot}} \approx 0.89 \left( \frac{M}{M_{\odot}} \right)^{0.89} \quad (2.6)$$

$$\frac{T_{\text{ZAMS}}}{T_{\odot}} \approx 1.07 \left( \frac{M}{M_{\odot}} \right)^{0.41} \quad (2.7)$$

As we can see in Eqns. 2.5, 2.6, and 2.7, the more massive a star is, the hotter, larger, and more luminous it is. Of the three parameters ( $L, R, T$ ), luminosity  $L$  has the strongest dependence on mass  $M$ . The homology relationships are great for providing reasonable approximations of stellar properties. For example, if someone told you that “The mass of Tau Ceti is about  $0.78 M_{\odot}$ ”, and asked you to calculate the luminosity of Tau Ceti, you would perform the following calculation:

$$\left( \frac{M_{\text{tau ceti}}}{M_{\odot}} \right) = 0.78 \quad \left( \frac{L_{\text{tau ceti}}}{L_{\odot}} \right) = \left( \frac{M_{\text{tau ceti}}}{M_{\odot}} \right)^{3.42} = 0.78^{3.42} \approx 0.42 \quad (2.8)$$

So, we have used the main-sequence homology relations to calculate that Tau Ceti has about 42% of the the luminosity of our sun.

### 2.4 ZAMS to TAMS

The observable characteristics of main sequence stars change slightly throughout their time on the main sequence. When a protostar starts fusing hydrogen into helium, we say that it

as reached *ZAMS*, (Zero-Age Main-Sequence). When the hydrogen in the core of the main-sequence star is depleted, it must burn other elements to remain stable. When the core of the star uses the last of its hydrogen, we say that the star has reached *TAMS*, (Terminal-Age Main-Sequence).

In the context of contact binaries, it is important to discuss the changes that occur to a star as it progresses through its main-sequence life. Upon reaching ZAMS, the main-sequence star is the most compact. As it gets older, its radius and luminosity increase, and its temperature decreases. We can calculate the magnitude of these changes by using analytical fits to stellar models. The analytical fits from Demircan and Kahraman [1991] that we will use have been derived for main-sequence stars with  $M < 1.66M_{\odot}$ . The vast majority of the components of contact binaries have  $M < 1.66M_{\odot}$ , for which the following relations are valid:

$$R_{ZAMS} \approx 0.89M^{0.89} \quad R_{TAMS} \approx 2.00M^{0.75} \quad L_{ZAMS} \approx 1.03M^{3.42} \quad L_{TAMS} \approx 2.54M^{3.41} \quad (2.9)$$

Where  $M$  is the mass of the star in solar units.

$$\frac{R_{TAMS}}{R_{ZAMS}} = \frac{2.25}{M^{0.14}} \quad \frac{L_{TAMS}}{L_{ZAMS}} = \frac{2.46}{M^{0.01}} \quad (2.10)$$

By using the Stephen-Boltzmann equation for the radiation of a sphere, we can solve for the fractional temperature change  $\frac{T_{TAMS}}{T_{ZAMS}}$ :

$$L = 4\pi R^2 \sigma_b T^4 \rightarrow \frac{T_A}{T_B} = \left(\frac{L_A}{L_B}\right)^{\frac{1}{4}} \left(\frac{R_A}{R_B}\right)^{\frac{1}{2}} \quad (2.11)$$

Where  $\sigma_b$  is the Stephen-Boltzmann constant.

Using equations 2.10 and 2.11, we can compute a table comparing ZAMS stars to TAMS stars, for a variety of masses.

Table 1: Comparison of Stellar Observables from ZAMS to TAMS

Stellar Mass	$\frac{R_{TAMS}}{R_{ZAMS}}$	$\frac{L_{TAMS}}{L_{ZAMS}}$	$\frac{T_{TAMS}}{T_{ZAMS}}$
$1.5M_{\odot}$	2.10	2.45	0.86
$1.0M_{\odot}$	2.25	2.46	0.84
$0.5M_{\odot}$	2.48	2.48	0.79
$0.2M_{\odot}$	2.81	2.50	0.75

We can see that at TAMS, a low-mass main-sequence star's radius and luminosity have increased by a factor of over two, while the surface temperature drops by 14% - 25% of

the ZAMS value. As a star fuses the hydrogen in its core via the pp-chain, the resulting helium builds up at the center of the star. This causes the hydrogen burning to occur in a “shell” of increasing radius around the helium core. Consequently, as a main-sequence star progresses from ZAMS to TAMS, its radius increases slightly, and its photosphere becomes slightly cooler. Thus, the age of the two components of a contact binary affects the radius and density of the star. The changes in luminosity and radius that occur during the main sequence have strong implications for the stability of contact binary systems (§2.8).

## 2.5 Metallicity

By far, the parameter that has the largest effect on the stellar properties is the mass. However the chemical composition of a star can also influence its observables. Astronomers use a simplified system consisting of three numbers  $[X, Y, Z]$  to refer to the chemical composition of a star:

$$X = \text{Hydrogen Abundance} \quad Y = \text{Helium Abundance} \quad Z = \text{Abundance of everything else}$$

$$X + Y + Z = 1 \quad (2.12)$$

When astronomers refer to “Metallicity”, they are often referring to  $Z$ : the fraction of the mass of the star that is not hydrogen or helium. For our own sun,  $Z = 0.02$ , which is referred to as the *solar metallicity*.

Metallicity influences the observables of main-sequence stars by affecting the opacity  $\kappa$  of the stellar material (see Eqn. 2.4). In general, stars with a higher metallicity  $Z$  also have a higher opacity  $\kappa$ . The increased opacity increases the effect of radiation pressure on the outer layers of stars, causing stars with higher metallicities to also have a slightly larger radius.

## 2.6 The Roche Potential

In the equations of stellar structure, there is a hidden assumption. These time-independent equations of stellar structure assume that the stellar matter exists in the potential of a point mass:

$$\Psi_{\text{point}} = \frac{GM}{r} \quad (2.13)$$

Where  $G$  is the gravitational constant.

However, a contact binary system cannot be modeled as a point mass. A contact binary most definitely contains *two* masses, because it contains two stellar components. We

can approximate these stellar components as two point masses, separated by a distance  $a$ . Despite this necessary point-mass approximation, the Roche model can be used to calculate the structure of binary stars [Kippenhahn and Thomas, 1970]. The Roche model assumes synchronous rotation, circular orbits and two point masses. Its coordinate system is based in the rotating frame [Kopal, 1959].

Mochnacki [1984] has computed the Roche potential in Cartesian ( $x,y,z$ ) coordinates, useful for performing numerical integrations. They write:

“In Cartesian coordinates, with the origin at the center of mass of the primary, the  $x$ -axis aligned with the centers of mass, and the  $z$ -axis parallel to the rotation axis, the potential at a point  $(x,y,z)$  co-rotating with binary system is given by:

$$\Psi_{\text{roche}}(x, y, z) = -\frac{G(M_1 + M_2)}{2a} C \quad (2.14)$$

where

$$C(x, y, z) = \frac{2}{1+q} \frac{1}{(x^2 + y^2 + z^2)^{\frac{1}{2}}} + \frac{2q}{1+q} \frac{1}{1+q[(x-1)^2 + y^2 + z^2]^{\frac{1}{2}}} + (x - \frac{q}{1+q})^2 + y^2 \quad (2.15)$$

$q = \frac{m_2}{m_1}$ ,  $(x, y, z)$  are in units of  $a$ , the separation between the two point masses.”

The Roche potential has points where  $\nabla\Psi = 0$ , called Lagrange Points (see Figure 6).

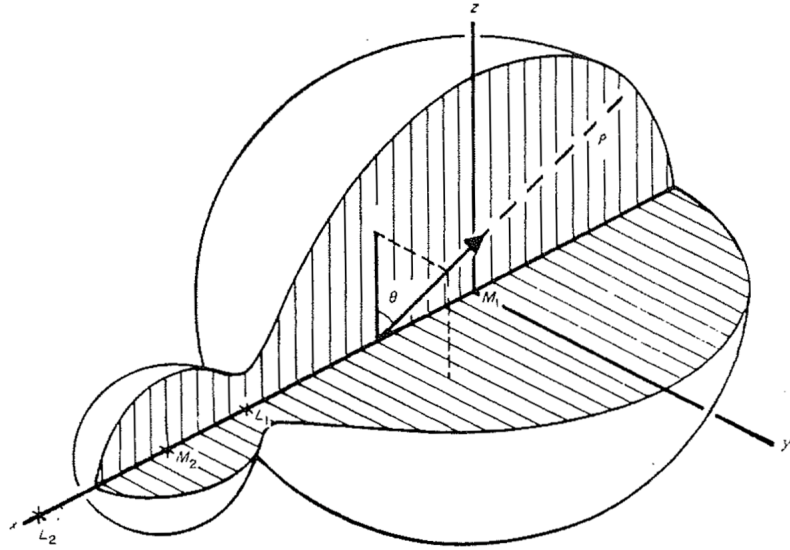


Figure 5: The coordinate system used in equations 2.14 and 2.15 to describe the potential  $\Psi$  of a contact binary system. (Fig. 1 from Mochnacki and Doughty [1972]).

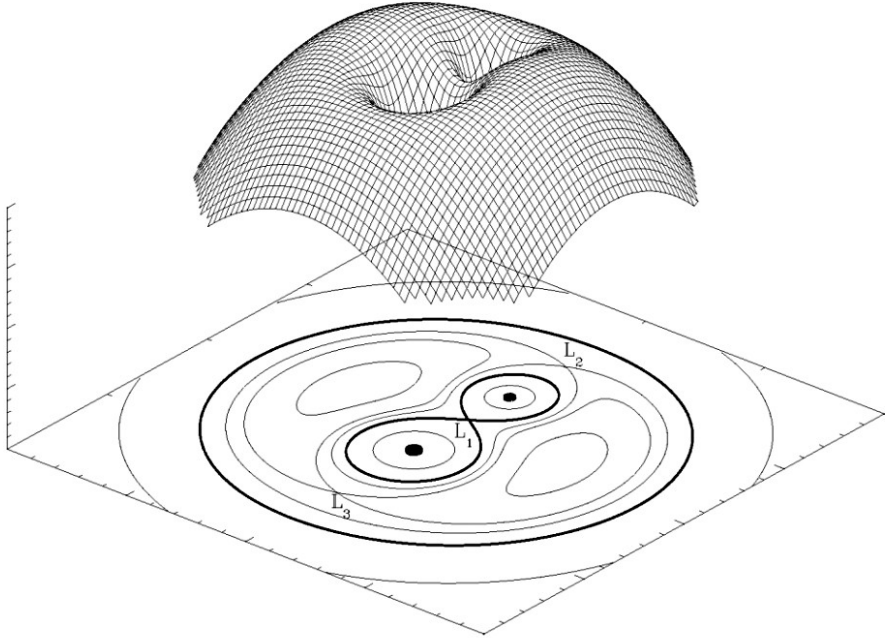


Figure 6: A composite 3D and contour plot of the Roche potential. The Roche lobe is the dark equipotential curve shaped like the  $\infty$  symbol. Three out of the five Lagrange points are labelled ( $L_1, L_2, L_3$ ) [Sluys, 2006].

Now that we understand the shape of the Roche potential, we can learn how the Roche potential is used to classify eclipsing binary stars, in a scheme primarily developed by the work of Kopal [1959].

In this scheme, eclipsing binaries are classified according to the location of the two photospheres relative to certain Roche equipotentials [p. 109, Kallrath and Milone, 2009]. An equipotential is a curve where the potential  $\Psi$  is equal to a constant value  $C$ ,  $\Psi = C$ . In Figure 7, we see three types of eclipsing binaries. In Detached systems, the photosphere of each component is well within the Roche lobe (the equipotential curve shaped like  $\infty$ ). In a Semi-detached configuration, the photosphere of one component completely fills its Roche lobe (touching the  $L_1$  point, while the photosphere of the other component remains well within its Roche lobe). In Overcontact systems, both components *overfill* the Roche lobe, and a bridge of stellar material connects the two components, covering the  $L_1$  point [Terrell, 2001].

Now we know how Detached, Semi-Detached, and Overcontact binaries are classified - but wait: Where are the *Contact Binaries*? Until now, we have presented contact binaries as “Overcontact Binaries”. But why did we have to make the name change?

Since the first half of the 20th century, most astronomers believe that the term “contact” (an abbreviation of Kopal’s “overcontact”) means that the photospheres of the two

components are touching physically. This is incorrect, according to the original classification scheme of Kopal [1959]. He intended contact to mean that the photospheres of the stars were in contact with their Roche Lobes. Though the term “contact” binary is technically incorrect, it is the most common usage in the literature, and is now the accepted name for these kinds of stars. For an excellent review of this naming issue, see Wilson [2001] .

The Roche lobe, (as we have been calling it) is also referred to as the *Inner Jacobi Equipotential*. There also exists an *Outer Jacobi Equipotential*. In Figure 7, the Outer Jacobi Equipotential is the outer-most curve that is drawn. It passes through the  $L_2$  point. The Inner Jacobi Equipotential is the curve that we have been referring to as the “Roche Lobe”. It is the curve shaped like the  $\infty$  symbol.

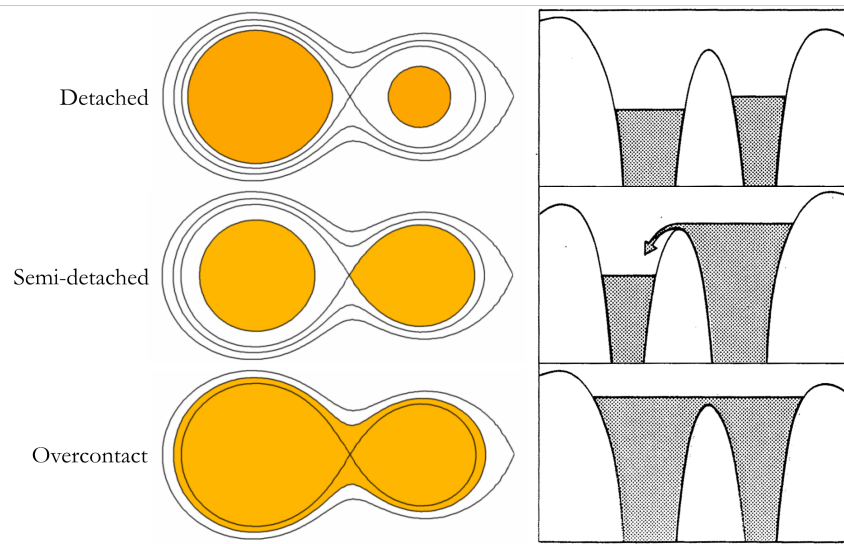


Figure 7: Types of eclipsing binary systems based on Roche geometry. In the bottom panel, (labelled “overcontact”), the photosphere of the star (shaded in orange), lies between the inner and outer Jacobi equipotentials. (Figs. 2, 3, and 4 from Terrell [2001], and Figure 1.4 from Pringle and Wade [1985]).

## 2.7 The Geometrical Elements of Contact Binary Systems

In the previous section, we have learned how to differentiate contact binary systems from the other types of eclipsing binary stars. In this section, we will learn how to describe specific contact binaries in terms of their geometrical elements. When we refer to the geometry of the contact binary system, we are really referring to the geometry of its photosphere. The vast majority of what we know of contact binary systems comes from their visible light-curves, which is why there is the convention of treating the photosphere as the “boundary” of the system. Astronomers have developed a set of geometrical elements that can describe the location of the photosphere with respect to the inner and outer Jacobi equipotentials.

The first geometrical element of note is the mass ratio  $q = \frac{m_2}{m_1}$  of the contact binary. The mass ratio is an important geometrical element in that it influences the shape of the Roche potential. We can see the effect of the mass-ratio term in equation 2.15. The Roche potential for a system with a mass ratio of unity (one) is perfectly symmetrical about the  $L_1$  point. The Roche potential for a system with a mass ratio that is far from unity is not symmetrical about the  $L_1$  point: the more massive component has an inner Jacobi equipotential that encloses more area.

The second geometrical element is the Roche lobe fill-out factor  $f$  (also called the degree of contact). This is the element that is used to describe the location of the photosphere with respect to the Inner and Outer Jacobi equipotentials.

The fill-out factor has a variety of definitions, but the most common is:

$$f = \frac{C_1 - C}{(C_1 - C_2) + 1} \quad (2.16)$$

Here  $C_1$  is the location of the inner Jacobi equipotential, and  $C_2$  is the location of the outer Jacobi equipotential.

When the photosphere of a contact binary is exactly filling the inner Jacobi equipotential, Eqn. 2.16 gives  $f = 0$ . When the photosphere of a contact binary fills the outer Jacobi equipotential, Eqn. 2.16 yields  $f = 1$ . In Fig. 8, we see the diameter  $d$  of the “neck” region (containing the  $L_1$  point), is a sizable fraction (0.1 to 0.3) of the separation of the centers of mass of the star ( $a$ ) for  $f > 0.2$ .

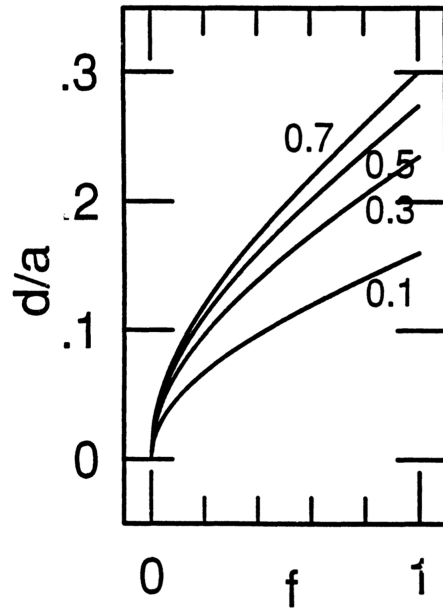


Figure 8: The widths  $d$  of the “neck” between stars, as a function of the degree of contact  $f$ , for a few values of the mass-ratio,  $q = 0.1, 0.3, 0.5, 0.7$ . The width of the neck is expressed in units of the separation between components,  $a$ . (Fig. 5 from Rucinski [1993a]).

The final element in the system is  $i$ , the inclination of the contact binary’s orbit with respect to the line of sight of the observer. This element is not intrinsic to the contact binary system, so it actually does not provide any information about the physics of the contact binary system. This element is reported because together with  $f$  and  $q$ , they completely defines the shape of contact binary light-curve as calculated using a Roche model. The light-curve of a contact binary with given values of  $f$  and  $q$  will exhibit the largest amplitude when the inclination  $i = 90^\circ$ , corresponding to a complete eclipse (see Fig. 9). When  $i = 0$ , the two components do not eclipse at all and the light-curve has amplitude 0. Inclinations between 0 and 90 correspond to partial eclipses, and the amplitude of the resulting light-curves increases monotonically with inclination (see Fig. 10).

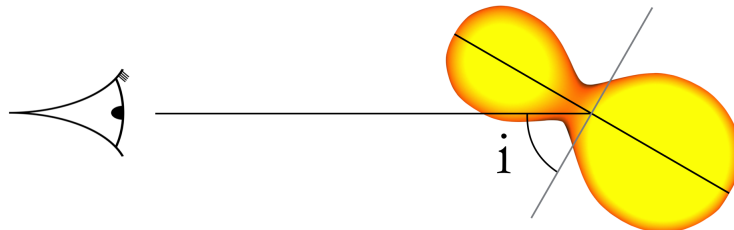


Figure 9: A diagram showing the inclination angle ( $i$ ) with respect to the observer.

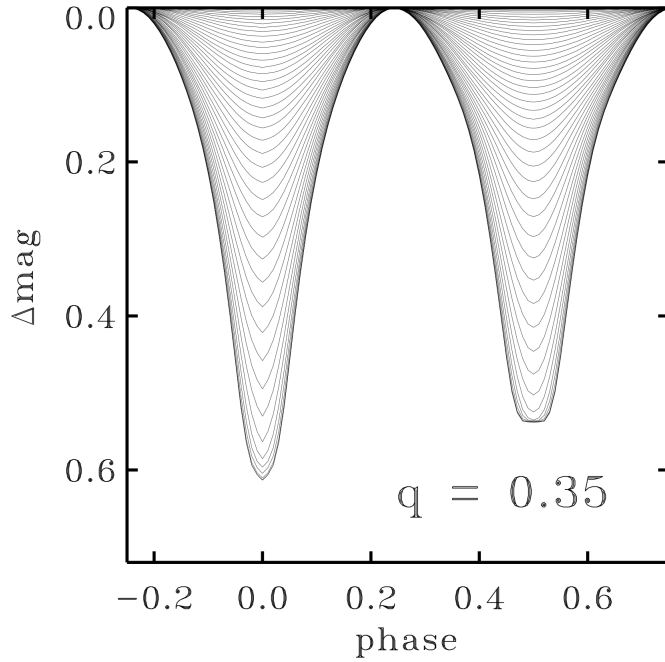


Figure 10: The calculated light-curve of a contact binary star with  $q = 0.35$ ,  $f = 0.25$ . This diagram shows how the flux received from the contact binary varies as a function of orbital phase. As the two components eclipse each other, the flux ( $\Delta\text{mag}$ ) varies. Orbital inclination  $i$  is varied in  $2^\circ$  steps. (Fig 1. from Rucinski [2001]).

In §3.5 and §3.6, we will see how the shape of the contact binary light-curve can be used to estimate the system geometry as described by  $[f, q, i]$ .

## 2.8 Thermal Equilibrium Models

The first thermal-equilibrium model of a contact binary star was developed in the late 1960's [Lucy, 1968a,b]. The great triumph of the thermal-equilibrium model is that it adequately explained the observed shape of the contact binary light-curve. Thermal equilibrium models assume that the two components of a contact binary are in *hydrostatic equilibrium*. Under the condition of hydrostatic equilibrium, the gradient in the pressure  $P$  is equal to the negative of the density  $-\rho$  times the gradient in the potential  $\nabla\Psi$ .

$$\nabla P = -\rho \nabla \Psi \quad (2.17)$$

$$\nabla \rho = \frac{dP(\Psi)}{d\Psi} = \rho(\Psi) \quad (2.18)$$

If we assume a homogenous composition on equipotential surfaces, then all state variables (pressure, density, temperature, surface gravity) are functions of  $\Psi$  alone [Webbink, 2003].

Because the photosphere of a contact binary is an equipotential surface, the temperature  $T$  should be constant across the photosphere. According to observations of contact binaries, this is true: the temperature of the shared photosphere does not vary by much across its surface.

Remember that both components of the contact binary are main-sequence stars, and so should follow the main-sequence homology relation for temperature:

$$\frac{T_{ZAMS}}{T_\odot} \approx 1.07 \left( \frac{M}{M_\odot} \right)^{0.41} \Rightarrow \quad \frac{T_1}{T_2} = \left( \frac{M_1}{M_2} \right)^{0.41} \quad (2.19)$$

If we set  $T_1 = T_2$  in Eqn. 2.19, we can see that for thermal equilibrium, it is necessary that  $M_1 = M_2$ . However, spectroscopic measurements indicate that the two components of a contact binary system almost always do *not* have equal mass:  $M_1 \neq M_2$  (see Fig. 11). In systems with  $M_1 \neq M_2$ , the secondary (the less massive component) should have a lower temperature than the primary, if both components are to follow the main sequence homology relations.

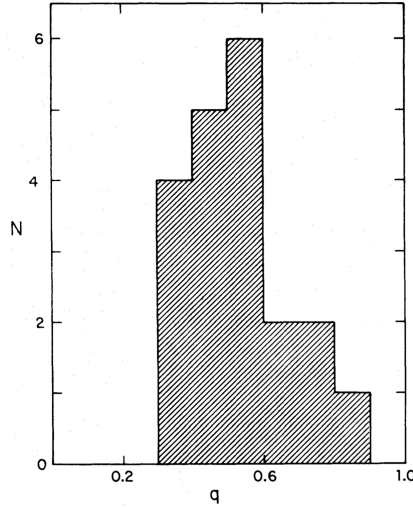


Figure 11: An early histogram of the mass-ratio  $q$  distribution of contact binary stars. Even in this crude early data, it is shown that contact binaries exhibit unequal component masses. This is different than the distribution of detached binaries, which has substantial weight at  $q = 1$ . (Fig. 3 of Lucy and Wilson [1979]).

This discrepancy means that energy must be exchanged between the two components of the contact binary in order to achieve hydrostatic equilibrium. This result is supported by observations: In Fig. 12, we see the secondaries of contact binaries and detached binaries plotted in the mass-luminosity plane. The secondaries of contact binaries are significantly *over-luminous* for their mass. In fact, Mochnacki [1981] has calculated that up to a third of the energy generated by the primary is transferred to the secondary. The energy generated

in the secondary is minuscule compared to the energy generated in the primary (< 10%), and thus the temperature of a contact binary star corresponds to the amount of energy coming from the primary, redistributed over the entire system [Rucinski, 1993a].

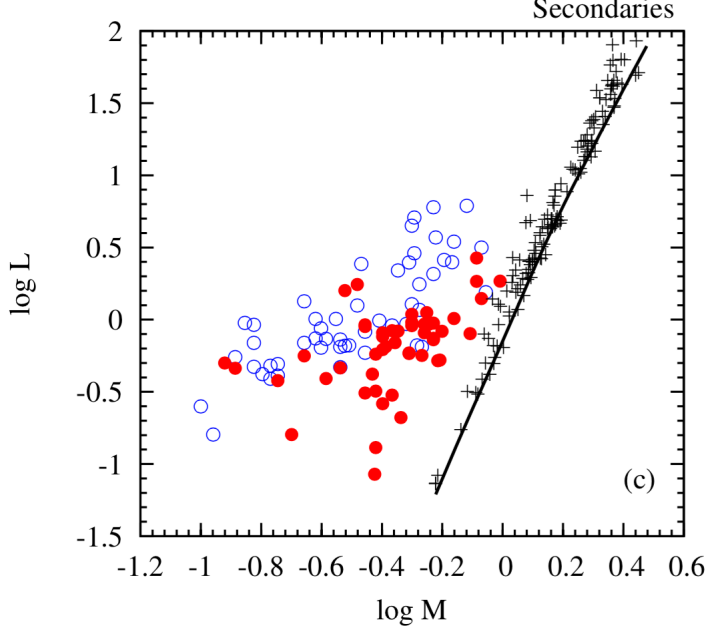


Figure 12: The mass  $M$  and luminosity  $L$  of secondaries of contact binaries ( $\circ$ ) and secondaries of detached eclipsing binaries ( $+$ ). The mass is determined via spectroscopic measurements of the radial velocity of the systems. The solid line indicates the ZAMS parameters. Notice how the secondaries of detached eclipsing binaries ( $+$ ) fit the ZAMS line well, while the contact binaries ( $\circ$ ) are *overluminous* for their mass. (Panel (c) of Fig. 1 of Yıldız and Doğan [2013]).

In comparison, the primary components of contact binaries have luminosities typical of main-sequence stars (Fig. 13). The temperature of the primary is slightly lower than a non-contact star of the same evolutionary state would have without the secondary attached to it [Rucinski, 1993a].

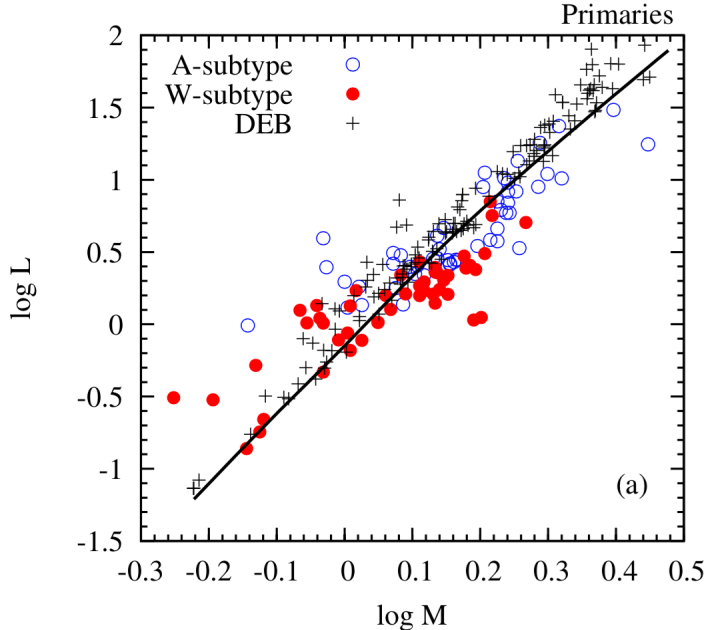


Figure 13: The mass  $M$  and luminosity  $L$  of primaries of contact binaries ( $\circ$ ) and primaries of detached eclipsing binaries ( $+$ ). The mass is determined via spectroscopic measurements of the radial velocity of the systems. The solid line indicates the ZAMS parameters, which are in rough agreement with the observed properties of the primaries. (Panel (a) of Fig. 1 of Yıldız and Doğan [2013]).

Energy is transferred through the neck of the contact binary. Kähler [2004] describes this energy transport by choosing a set of circulation functions  $[c_1, c_2]$  that describe the transfer of energy through the neck of the system. In the model of Kähler [2002], the interaction of the two components only occur in the outer layers of the secondary and primary.

In contact binary systems observed in the field, the two components are very dissimilar. Lucy [1968b] assumed that both components started out at ZAMS, however his model had trouble producing components that had different luminosities. By assuming that the two components have different evolutionary states (i.e. one component closer to ZAMS, the other component closer to TAMS), we can produce models with components as dissimilar as binaries observed in the field. The fact that we do not see any contact binaries with mass-ratios of  $q = 1$  must be due to an instability around  $q = 1$  [Rucinski, 1993a].

If the energy transfer between the components is efficient enough, the stars can maintain contact throughout their life times. However, if the energy transfer between the components is not efficient enough, the system is theorized to cycle through phases of contact and detached phases. This model for contact stability is called Thermal Relaxation Oscillation, or TRO. In the TRO model, contact binaries oscillate in and out of contact, maintaining thermal equilibrium in the contact state [Lucy and Wilson, 1979]. These oscillations of  $a$

along the semi-major axis cause the contact binary to change its period  $P$  (see Fig. 14) [Qian, 2001]. However, the observed orbital period-distribution (and low abundance of semi-detached systems) does not support TRO theory. Furthermore the loss of angular momentum (see §2.12) should cause the oscillations to die out. As of now it is unclear if the contact state is one stage in an oscillatory solution, or a stable configuration.

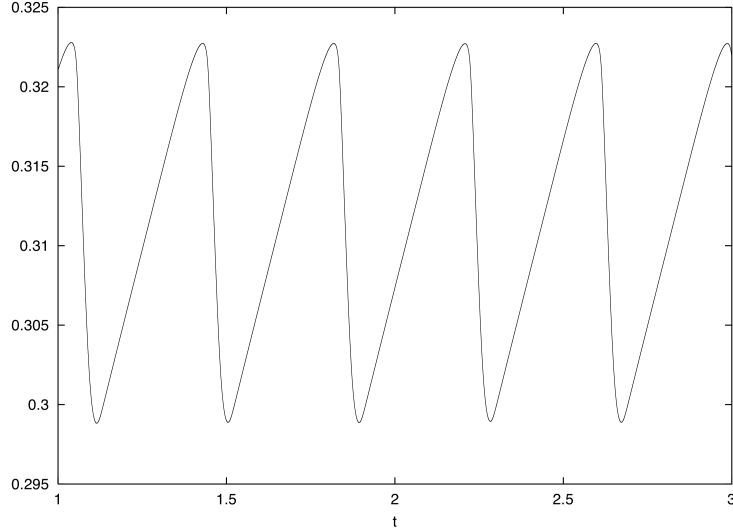


Figure 14: Plot of orbital period  $P_{\text{orb}}$  in days (on the y-axis), in comparison to thermal time  $t$  (on the x-axis). This shows the possible oscillatory nature of the contact stage. (Fig. 4 of Kähler [2002]).

## 2.9 Interior Structure

In stars, there are two primary mechanisms of energy transport: (1) In radiative transport, energy is able to leave the star through the dispersion of photons (electromagnetic energy) through the stellar medium (which is mostly hydrogen gas) and (2) in convective transport, energy is transferred through the physical motion of the stellar medium. Convective transport occurs when radiative transport is not efficient enough to transport the energy out of the star. When radiative transport dominates, the stellar material is in hydrostatic equilibrium, and energy is transported through it via electromagnetic waves. If conditions are such that radiation cannot transport energy away from the core efficiently enough, the stellar material itself will have to move to transport this energy, disrupting hydrostatic equilibrium.

Convection occurs in the stellar medium when the condition

$$\frac{d \ln P}{d \ln T} < \frac{\gamma}{\gamma - 1} \quad (2.20)$$

is satisfied [p. 325, Carroll and Ostlie, 2006]. In Eqn. 2.20,  $P$  denotes the pressure,  $T$

denotes the temperature.  $\gamma$  is the ratio of constant pressure to constant volume specific heats, which equals  $5/3$  for a monatomic gas. This equation states that when the pressure gradient is smaller than the temperature gradient, convection is more likely to occur. Convection also is more likely to occur when the stellar opacity  $\kappa$  is large.

In a main-sequence star, the primary determinant of the temperature and pressure gradients are the mass of the star  $M$ , and the radial coordinate  $r$  of the stellar medium in question. In some main-sequence stars, the criterion for convection is not satisfied at any point in the interior. We call these stars “completely radiative”. In some main-sequence stars the criterion for convection is satisfied at every point in the interior. We call these stars “completely convective”. For a star like our sun however, the criterion for convection is satisfied in some parts of the interior and is not satisfied in other parts. Main-sequence stars with a solar temperature have radiative interiors, and a thin convective envelope on the exterior. Figure 15 shows the extent of convective and radiative regions in main-sequence stars of a variety of masses. We can see that stars of solar mass  $\log(\frac{M}{M_\odot}) = 0$  or less have a convective envelope at the exterior, and that stars of greater than solar mass have radiative exteriors and convective cores.

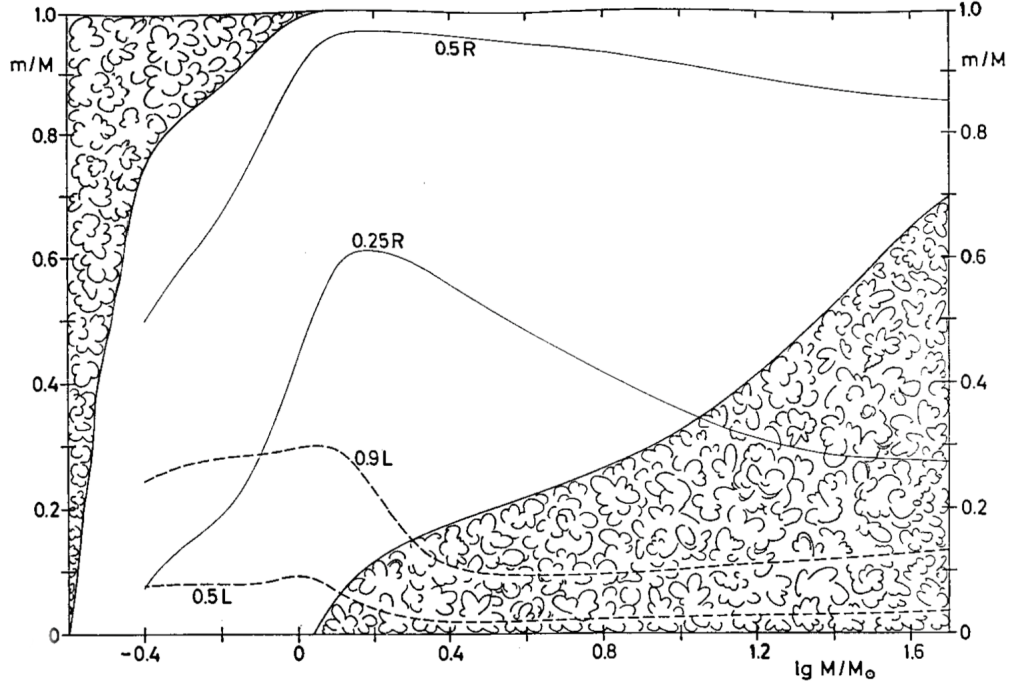


Figure 15: The mass values  $m$  from center to surface are plotted against the stellar mass  $M$  for zero-age main-sequence models. “Cloudy” areas indicate the extent of the convective zones inside the models. Two solid lines give the  $m$  values at which  $r$  is  $1/4$  and  $1/2$  of the total radius  $R$ . The dashed lines show the mass elements inside which  $50\%$  and  $90\%$  of the total luminosity  $L$  are produced. (Fig. 22.7 from page 212 of Kippenhahn et al. [1990]).

If a main-sequence star of solar composition has a photospheric temperature of less than 6200K, it will exhibit a convective envelope. The sun has a temperature of 5800K and has a thin convective envelope. If a star has a photospheric temperature of greater than 6200K, radiative energy transport is the dominant mode at the surface. Astronomers sometimes call contact binary with convective envelopes “Late-type”, and stars with radiative envelopes “Early-type”.

In Fig. 16, we see the interior structure of a typical *late-type* contact binary system. Each component has a radiative interior, and both components have a large convective envelope.

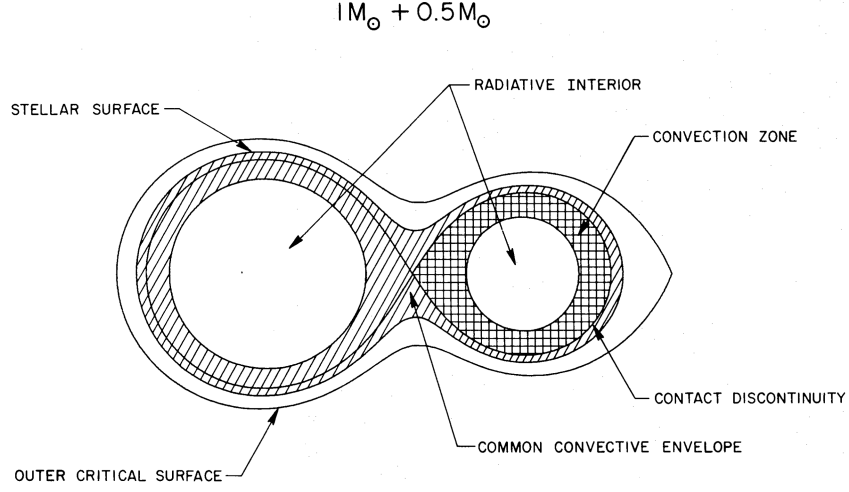


Figure 16: An equatorial cross-section of a  $1 M_{\odot} + 0.5 M_{\odot}$  (late type) zero-age contact binary of solar composition. The resulting filling factor of this model is  $f = 0.41$ , and the binary period is  $P_d = 0.228$  days. (Fig. 2 from Lubow and Shu [1977]).

In Fig. 17, we see the interior structure of a typical *early-type* contact binary system. The primary has a small convective core, and a large radiative envelope, while the secondary has a radiative core and a convective outer envelope.

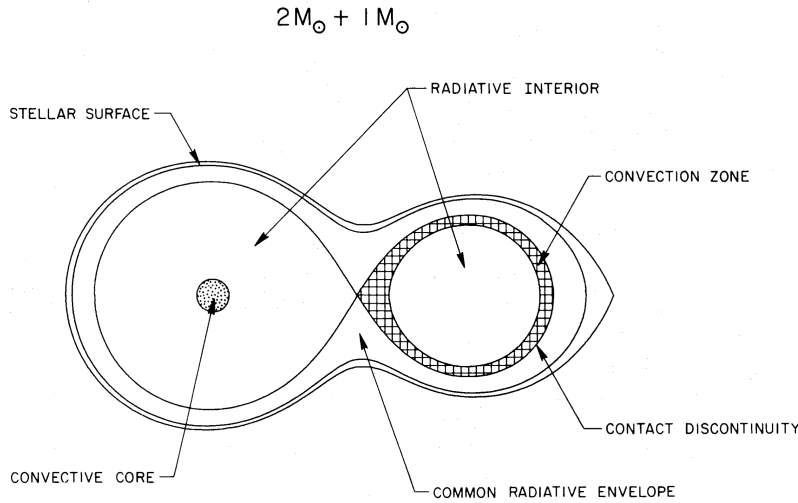


Figure 17: An equatorial cross-section of a  $2 M_{\odot} + 1 M_{\odot}$  (early type) zero-age contact binary of solar composition. The resulting filling factor of this model is  $f = 0.84$ , and the binary period is  $P_d = 0.314$  days. (Fig. 3 from Lubow and Shu [1977]).

Understanding the interior structure of the contact binary star is important because of the effects of convection. Convection causes the *radial mixing* of elements in the stellar interior. The motion generated by convection can cause strong magnetic fields, which (as we will see in §2.16) can cause starspots, flares, and changes in the mass distribution of the system (Fig. 18). There is also evidence that contact binaries with convective envelopes have smaller mass-ratios  $q$  than contact binaries with radiative envelopes.

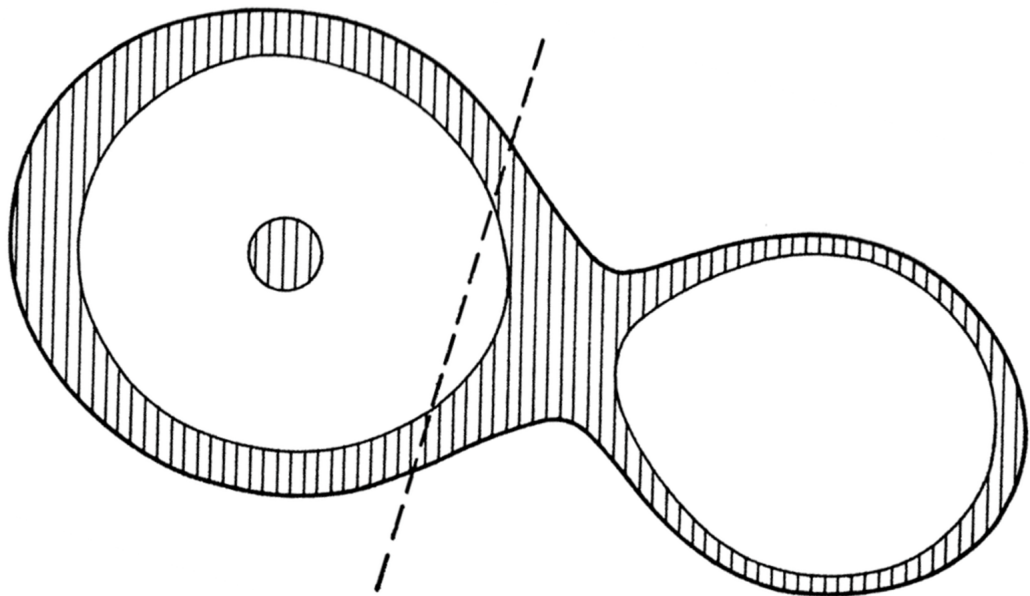
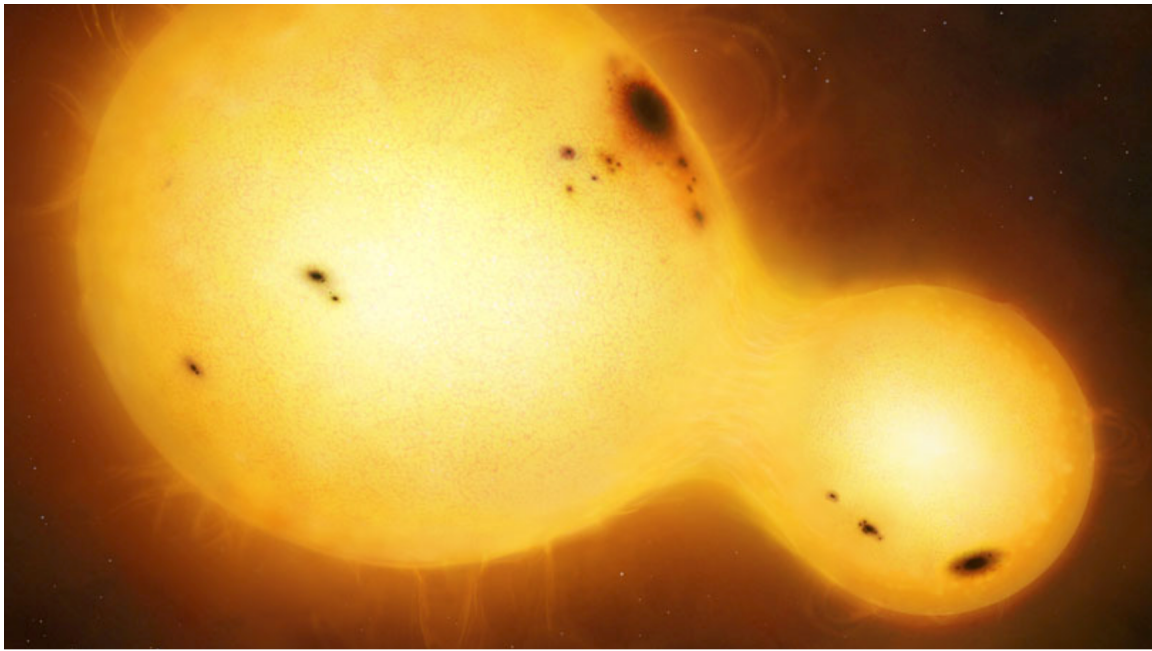


Figure 18: Model for a contact binary system. The hatched areas denote convection zones, and the vertical dashed line is the axis of rotation. (An illustration by Mark Garlick, and Fig. 1 from Lucy [1968a]).

## 2.10 The Period-Color Relation

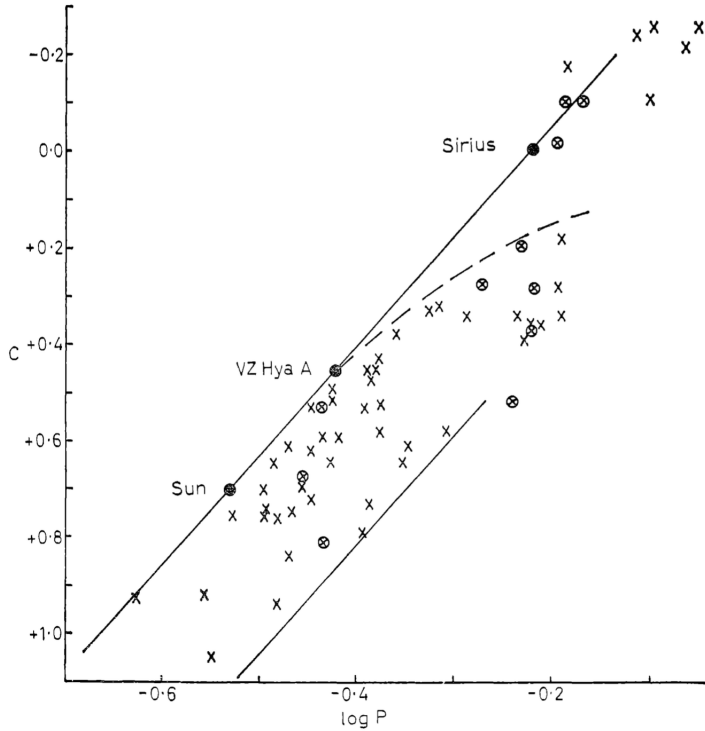


Figure 19: The color (y-axis) and period (x-axis) of the contact binary systems known in the 1960's. Bluer color (hotter) corresponds to a negative color index  $C$ . Notice the positive correlation denoted by the two solid lines. (Fig. 6 from Eggen [1967]).

Two parameters that are the easiest to observe for contact binaries are the orbital period ( $P$ ) and effective temperature ( $T$ ). In the 1960's, a correlation between these two physical parameters was discovered [Eggen, 1967]. Because the color of a star is indicative of its temperature, this relationship is most commonly called the period-color relation.

In this section, we will perform a derivation of this relation to understand why there is a relation between the orbital period ( $P$ ) and the effective temperature ( $T$ ) of a contact binary system. We start with the fact that contact binaries are composed of two main-sequence stars. Remember that main-sequence stars have well defined relationships between mass and radius:

$$\frac{R_{ZAMS}}{R_\odot} \approx 0.89 \left( \frac{M}{M_\odot} \right)^{0.89} \quad \text{for } M < 1.66M_\odot \quad (2.6)$$

We can relate the combined masses of the two stars to their periods by using the generalized form of Kepler's Third Law. We will assume that the two components of our contact binary have equal mass.

$$P^2 = \frac{4\pi^2}{G(M_1 + M_2)} a^3 \Rightarrow P^2 = \frac{4\pi^2}{G(2M)} a^3 \quad (2.21)$$

In order for the two components to be in contact, their photospheres must touch physically. This allows us to introduce the contact criterion, in which the separation between the centers of the components are equal to the sum of the two radii. We will assume that two components of our contact binary have equal radius:

$$a = R_1 + R_2 = 2R \quad (2.22)$$

We can then substitute Eqn. 2.22 into Eqn. 2.21

$$P^2 = \frac{4\pi^2}{G(2M)} (2R)^3 \quad (2.23)$$

Because we know that both of the components of the contact binary are on the main-sequence, we express the radius of the star at ZAMS in terms of its mass using Eqn. 2.6. When we substitute Eqn. 2.6 into Eqn. 2.23 (converting Eqn. 2.6 into SI units), we can express the orbital period  $P$  as a function of  $\frac{M}{M_\odot}$ .

$$P^2 = \frac{4\pi^2}{2G(\frac{M}{M_\odot})M_\odot} 8 \left( \frac{R}{R_\odot} \right)^3 R_\odot^3 \Rightarrow P^2 = \frac{16\pi^2}{G(\frac{M}{M_\odot})M_\odot} \left( 0.89 \left( \frac{M}{M_\odot} \right)^{0.89} \right)^3 R_\odot^3 \quad (2.24)$$

We can simplify Eqn. 2.24 to be prepared for the next step.

$$P^2 = \frac{(11.2)\pi^2 R_\odot^3}{GM_\odot} \left( \frac{M}{M_\odot} \right)^{1.67} \quad (2.25)$$

Now that we have the period described strictly in terms of stellar-mass, we can use the mass-temperature homology relation to express the period strictly in terms of temperature. Starting from Eqn. 2.7:

$$\frac{T_{ZAMS}}{T_\odot} \approx 1.07 \left( \frac{M}{M_\odot} \right)^{0.41} \Rightarrow \left( \frac{M}{M_\odot} \right) = 0.84 \left( \frac{T}{T_\odot} \right)^{2.44} \quad (2.26)$$

We can substitute Eqn. 2.26 into Eqn. 2.25 and simplify to find the period-temperature relationship:

$$P^2 = \frac{(11.2)\pi^2 R_\odot^3}{GM_\odot} \left[ 0.84 \left( \frac{T}{T_\odot} \right)^{2.44} \right]^{1.67} \Rightarrow \quad (2.27)$$

$$P = \left( \frac{8.4\pi^2}{G} \frac{R_\odot^3}{M_\odot} \left( \frac{T}{T_\odot} \right)^{4.07} \right)^{\frac{1}{2}} \quad P \propto \left( \frac{T}{T_\odot} \right)^{2.03} \quad (2.28)$$

Table 2: ZAMS Period-Temperature Relation

<b>Stellar Classification</b>	Stellar Temperature (K)	Orbital Period (days)
F	6500K	0.2138
G	5800K	0.1695
K	5000K	0.1253
M	3700K	0.0691

In Table 2, we plug in a few typical values for stellar temperature into Eqn. 2.28 and see what happens to the period of the contact binary.

As we can see, as the temperature of a contact binary increases, so does the period, which matches what we observe in Fig. 19. The values for the periods presented in Table 2 are actually shorter than typically observed values by a factor of 2-3. This is because we used the ZAMS homology relations in the derivation. Contact binaries do not form at ZAMS, and as we learned in §2.4 ZAMS stars have a much smaller radius than TAMS stars.

There is considerable scatter in the observed period-temperature diagram (see Fig. 19) because a contact binary's position in period-temperature space is affected by the mass of each component ( $M_1, M_2$ ), the metallicity of each component ( $Z_1, Z_2$ ), the age of each component ( $A_1, A_2$ ), the degree of contact ( $f$ ), and other factors. All of these characteristics vary considerably from binary to binary, resulting in considerable spread in the period-temperature diagram. Fortunately, researchers have made use of age-dependent and metallicity-dependent models to produce a variety of period-color relationships for stars of various ages and metallicities (Fig. 20).

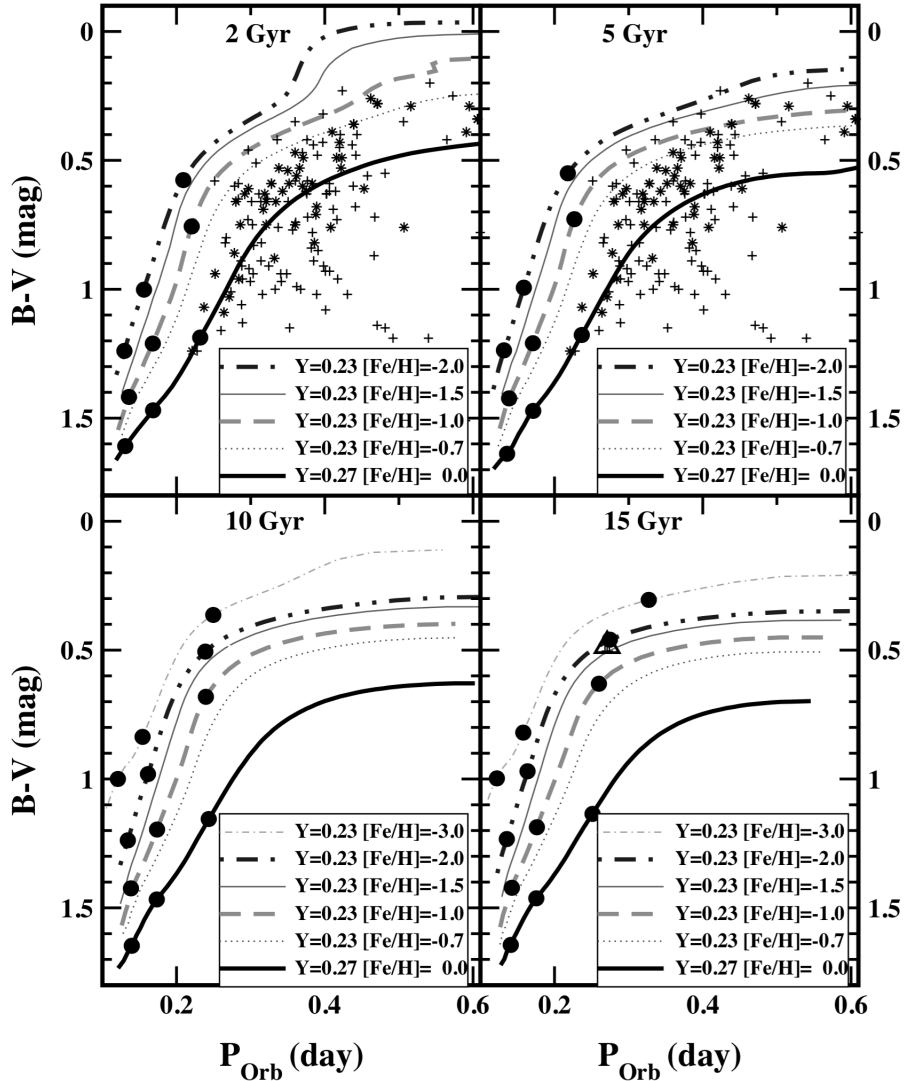


Figure 20: Metallicity and Age-Dependent Period-Color relations for contact binary stars. A smaller value of  $B - V$  magnitude corresponds to a higher temperature. Period-color relationships for individual models are plotted as lines, while observed systems are plotted as points. (Fig. 1 from Rubenstein [2001]).

Any successful model of contact binary systems should be able to reproduce the period-color relationship as defined by observed systems. Recent models that include mass circulation between the two components (e.g. Kähler [2004]) have been successful at reproducing this relationship (see Fig. 21).

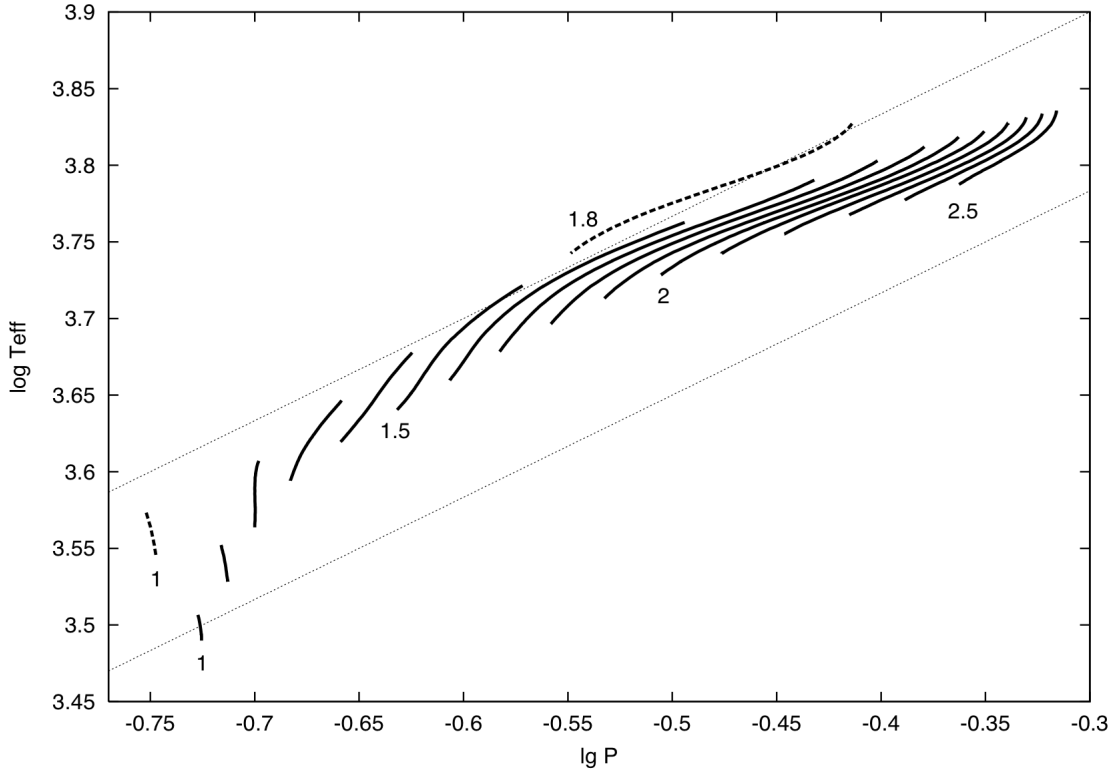


Figure 21: A series of contact binary models generated by Kähler [2004]. The set of models well reproduces the period-color relationship (as indicated by the two parallel lines). (Fig. 23 from Kähler [2004]).

## 2.11 Mechanisms of Formation

As with any object made up of stars, the starting point in the life of contact binaries is a cold cloud of interstellar gas which is mostly hydrogen. The gas cloud seeks to contract upon itself because of its own gravity, but cannot, because it is supported by its own gas pressure. As the cloud cools by radiating its energy into the surrounding space, its internal gas pressure decreases and the cloud contracts. Eventually, the cloud collapses into a small enough space that the temperature and pressure start to increase at the cloud's center. When temperatures get high enough for nuclear fusion to occur, the protostar can support itself against further collapse. At the onset of nuclear fusion, we say that the protostar has become a star, at Zero Age Main Sequence.

Early theories of contact binary formation posited that contact systems could be formed in contact, directly out of the proto-stellar material [Lucy, 1968b]. However, the symmetry and precise amount of required angular momentum render this formation path unlikely: unless exceptional orbital angular momentum loss takes place, the shortest period zero-age

binaries with solar type components should have orbital periods of 2 days or more [Stepien, 2006a]. It is likely that contact binaries start as two separate main-sequence stars which gradually fall into a contact configuration.

Indeed, binary stars are abundant in our galaxy, with over half of all stars being part of a binary or multiple system [Carroll and Ostlie, 2006]. What causes a binary star to become a contact binary? The answer is always angular momentum loss, or AML. The system of two stars in orbit loses angular momentum, resulting in an orbit with a decreasing semi-major axis. When the orbit of the binary gets small enough, mass transfer between the two components will force them into a contact configuration.

All stars slowly lose mass by shedding charged particles in a *solar wind*. For example, the mass loss rate for the sun is  $\dot{M}_\odot \approx 3 \times 10^{-14} M_\odot \text{yr}^{-1}$  [p.374: Carroll and Ostlie, 2006], which is very small compared to the sun's mass. The most active single stars lose approximately  $10^{-11} M_\odot \text{yr}^{-1}$  [Stepien, 2006a]. However, significant amounts of angular momentum can be lost to this wind. As a star rotates, its magnetic field rotates along with it. This rotating magnetic fields accelerates the charged solar wind particles that are moving away from the sun, thereby transferring angular momentum from the sun to the magnetized solar wind. In this way, the rotation of the sun slows, and it loses angular momentum. An interaction between rotating stars and stellar wind occurs in binary systems, causing them to lose angular momentum. This interaction between a rotating star and a magnetized solar wind creates a pattern in the stellar magnetic field called a Parker spiral [p.380: Carroll and Ostlie, 2006]. This loss of angular momentum decreases the separation between the components  $a$ , and orbital period  $P$  of the binary. In Eqn. 2.29, we present a semi-empirical formula for the orbital period decrease of a close, cool binary, based on the rotation evolution of solar type stars, derived by Stepień [2006a].  $P_{\text{orb}}$  is in days, and  $t$  is  $\frac{dP_{\text{orb}}}{dt}$  increases as the period decreases.

$$\frac{dP_{\text{orb}}}{dt} = (-2.6 \pm 1.3) \times 10^{-10} P_{\text{orb}}^{-\frac{1}{3}} e^{-0.2P_{\text{orb}}} \quad (2.29)$$

A binary star system can also lose angular momentum through an interaction with a third (or tertiary) star. In recent years, evidence has been amassing for the formation through this pathway. In this pathway, two stars begin in a stable orbit. When a third star is introduced into the system, it steals angular momentum from the first two stars, resulting in a closer orbit. There is evidence that this companion stays in orbit around the contact binary. A study by Pribulla and Rucinski [2006] has established a lower limit of  $42\% \pm 5\%$  on the fraction of contact binaries in orbit with another star. In a search of 13,927 eclipsing binaries in the SuperWASP catalog, 24% had period-changes indicating a closely orbiting companion [Lohr et al., 2015]. The presence of tertiary components around specific components has also been detected via spectral imaging [Hendry and Mochnacki, 1998].

In these three-body situations, the inner two bodies (in our case, the two components of that will be the contact binary) lose angular momentum, through a mechanism called the Kozai-Lidov mechanism. In the Kozai-Lidov mechanism , the orbit of two inner bodies is perturbed by a third body orbiting farther out. In the equations of motion for the three-body system, angular momentum is conserved:

$$L_z = \sqrt{1 - e^2} \cos i \quad (2.30)$$

Because the quantity  $L_z$  is conserved, orbital eccentricity  $e$  can be traded for orbital inclination  $i$ . Three body systems with undergo Kozai-Lidov cycles, with a certain characteristic period:

$$T_{\text{Kozai}} = 2\pi \frac{\sqrt{GM}}{Gm_2} \frac{a_2^3}{a^{\frac{3}{2}}} (1 - e_2^2)^{\frac{3}{2}} \quad (2.31)$$

During these Kozai-Lidov cycles, the inner two bodies can tidally interact, resulting in a decrease of their separation. The Kozai-Lidov mechanism can result in much faster angular momentum loss than the magnetized wind mechanism.

Whether the binary system has lost angular momentum via a tertiary component or a magnetized wind, the contact stage begins when there is mass transfer from the primary to the secondary, resulting in a system with an isothermal common envelope.

## 2.12 Evolution in the Contact State

Mass transfer does not occur for all stars that come into close proximity. As we discussed in §2.8, the characteristics of observed contact binaries suggest that one component is nearer to ZAMS, and the other is nearer to TAMS. In Fig. 22, note how the secondaries (diamonds) have a mass-radius relation that is characteristic of TAMS stars, and the primaries (asterisks) have a mass-radius relation that is characteristic of ZAMS stars. The typical contact binary enters the contact stage when it is at least 4-5 Gyr old [Stepien, 2006a]. Only the combination of a TAMS and ZAMS star can fulfill the mass-radius relationship for contact binaries, while simultaneously being in thermal equilibrium. In other words, the components of most systems do not appear to have the same evolutionary state.

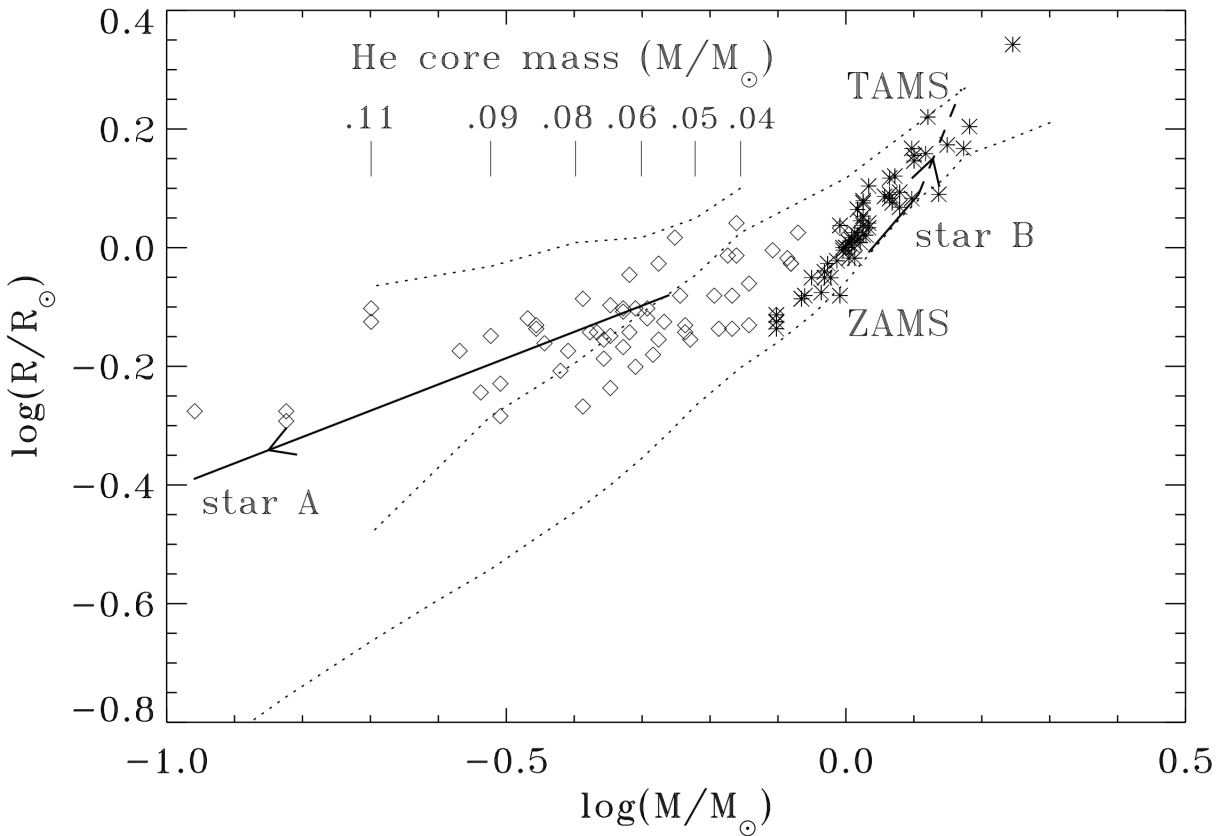


Figure 22: Radii and masses of 100 well-observed contact binaries. Asterisks (\*) denote the primaries, and diamonds denote the secondaries. Notice the dotted lines: the ZAMS mass-radius relation is plotted as the lower dotted line, and the TAMS mass-radius is plotted as the upper dotted line. (Fig. 1 from [Stepien, 2006a].)

As soon as the two components enter contact, the component that is closer to TAMS starts transferring mass onto the ZAMS component. The ZAMS component then becomes the more massive primary, while the helium-rich TAMS component becomes the secondary. Models predict that the mass of the secondary component progenitor (before mass transfer) ranges from 1 to  $2.5 M_{\odot}$  [Yıldız and Doğan, 2013].

After the mass-transfer occurs the system becomes stable and slowly loses angular momentum through a magnetized wind. The story of the evolution of a contact binary is the story of the evolution of its orbital angular momentum, or  $H_{\text{orb}}$ . For a binary system, the orbital angular momentum can be computed:

$$H_{\text{orb}} = \sqrt{GM_{\text{tot}}^3 \frac{aq^2}{(1+q)^4}} \quad (2.32)$$

where  $q$  is the mass ratio of the binary. As we can see in Eqn. 2.32, a decrease in  $H_{\text{orb}}$  can be caused by a decrease in the separation  $a$  between the two components (with all other variables held constant). With all other variables held constant, an increase in the mass ratio  $q$  also has the effect of decreasing  $H_{\text{orb}}$ .

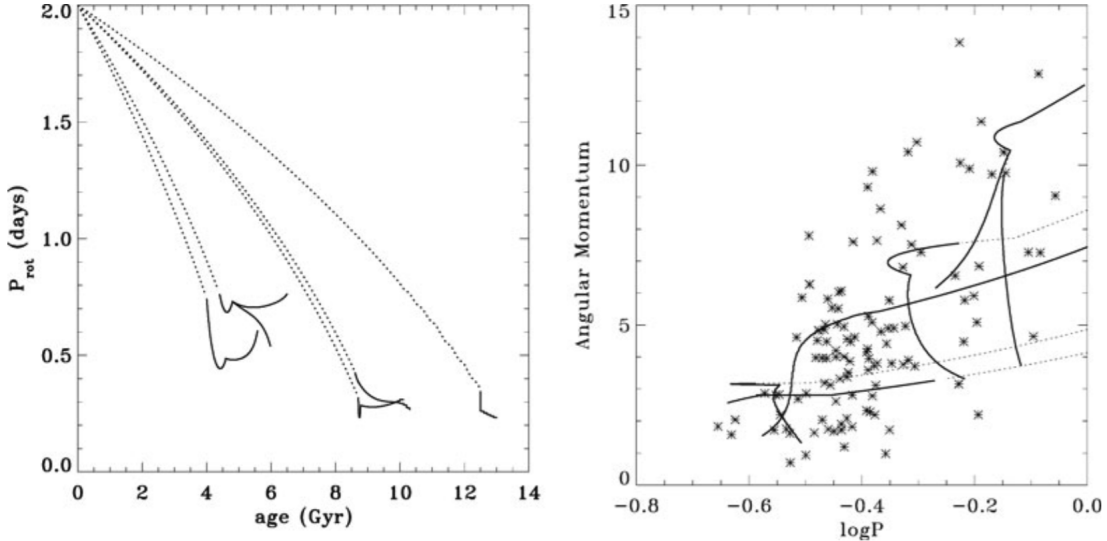


Figure 23: The period (left panel) and angular momentum evolution (right panel) of six contact binary models. The models are differentiated by mass, with the highest-mass binaries having the shortest lifetimes. All of the models start as detached binaries with an initial orbital period  $P_0 = 2.0\text{d}$ , but lose angular momentum through a magnetized wind (denoted by dashed lines). Then the binaries come into contact and change their period through mass-transfer (denoted by solid lines). The orbital angular momenta of known systems are plotted as crosses ( $\times$ ) in the right panel. (Fig. 1 from Stepień and Gazeas [2008]).

During evolution in the contact state, angular momentum loss due to a magnetized wind causes the separation of the two components to decrease. Mass transfer from the secondary onto the primary component causes the separation of the two components to increase. These two effects balance to keep contact systems in shallow contact ( $0.15 \leq f \leq 0.5$ ) throughout their lifetimes (Fig. 23).

Some of the most recent modeling work indicates that the typical duration of the contact state is 1 to 1.5 Gyr, but the orbital period distribution shows that the lifetime of the contact state is certainly not greater than 3 Gyr [Li et al., 2007, Gazeas and Stępień, 2008].

Because of self-regulating mechanisms in the contact state, and the homogeneity of main sequence stars, there are well defined relationships between the mass  $M$ , luminosity  $L$ , mass-ratio  $q$ , and orbital period  $P$  of contact binary stars [Gazeas, 2009, Awadalla and Hanna, 2005]. This enables them to be used as distance tracers: by observing a contact binary's

period, we can calculate its luminosity [Chen et al., 2016].

One of the most striking features of contact binary stars as a population is the existence of the “short-period” limit. If we look at the distribution of periods of contact binary stars, we find that there is a sharp cutoff in the distribution, which is not due to observational discovery-selection effects (Fig. 24) [Rucinski, 2007, Lohr et al., 2012, Drake et al., 2014a].

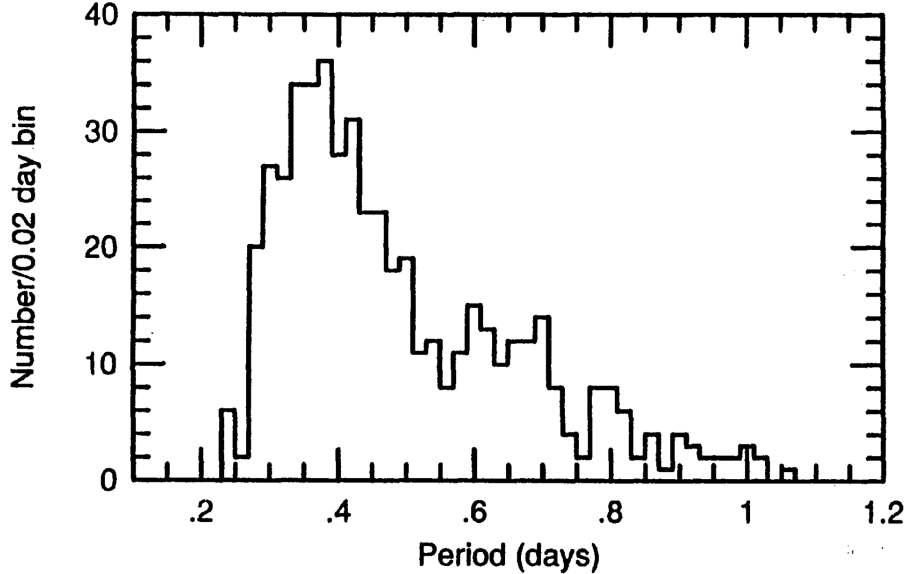


Figure 24: The period distribution of contact systems in the 4th edition of the General Catalogue of Variable Stars. Notice the sharp cutoff at  $P_{\text{orb}} = 0.22$  days. (Fig. 1 from Rucinski [1992]).

Rucinski [1992] found that the Hayashi full-convection limit was not the reason for the sharp period cutoff at  $P_{\text{orb}} = 0.22$  days. A compelling theory is that the progenitors of extremely low-mass contact binaries have not yet had the time to evolve to TAMS, and have thus been unable to undergo the mass-transfer necessary to become a contact binary [Stepien, 2006b]. Thus the period cutoff is set by the age of the universe.

## 2.13 Evolution out of the Contact State

It is generally accepted that the contact state of binary evolution ends with the inspiral and merger of the two components. The merger event is where the contact system becomes dynamically unstable, and rapidly coalesces into a single, rapidly rotating star. This is caused when the system “runs-out” of angular momentum  $H_{\text{tot}}$ . In more precise language, the system becomes unstable when it cannot lose angular momentum  $H_{\text{tot}}$  by change of the separation  $a$  of its components:  $\frac{dH_{\text{tot}}}{da} = 0$ . When we assume a synchronized system and ignore the spin angular momentum of the secondary component, we can write the total angular angular momentum  $H_{\text{tot}}$  as:

$$H_{\text{tot}} = H_{\text{orb}} + H_{\text{spin}} = \mu a^2 \Omega + M_1 k_1^2 R_1^2 \Omega \quad (2.33)$$

Where  $M_1$  and  $R_1$  are the mass and radius of the primary.  $\mu = M_1 M_2 / M$ ,  $M = M_1 + M_2$ ,  $k_1$  is a dimensionless gyration radius, which depends on the structure of the star.  $\Omega = \sqrt{\frac{GM}{a^3}}$ .

We can find the instability condition by setting  $\frac{dH_{\text{tot}}}{da} = 0$ , which yields two equivalent criteria:

$$\frac{a_{\text{inst}}}{R_1} = k_1 \sqrt{\frac{3(1+q)}{q}} \quad \text{or} \quad H_{\text{orb}} = 3H_{\text{spin}} \quad (2.34)$$

Notice how the mass-ratio  $q$  figures into this equation. We can use the equations of stellar structure, in conjunction with Eqn. 2.34 to express the limit of stability as a minimum *mass-ratio*  $q$ , as a function of fill-out factor  $f$ . Using this method, the minimum mass-ratio for contact-binaries is calculated to be  $q_{\min} = 0.070$  to  $0.074$ , depending on fill-out factor  $f$  (see Fig. 25).

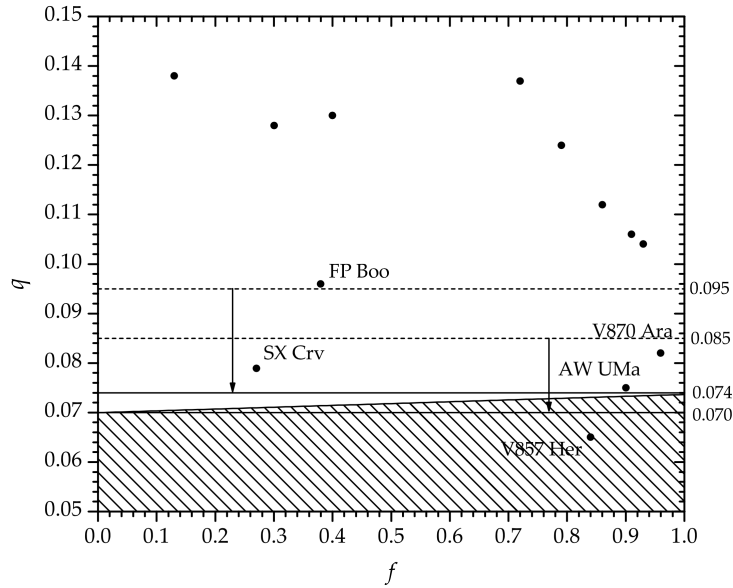


Figure 25: The mass-ratio limit  $q_{\min}$  as a function of fill-out factor  $f$ . Several systems that are near the limit are plotted as black points. (Fig. 1 from Arbutina [2009]).

As we learned in §2.12, the secondary of the contact binary transfers mass onto the primary after contact begins. As the system loses angular momentum, the separation between the two components must decrease, bringing the two components into better thermal contact. In response to this change, mass is transferred from the secondary to the primary, causing the mass ratio to decrease. This has the effect of increasing the separation between the two components. When the secondary transfers enough mass such that  $q = \frac{M_2}{M_1} \leq 0.070$  to  $0.074$ ,

a tidal instability develops. Some models predict that the systems merge into a single, rapidly rotating star on the timescale of  $10^3$  to  $10^4$  years [Rasio, 1995].

The merger of a contact binary star has been observed [Tylenda et al., 2011]. A “red nova” event was observed in the constellation of Scorpius in late 2008. When archival data was examined, it was revealed that a contact binary system had existed at the nova’s precise location (see Fig. 26). In the years preceding the red nova event, it was discovered that the period of the contact binary (called V1309 Sco) was decreasing (see Fig. 27). This period decrease was the onset of the instability that caused the two components to merge. As the components merge in dynamical time, the hydrogen reaction rate increases by orders of magnitude, resulting in a dramatic increase in brightness seen as the peak in Fig. 26.

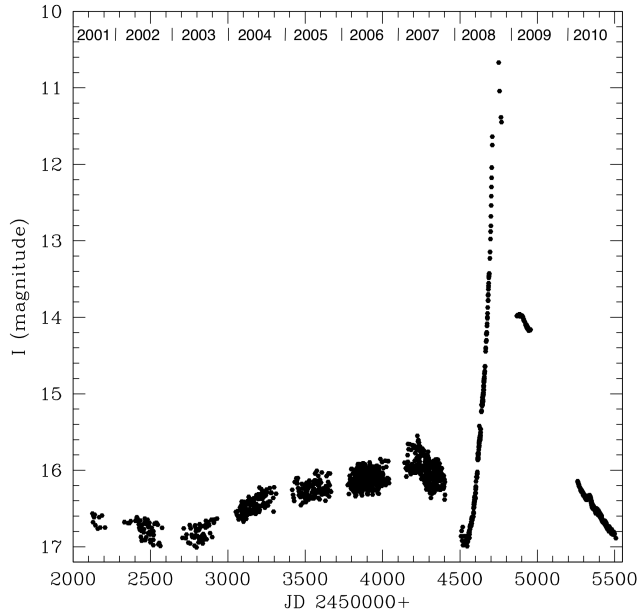


Figure 26: Light-curve of V1309 Sco from the OGLE-III and OGLE-IV projects:  $I$  magnitude versus time of observations in Julian Dates. Time in years is marked on top of the figure. At maximum the object attained  $I \approx 6.8$ . (Fig. 1 from Tylenda et al. [2011]).

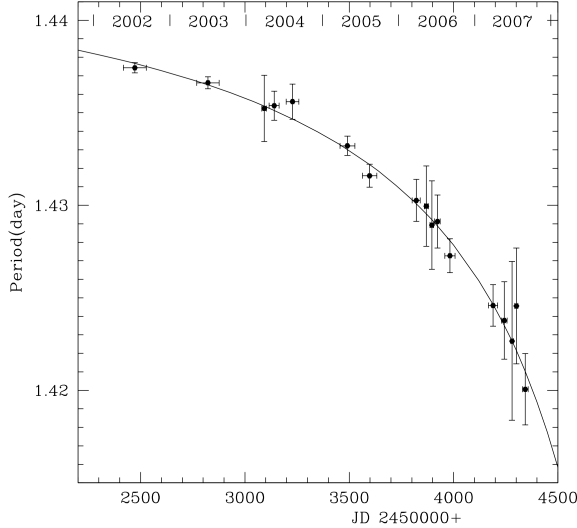


Figure 27: The evolution of the orbital period of V1309 Sco in the years before the merger event. Note the exponential decrease of the solid curve fitted to the data. (Fig. 2 from Tylenda et al. [2011]).

By looking for contact binary systems with rapidly decreasing orbital periods, we can find systems that are likely to merge. Period decay has been detected in the Kepler data of the contact binary KIC9832227 that is very similar to the period decay observed by Tylenda et al. [2011]. In this manner, a merger of a contact binary has been predicted in the year of  $2022.2 \pm 0.6$  [Molnar et al., 2017].

Another piece of evidence that supports the hypothesis of the contact binary state ending in a merger event is the presence of a special type of star called a *blue straggler* [Andronov et al., 2006]. A blue straggler is a star that appears to have a main-sequence lifetime that is longer than it should be, given the star's mass. Blue stragglers are frequently discovered in globular clusters. In a Hertzsprung-Russell diagram of a globular cluster, blue stragglers appear as outliers: they are the stars that remain after stars of similar mass have “turned-off” the main sequence moving upwards. The location of blue stragglers in a HR diagram is denoted by the dotted lines in 28.

Short period eclipsing binaries have been found amongst blue stragglers in the globular cluster NGC5466 (Fig. 28) [Mateo et al., 1990]. The eclipsing binaries found in these globular clusters have similar brightnesses and colors to blue stragglers. It is likely that after the violent merging event, a contact binary transforms into a single, rapidly rotating star. The rotation of the star slows over time through AML via a magnetized wind, and it becomes a blue straggler.

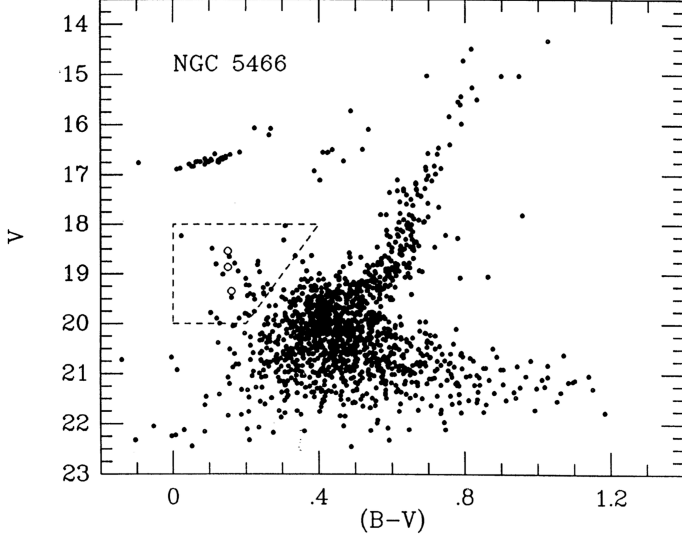


Figure 28: A color-magnitude diagram of globular cluster NGC 5466. The blue stragglers are defined to be all stars located within the region bounded by the dashed lines. The mean  $V$  magnitudes and  $(B - V)$  colors of the eclipsing binaries discovered by Mateo et al. [1990] are shown as open circles. (Fig. 1 from Mateo et al. [1990]).

## 2.14 Frequency and Density

In order to understand how long contact binary systems live, we need to know how common they are among main-sequence stars. The contact binary *frequency* describes the fraction of main-sequence stars that are in a contact binary system. We would also like to know how many contact binary systems there are, per volume in galactic space. The contact binary *density* describes the number of contact binary systems per cubic parsec.

Contact binaries are the most frequently observed type of eclipsing binary star, because their eclipses can be detected at a wide range of orbital inclinations. In recent searches for eclipsing binary stars in survey data [Drake et al., 2014b] contact binary stars comprised 50% of the new variable stars discovered.<sup>1</sup>

Studies using OGLE survey data on the galactic bulge (Baade's Window) indicates that the frequency of contact binaries relative to main sequence stars is approximately  $\frac{1}{130} = 0.7\%$  in the absolute magnitude range of  $2.5 < M_v < 7.5$  [Rucinski, 1998]. A later study using ASAS survey data shows that the frequency is 0.2% in the solar neighborhood [Rucinski, 2006] in the absolute magnitude range of  $3.5 < M_v < 5.5$ . A catalog of 1022 contact binary systems in ROTSE - 1 survey data placed the spatial density of contact binaries at  $1.7 \pm 10^{-5} \text{ pc}^{-3}$  [Gettel et al., 2006].

---

<sup>1</sup>To find suitable contact binary targets for observation by a small observatory, see Pribulla et al. [2003], an excellent catalog of contact binaries in the field.

There is a high level of consistency between frequency measurements, suggesting that the true frequency is in the range of  $0.002 - 0.008$ . This is very similar to the frequency of short-period detached binaries, which is  $0.003 - 0.007$  [Duquennoy and Mayor, 1991]. The similarity indicates that the lifetime of a binary in the contact phase is of the same order of magnitude as the lifetime in the detached phase [Stepien, 2006a].

## 2.15 Early-Type Contact Binaries

There is a type of contact binary that is so special that it merits its own section. The contact binaries that we have been talking about in the previous section have been low-mass, meaning that each of the components has a mass of less than  $1.6M_{\odot}$ . However, astronomers have found several massive O-type contact binaries, with component masses of close to  $40M_{\odot}$ . Early-Type contact binaries deserve a special section due to their extreme mass, luminosity, rarity, and short lifetime. These massive contact binaries are significantly different from their solar-mass counterparts, and are particularly exciting because they provide a mechanism for placing two black holes in close proximity.

When astronomers say that a star is “Early-Type”, they mean that it is “early” on the spectral classification sequence (OBAFGKM). O and B stars are more massive, more luminous and hotter than our sun. There are only a handful of O and B Type contact binary systems known. The four best studied systems are TU Muscae [Penny et al., 2008], MY Cam [Lorenzo et al., 2014], UW CMa [Antokhina et al., 2011], V382 Cygni [Popper, 1978].

These massive O and B type contact binaries are very different from less massive (F,G,K, or M type) contact binaries. Because O and B type stars have such short life-times, O and B type contact binaries are especially short-lived. Also, very few O and B type contact binaries are formed, because the stellar initial mass function (IMF) is heavily skewed towards low-mass  $M$  stars. The combination of these two effects makes massive O and B type contact binaries exceedingly rare. In fact, less than 10 systems have been discovered so far.

Early-Type contact binaries are some of the most luminous stellar objects: they can be seen at extragalactic distances [Lee et al., 2014, Vilardell et al., 2006]. Their period-luminosity relationship can even be used to precisely measure the distance to the contact-binaries in M31, or the Magellanic clouds[Hilditch et al., 2005, Priya et al., 2013, Rucinski, 2006].

## 2.16 Magnetic Activity

In stellar atmospheres, the convective movement of stellar plasma creates magnetic fields, which in turn affect the motion of that same plasma (§2.9). Contact binaries are rapidly rotating systems, with orbital periods of 0.2 to 0.8 days (compare this rate with the ap-

proximately 30 day rotational period of the sun), so they have the potential to form much stronger magnetic fields. As a result, they exhibit dramatic magnetic phenomena.

There is a lot of evidence that contact binary stars have strong magnetic fields. Astronomers observe changes in their light-curves, indicating that starspots may be appearing and disappearing on their photospheres [Borkovits et al., 2005, Shengbang and Qingyao, 2000, Kaszás et al., 1998, Qian et al., 2007, Lee et al., 2004, Yang et al., 2012, Zhang and Zhang, 2004, Gazeas et al., 2006]. Starspots are magnetic phenomena, and so their occurrence is related to the magnetic activity of their host star [Berdyugina, 2005]. Doppler imaging of contact binaries can reveal the shapes and locations of the starspots on the photosphere (see Fig. 29) [Barnes et al., 2004]. In addition, doppler imaging has been used to track the evolution and migration of starspots on contact binaries [Hendry and Mochnacki, 2000]. More recently, Kepler data has been used to perform starspot tracking [Tran et al., 2013, Balaji et al., 2015].

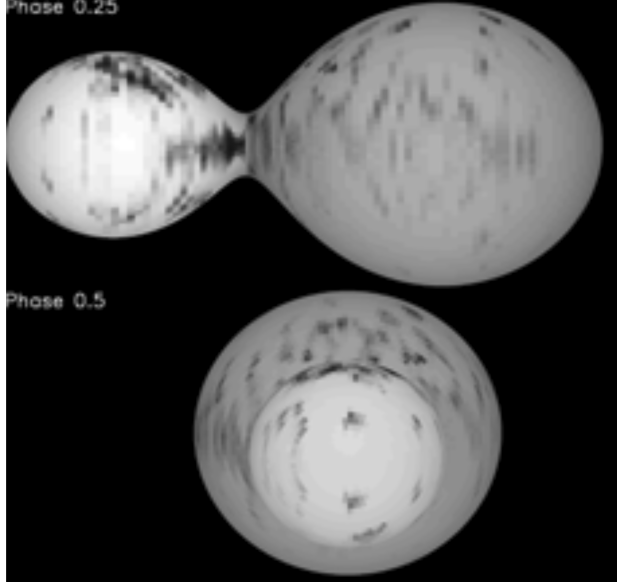


Figure 29: An image of the surface brightness of the contact binary star AE Phe, showing that it is heavily spotted. (Fig. 5 from Barnes et al. [2004]).

The sun goes through cycles of magnetic activity, with a period of 11 years, where the solar magnetic field gets stronger, and then weaker [Balogh et al., 2015]. Oscillations in the magnetic field strength may cause contact binaries to undergo similar orbital period and luminosity changes. The first comprehensive theory for this modulation in close binary systems was formulated in the early 1990's by John Applegate [Applegate, 1992, Lanza, 2006].

Flares have been observed on contact binary systems. Observations in visible light [Qian et al., 2014] (see Fig. 30), in ultraviolet bands [Kuhi, 1964], in x-ray wavelengths [McGale

et al., 1996], and in radio wavelengths [Hughes and McLean, 1984, Vilhu et al., 1988] have supported the occurrence of large flares. During a continuous monitoring campaign in the winters of 2008 and 2010, Qian et al. [2014] observed a contact binary system CSTAR 038663 ( $P = 0.27$  days,  $T_1, T_2 = 4616\text{K}, 4352\text{K}$ ) for a total of 4167 hours (174 days) in the SDSS  $i$  band using the CSTAR telescope array in the Antarctic. In this time, Qian et al. [2014] discovered 15  $i$  band flares, revealing a flare rate of 0.0036 flares per hour. These 15 flares had durations ranging from 0.006 to 0.014 days (9 to 20 minutes), and amplitudes ranging from 0.14 - 0.27 magnitudes above the quiescent magnitude. In 1049 close binaries observed by Kepler, Gao et al. [2016] have identified 234 “flare binaries”, on which a total of 6818 flares were detected.

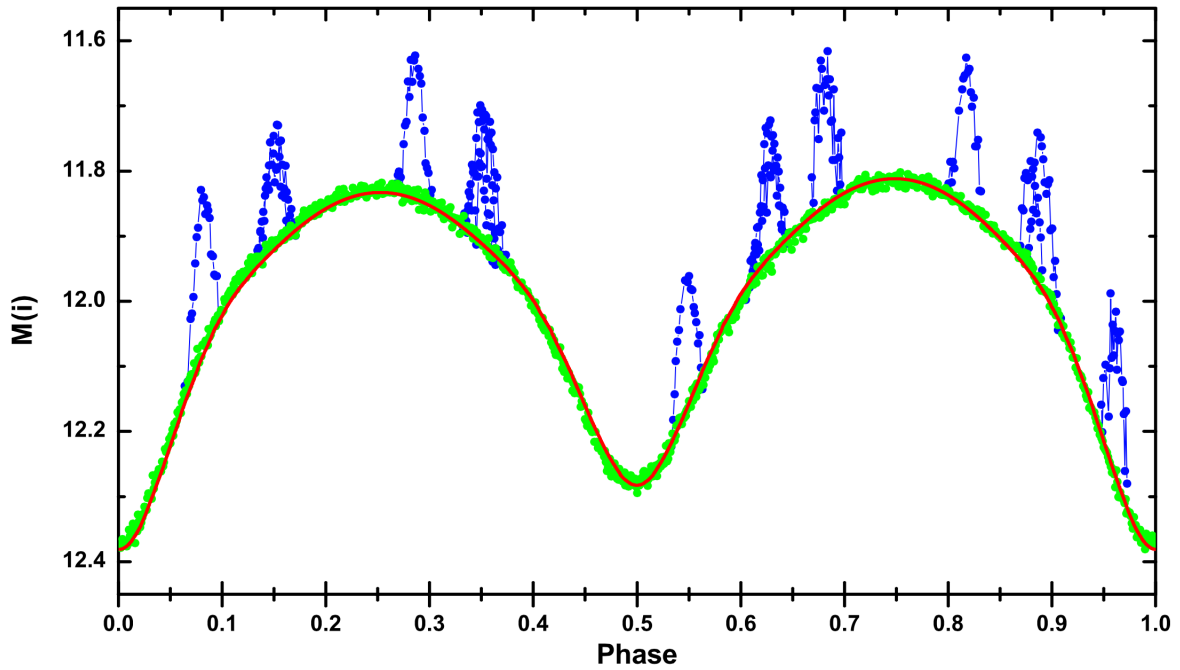


Figure 30: A light-curve of a contact binary that shows 11 flares visible in the  $i$ -band. (Fig. 15 from Qian et al. [2014]).

### 3 Observations and Analysis Techniques

Astronomy is unique as a science because almost all the information that can be obtained from an object in the sky comes to us as electromagnetic waves. Perhaps *THE* question in observational astronomy is: “What can we learn from these electromagnetic waves?”. The study of contact binary stars is no different. In this section, we will learn the ways that researchers study electromagnetic waves from contact binary stars.

#### 3.1 Images of Contact Binaries

The oldest type of astronomical information is image data: “What do I see when I look through the telescope?”. To put this question in more formal language: “What is the distribution of the intensity of visible light as a function of position?”. When we look at the moon, for example, we can learn a lot about it: we might see some crater “over here”, with a given size, shape, color, etc. We might see a dark lunar mare (or “sea”), “over there”, with another size, shape, color, etc. The moon is what we call a “resolved source”, meaning that features on it are distinguishable: we can separate “over here” from “over there”. In other words, the distance between “over here” and “over there” is larger than the resolution limit of our telescope. Let’s see if we can reasonably obtain image data from a contact binary:

On a still, clear night at the Las Campanas observatory in Chile, the atmospheric resolution limit (or “seeing”) is 0.5 arcseconds. This is the best resolution that can be expected from a telescope on earth.

$$0.5 \text{ arcseconds} * \frac{1}{3600} \frac{\text{arcseconds}}{\text{degrees}} = 1.4 \times 10^{-4} \text{ degrees} * \frac{\pi}{180} \frac{\text{radians}}{\text{degrees}} = 2.4 \times 10^{-6} \text{ radians} \quad (3.1)$$

In order to distinguish between the two components of a contact binary, the resolution limit of our telescope must be smaller than the distance between the centers of the two components.

For a contact binary star of solar type, this is about two solar radii:  $2R_{\odot} = 2 \times (6.957 \times 10^5) \text{ km}$ . Let us place this hypothetical contact binary at the same distance as the nearest star, *Proxima Centauri*, which is 4.243 light years = 1.301 parsecs =  $4.014 \times 10^{13} \text{ km}$ .

To calculate the angle that a solar type-contact binary at the distance of *Proxima Centauri* would subtend, we will use the small angle approximation:

$$\sin(\theta) \approx \theta, \quad \cos(\theta) \approx 1 - \frac{\theta^2}{2}, \quad \tan(\theta) = \frac{\sin(\theta)}{\cos(\theta)} = \frac{\theta}{1 - \frac{\theta^2}{2}} \Rightarrow \tan(\theta) \approx \theta \quad (3.2)$$

If we set up a right triangle (as in Fig. 31), we see than the tangent of the angle  $\theta$  is equal to the diameter of the sun divided by the distance to *Proxima Centauri*.

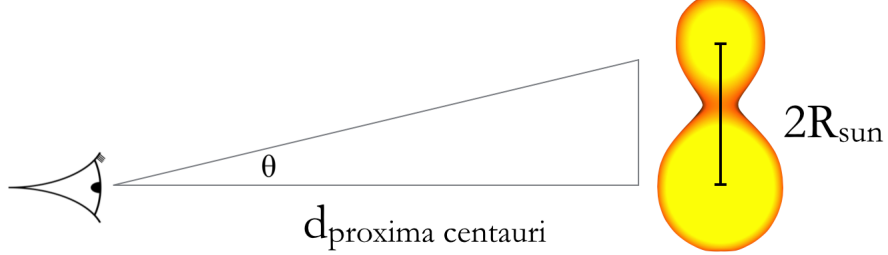


Figure 31: Calculating the angle  $\theta$  subtended by a solar-type contact binary at the distance of the nearest star.

$$\frac{2R_{\text{sun}}}{d_{\text{proxima centauri}}} = \frac{2 \times (6.957 \times 10^5) \text{ km}}{4.014 \times 10^{13} \text{ km}} = \tan(\theta) \approx \theta = 3.466 \times 10^{-8} \text{ radians} \quad (3.3)$$

When comparing the resolution necessary to distinguish the components of a contact binary to the best resolution possible on earth:

$$\frac{3.466 \times 10^{-8} \text{ radians}}{2.4 \times 10^{-6} \text{ radians}} \approx 0.02 \quad (3.4)$$

To summarize: we would need 50 times the resolving power achievable from the earth to obtain image data from a large contact binary at the distance of the nearest star. In actuality, the situation is even worse. 44 Bootis is the nearest contact binary system to earth, at a distance of 13 parsecs (42 light years) it is 10 times further away than *Proxima Centauri* [Eker et al., 2008]. For this reason, we cannot obtain usable image data from contact binaries <sup>2</sup>.

### 3.2 Photometry of Contact Binaries

In images, contact binaries appear as an unresolved point source. At first glance, it may appear that astronomers are stuck: they cannot “see” the contact binary and so must remain uncertain about its characteristics. However, as Kempf and Müller learned in 1903, the

---

<sup>2</sup>it is possible to achieve this resolution (as good as 0.0005") through long-baseline interferometry. Using the CHARA array on Mount Wilson, researchers have constructed a resolved image of the eclipsing binary system  $\beta$  *Lyrae* [Zhao et al., 2008]. However, interferometric imaging is only possible for the brightest stars, so is not useful for contact binaries.

amount of light received from a contact binary varies as a function of time. This function is called the light-curve:

$$f(\text{Time}) = \text{Flux Received at Telescope} \quad (3.5)$$

A light-curve is constructed from observations. An astronomer can sample the light-curve and approximate its true shape by repeatedly measuring the brightness of the source over a certain time span.

Kempf and Müller knew that they could use the light-curve to learn about the shape of the contact binary system. First, they noted that the light-curve was periodic: after a certain amount of time, the trend in flux *exactly repeated* itself. Thus they inferred that the process that was responsible for the variation in the flux was cyclical in nature.

They observed that the period of the light variation in W UMa was very stable (“The error of the period can hardly be more than 0.5s...”). They assumed that a rotational or orbital mechanism was responsible for the light variation. They thought that the light-curve shape might be caused by the presence of a large dark spot on a rapidly rotating single star, which was hypothesized to be “in an advanced stage of cooling”. However, W UMa was a hotter white star, not a cool red star, leading Kempf and Müller to discredit this model (hotter stars do not have the convective envelope necessary to form surface magnetic fields). They also considered a single star in the shape of an ellipsoid, however they calculated that this model did not describe the shape of the light-curve very well. In 1903, the eclipsing binary model was already proposed as a mechanism for the light-curves of certain stars (most notably Algol). To construct their model, they looked at existing eclipsing binary light-curves and imagined what would happen if they brought the two stars close together. If they brought the two stars close enough together so that the stars were almost touching, there was always variation in the light-curve, just like they observed.

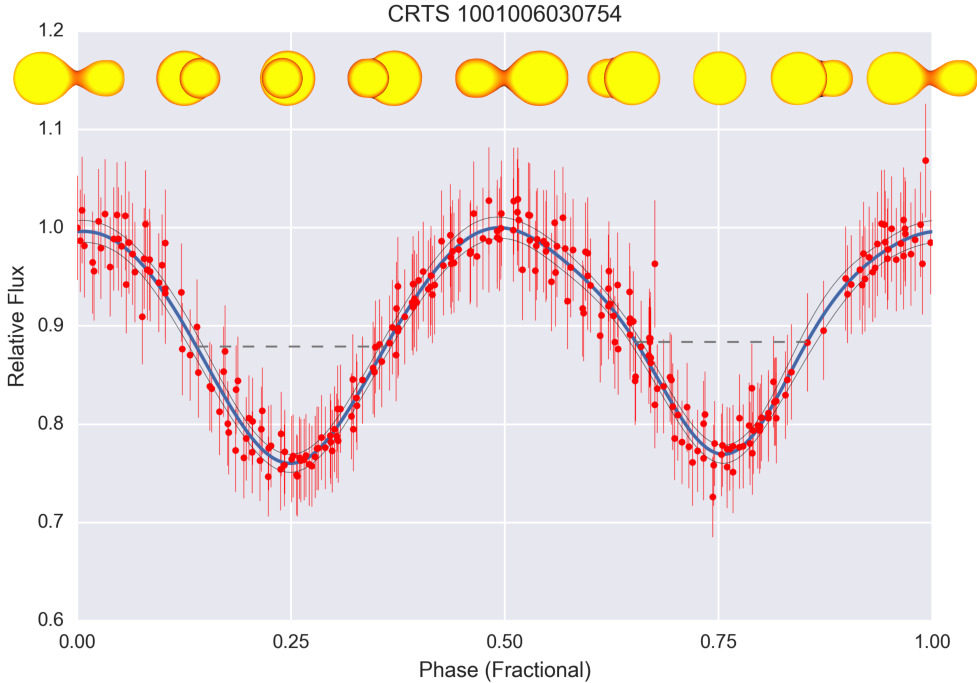


Figure 32: Light-curve is from CRTS data [Drake et al., 2014b]. Illustration of contact binary phase from an animation at: <http://cronodon.com/SpaceTech/BinaryStar.html>

The light-curve of a system with two (relatively) small and cool  $M$  type components should be qualitatively and quantitatively identical to the light-curve of a system with two massive and hot  $G$  type components, given the systems have the same geometry  $[f, q, i]$ . The shape of a contact binary's light-curve can tell us a lot about it (Fig. 32).

### 3.3 Spectra of Contact Binaries

Time-series spectra are some of the most complete observations of contact binaries (Fig. 33). By fitting a blackbody curve to the spectrum of a star, we can calculate its temperature to greater precision than we can by using color filters. In addition, spectral features of a known wavelength can be used to measure the velocity of the source. Contact binaries are rapidly rotating systems, which causes spectral lines to be broadened. Abundances of elements cannot be determined precisely due to the broadening and blending of spectral lines caused by the fast rotation [Gazeas and Niarchos, 2006]. The analysis of the rotational velocities of contact binaries is especially challenging because unlike some binary systems, the two components are of approximately equal brightness. To calculate the mass ratio of a system  $q$ , the spectrum must be deconvolved. Spectrum-deconvolution techniques produce values of  $q$  accurate to a few percent [Rucinski, 1993a, Hrivnak, 1989].

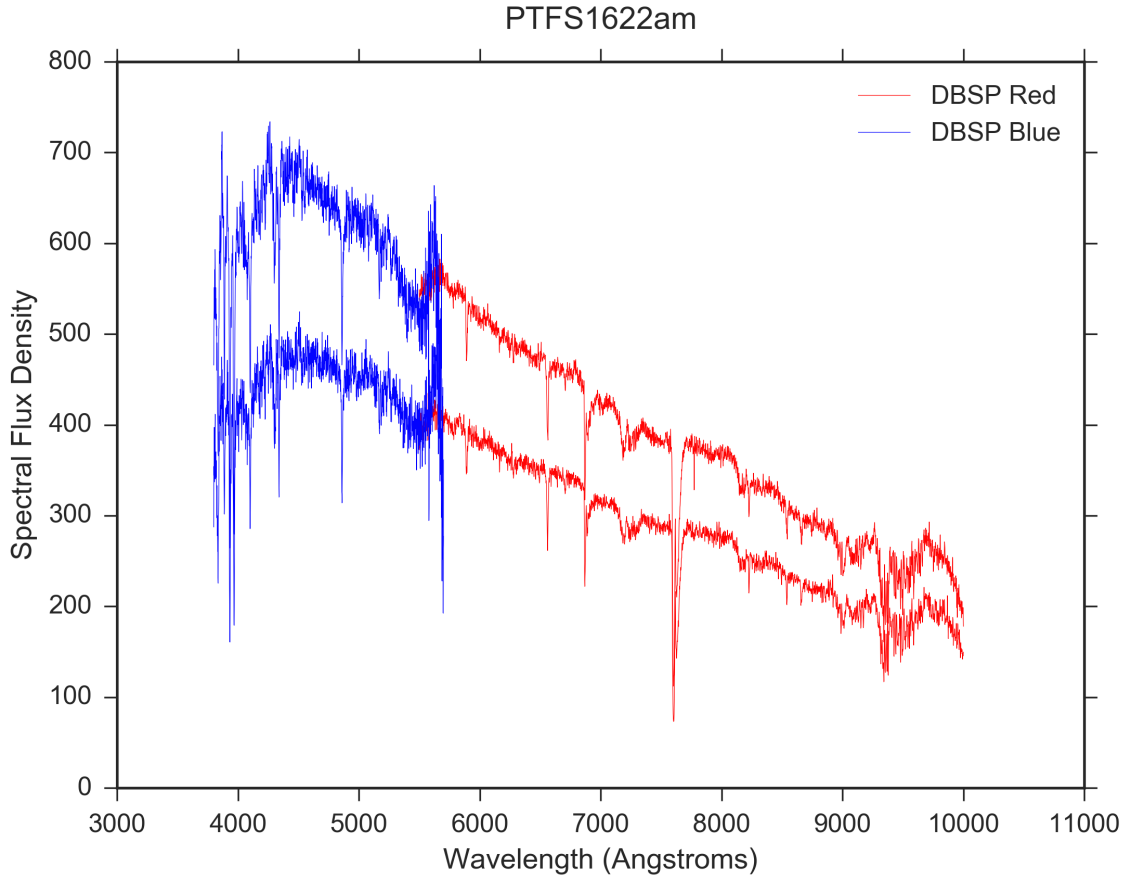


Figure 33: Two spectra of the contact binary star PTFS1622am in data from the Double-Beam Spectrograph at the 200" Hale Telescope taken by the author. The two colors indicate the separate chips that the spectra was observed on. The Spectral Flux Density is in arbitrary units, what is more important is to observe the relative flux.

### 3.4 X-ray and Ultraviolet Data on Contact Binaries

Contact binaries are much brighter than main-sequence stars in the ultraviolet, owing to their strong magnetic fields cause by rapid rotation. Earth's atmosphere is opaque to X-ray and ultraviolet (UV) light, but the advent of space-based observatories has made observations of the sky possible in these passbands.

The first X-ray survey of contact binaries was conducted by the *Einstein* satellite [Crudace and Dupree, 1984]. The *Extreme Ultraviolet Explorer* and *ROSAT* satellites have been used to observe contact binaries in the ultraviolet (Fig. 34) [Vilhu and Walter, 1987, Stepień et al., 2001]. Ultraviolet observations provide information about the coronal structure of contact binary systems.

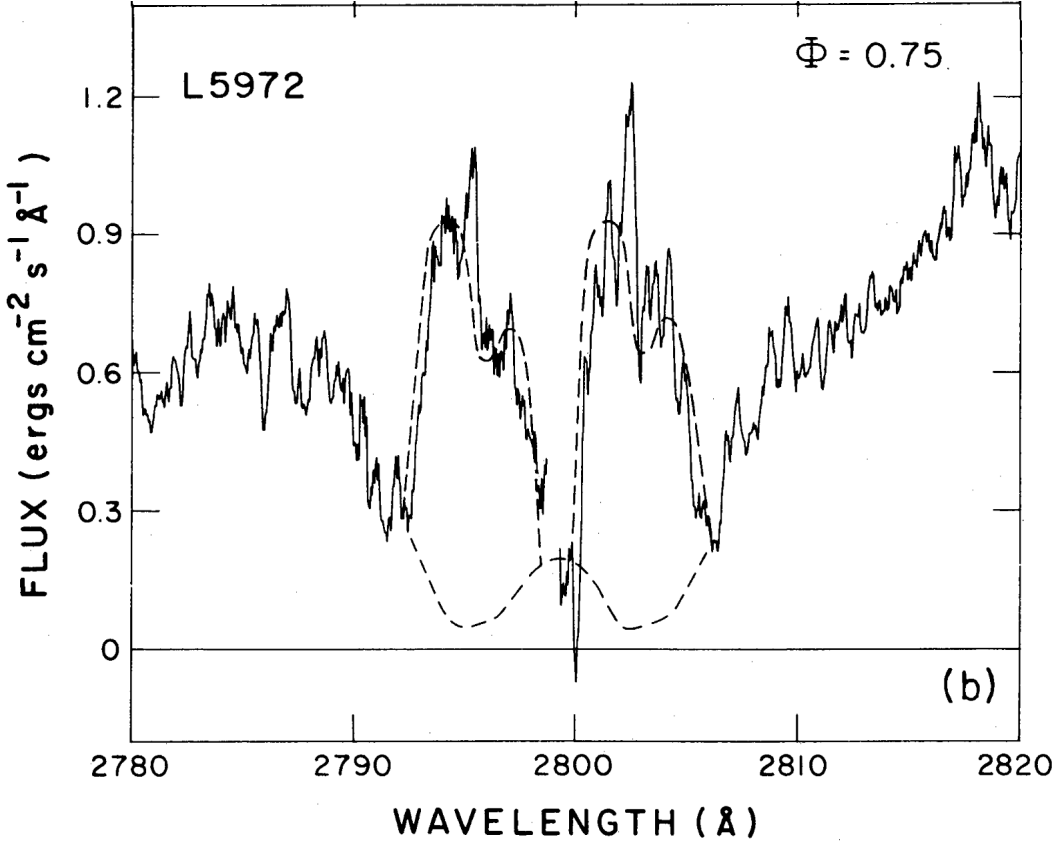


Figure 34: An ultraviolet spectrum of the magnesium II  $h$  and  $k$  emission lines on the contact binary W UMa. The presence of these lines is indicative of chromospheric activity. (Fig. 1 from Vilhu and Walter [1987]).

### 3.5 Physical Light-Curve Modeling

In this section, we will learn how astronomers convert light-curves and spectra of contact binaries into measurements of physical parameters of the systems. Some parameters that can be measured for contact binary stars are the component masses  $M_1, M_2$ , the component luminosities  $L_1, L_2$  and temperatures  $T_1, T_2$ , the system inclination  $i$ , and the fill-out factor  $f$ .

In §3.2, we learned that contact binary light-curves contain information about the physical nature of the system. Since the majority of data on contact binaries is in the form of photometric light-curve measurements, there has been much effort spent on refining the process of light-curve analysis.

Physical models of contact binary systems (like those of Lucy [1968a]) can be used to simulate light-curves. By computing the surface brightness of the system across the visible area, the total flux from this theoretical system can be calculated for any orbital phase

and system inclination. In these models, the masses, radii, temperatures, and many other parameters can be varied to produce different light-curves. The goal of the physical modeling code is to find a combination of system parameters ( $M_1, M_2, L_1, L_2, T_1, T_2, i, f$ , etc...), that accurately reproduce the observed light-curve (see Fig. 35).

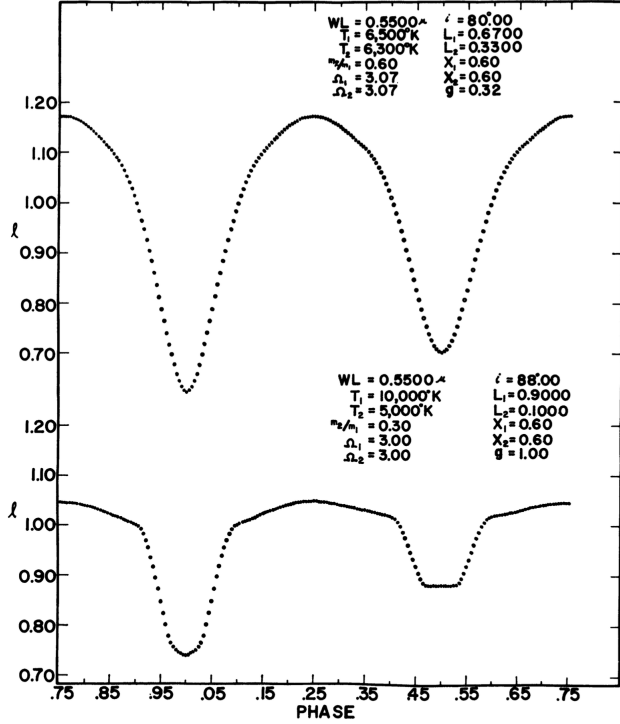


Figure 35: Theoretical light-curve models of two different eclipsing binary systems. The system at the top is a contact binary. Notice the list of system parameters used to generate the model:  $WL = 0.5500\mu$  indicates that the light-curve is generated in the visible wavelength of 550 nanometers.  $T_1, T_2$  indicate the temperature of each of the components of the contact binary, inclination  $i$ , luminosities, separations, and the gravity-darkening coefficient  $g$  are also reported. (Fig. 1 from Wilson and Devinney [1971]).

The modeling process is called the “inverse problem”, an observed light-curve is used to determine a set of orbital elements. This “inverse problem” is a non-linear least squares fit to many parameters, which is typically solved using a numerical gradient descent method. This process faces a whole host of problems that occur in nonlinear multiple-parameter fitting: parameter correlations, divergence, and the presence of several non-unique solutions [Kallrath et al., 1998].

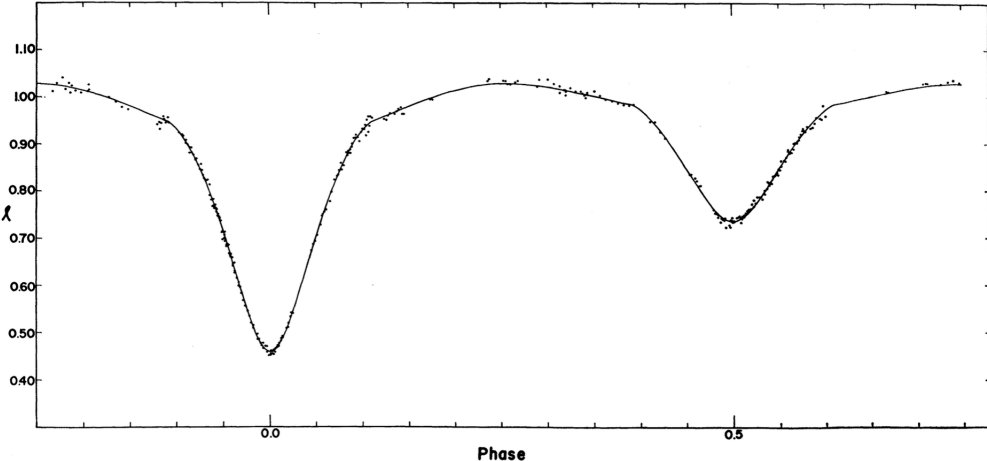


Figure 36: A theoretical light-curve of the eclipsing binary MR Cygni (the solid line), compared with observations (points). The fit is very good, leading researchers to believe the parameters reported by the fit. However, there is no guarantee that this fit points to a unique system solution. (Fig. 3 from Wilson and Devinney [1971]).

The Wilson-Devinney Code (hereafter WD code) was the first code that could produce contact binary light-curves in large quantities for a variety of system parameters [Wilson and Devinney, 1971]. The Python package `phoebe` is a user friendly implementation of the WD code in `python` developed by an international team of researchers, allowing a large number of scientists to fit physical models to light-curve data [Prša et al., 2013].

Unfortunately, at the ground based photometric uncertainty limit of  $\approx 0.01$  magnitudes, `phoebe` models based on observational data are almost always under-determined. There are so many free parameters in the models (which for example allow the user to also fit for starspots of various shapes and sizes, and to include the light of an unresolved tertiary component), many degenerate perfect fits to observed data can always be found (see Fig. 36). The degeneracy of these solutions is rarely if ever mentioned in the literature. For a complete solution of a contact-binary system, radial velocity data needs to be used to break degeneracies by providing an independent measurement of the system's total mass and mass-ratio . Simultaneous fitting of physical models of the contact binary light-curve and radial velocity data can provide solutions that are almost totally unique.

Due to their high photometric accuracy, light-curves from the Kepler mission can be used with the WD code (as implemented in `phoebe`) to great effect [Senavci et al., 2016]. New physics is being introduced into `phoebe`, which can be explored with the high-quality photometry from Kepler.

In summary, physical light-curve modeling is a powerful tool in the study of contact binary systems. When a physical analysis of the light-curve data is combined with radial-velocity data from spectroscopy, system parameters can be fully constrained. However, in

much of the literature, there are a large number of free parameters that are simultaneously fit to observations *without using radial-velocity data*, leading to the problem of non-unique parameter solutions for the same observational data. Researchers should be aware of this limitation when reporting their results.

### 3.6 Nomographic Light-Curve Solutions

As larger and larger numbers of contact binaries were discovered, astronomers saw the need for a less computationally intensive way of determining a system's geometrical elements from light-curve data. The nomographic method does not seek to produce a large number of system parameters, but rather seeks only to constrain the system geometry  $[f, q, i]$ . In the nomographic method, the physical model of the contact binary is used in reverse (as compared to §3.5). A catalog of models is produced, covering the parameter space of system geometry  $[0 \leq f \leq 1, 0 \leq q \leq 1, 0 \leq i \leq 90]$ . In the physical models used to compute the catalog of light-curves, isothermal envelopes are assumed, along with a simple gravity-darkening law. The light-curve that is observed by the telescope is then compared with the whole catalog of computed light-curves, and the closest match is interpreted as corresponding to the actual system parameters.

Mochnacki and Doughty [1972] was the first to propose a nomographic method. As large numbers of contact binary light-curves were being collected in the early 1990's, interest in nomographic solutions was revived. Rucinski [1973] derived two methods, one based on a Fourier decomposition of the light-curve, and the other based on measuring the eclipse half-widths. It was found that for systems with a light-curve amplitude  $A$  of greater than 0.3 magnitudes, the fill-out factor  $f$  could be calculated. Work with light-curves from the OGLE survey has determined a criterion for contact based on Fourier coefficients alone [Rucinski, 1997]. Rucinski [1993b] calculated an array of contact binary light-curves for 1500 possible combinations of  $[f, q, i]$  (Fig. 37). Fourier analysis has been used to find and characterize contact binaries in all-sky surveys [Coker et al., 2013].

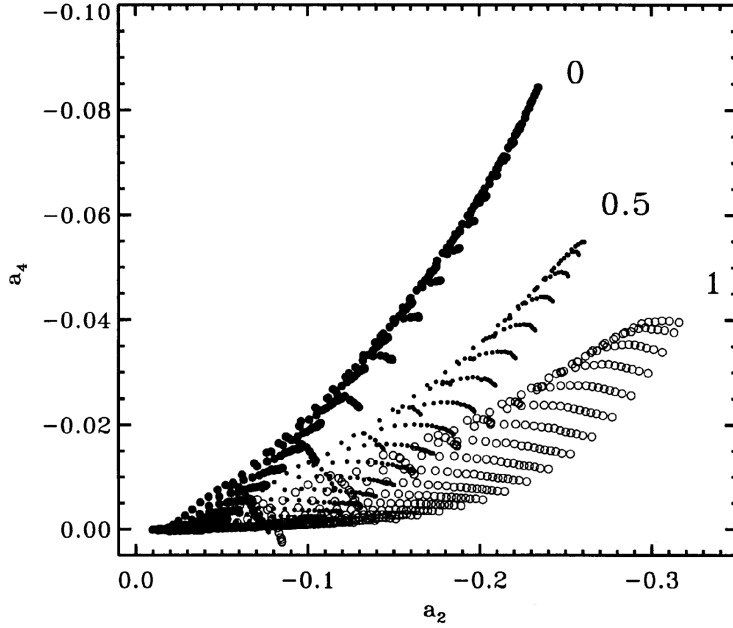


Figure 37: Relations between the two largest cosine coefficients  $a_2$  and  $a_4$ , for three values of the fill-out factor  $f = [0, 0.5, 1]$ . By measuring  $a_2$  and  $a_4$ , models can be differentiated from each other. Notice how sets of models with different fill-out factors  $f$  occupy different regions in the  $a_2$ - $a_4$  plane. (Fig. 6 from Rucinski [1993b]).

An advantage of this method is that the model degeneracy can be estimated. Often, (especially for systems with a low orbital inclination) many models will be supported by the observed data. One result from this analysis of degeneracy is that the mass-ratio ( $q$ ) as determined from the light-curve photometry ( $q_{ph}$ ) has been shown to be unreliable at low inclinations (Fig. 38) [Van Hamme and Wilson, 1985, Terrell and Wilson, 2005, Hambálek and Pribulla, 2013].

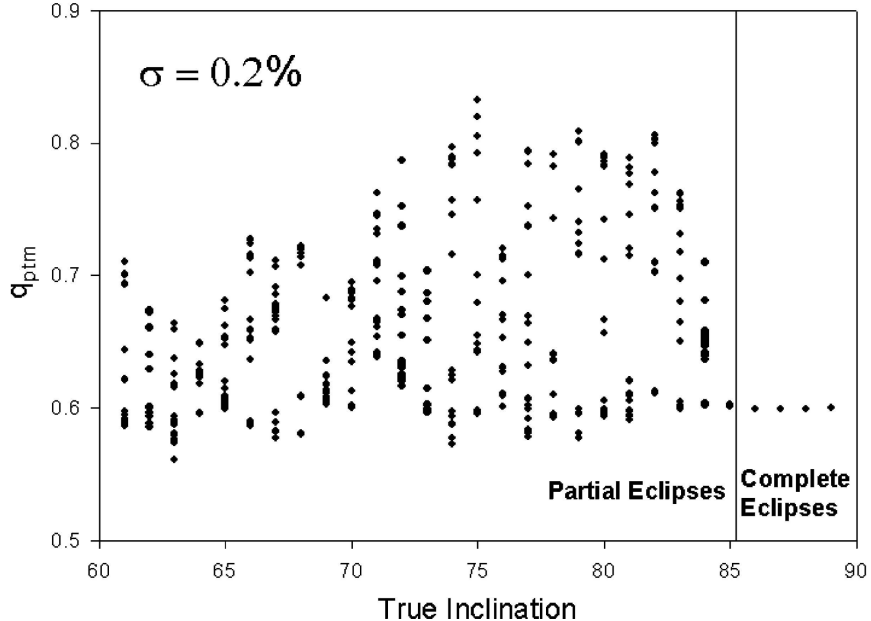


Figure 38: A series of estimates of  $q_{\text{ph}}$  on simulated contact binary light-curves at a variety of inclinations, with photometric uncertainties of 0.2%. This shows that the estimate of  $q_{\text{ph}}$  is only stable when the inclination is high enough such that complete eclipses occur. (Fig. 5 from Terrell and Wilson [2005]).

Motivated by new photometric data collected by all-sky surveys, researchers are still improving this method. In recent work, neural networks have been used to find the parameters  $[f, q, i]$  [Zeraatgari et al., 2015]. In response to the dramatic increase in the volume of data collected, fully automated approaches have been developed to classify light-curves of the various types of eclipsing binary systems [Prsa et al., 2008, 2009].

### 3.7 O-C Analysis

O - C Analysis is one of the oldest analysis techniques for analyzing eclipsing binary stars. Historically, great effort has been spent on compiling “times of periastron”, for the bright eclipsing binary stars. Simply, the time when the eclipsing binary is at its minimum brightness is recorded over and over again, for a large number of orbital periods.

O-C Analysis is short for “observed minus computed”, referring to the fact that a measurement is the observed time of minimum light as compared to the computed time of minimum light. First, a full light-curve is obtained for the system in question. Then, based on this light-curve, the period is calculated, and an ephemeris is computed, listing all of the future times of minimum light. Finally, light-curves are obtained at future epochs. The observed times of minimum light (O) are compared to previous times of minimum light as

computed by the ephemeris ( $C$ ). The difference ( $O - C$ ) is plotted as a function of epoch. On an O-C diagram, a linear change in period (of the form  $P = a \times t + b$ ) appears as a parabola (see Fig. 40).

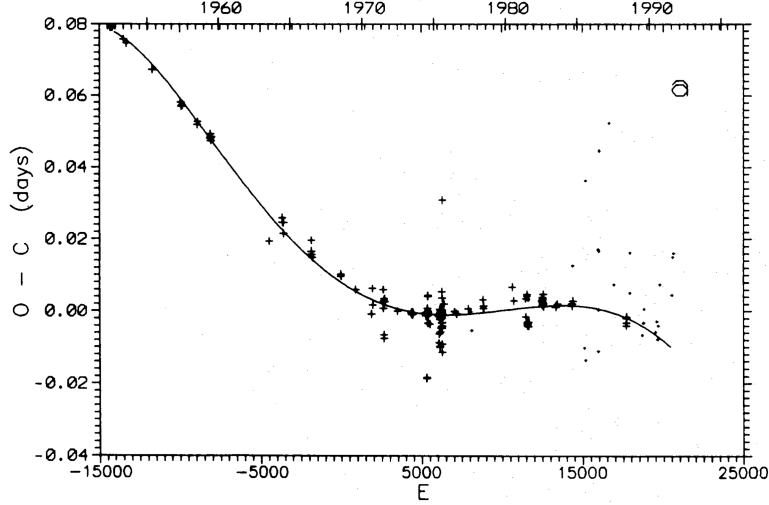


Figure 39: The O - C diagram of V566 Oph, fit by a least squares polynomial. (Fig. 4a from Kalimeris et al. [1994]).

By fitting polynomial models to observed ( $O - C$ ) data, we can calculate the rate of period change  $\frac{dP}{dT}$ , which is represented as  $\dot{P}$ . When the light-curve of a contact binary is well sampled, O-C analysis is stable against the appearance and disappearance of starspots and photometric noise (see Fig. 40) [Kalimeris et al., 2002]. However, when photometric data is sparsely sampled (as in data from some all-sky surveys), the determination of  $\dot{P}$  using the  $O - C$  method is less certain. To adapt the  $O - C$  method to survey data, automated approaches have been developed [Lohr et al., 2015].

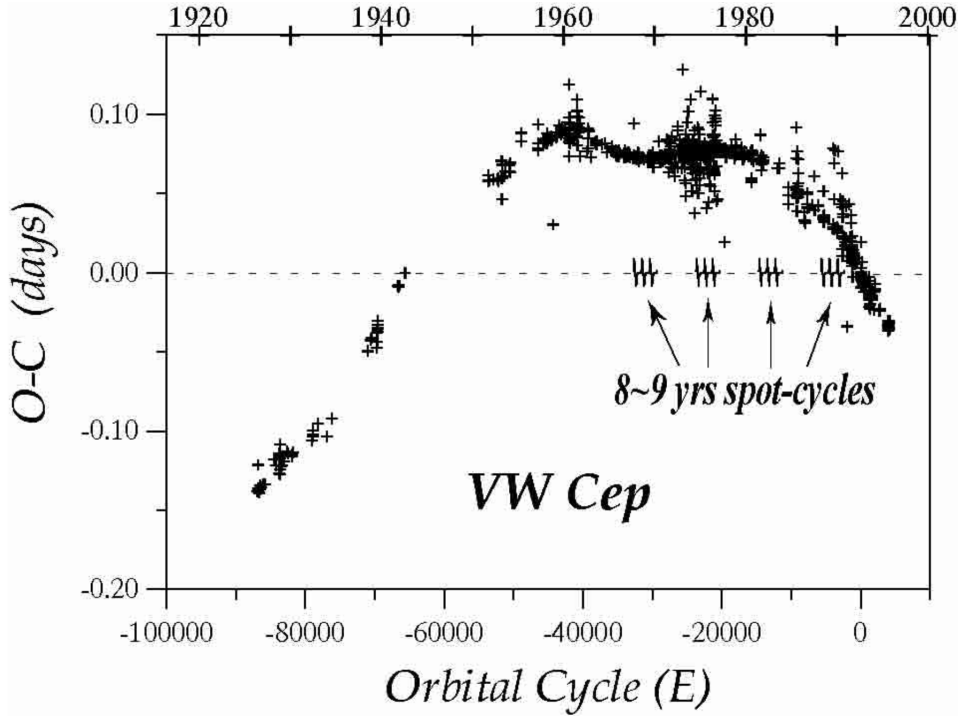


Figure 40: An O-C diagram of the contact binary VW Cep. Note how the presence of starspots (during 8-9 year spot cycles) causes additional scatter in the O-C trace, but does not change the local median trace value. (Fig. 7 from Kalimeris et al. [2002]).

Measurements of  $\dot{P}$  provide an important constraint on models of contact binary evolution (see Fig. 41) [Qian, 2001]. It is measurements of  $\dot{P}$  that allow us to find contact binaries that may be close to merger [Tylenda et al., 2011, Molnar et al., 2017]. The orbital period of a contact binary can change for a variety of reasons, but an observed period change always implies underlying geometrical and structural changes [Kalimeris et al., 1994]. In contact systems, orbital period changes can generally be divided into short-term variations (which happen on decadal 10 year timescales) and long-term variations, (which happen on a thermal timescale, typically millions of years). The long-term variations could be caused by angular momentum loss due to magnetic braking, mass loss through the  $L_2$  point and/or the chemical evolution of the primary. The short-term variations are caused by the orbit of a third body or the redistribution of the angular momentum due to magnetic activity.

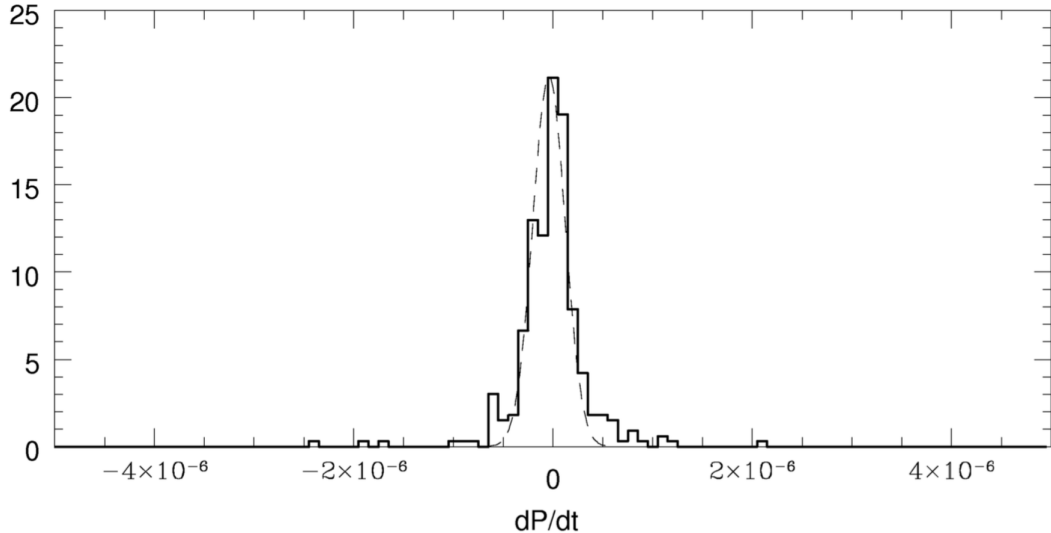


Figure 41: A histogram of the  $\dot{P}$  values measured for 569 contact binaries in the OGLE survey. This distribution is unimodal and symmetric about 0, which is not predicted by the TRO model. (Fig. 3 from Kubiak et al. [2006]).

### 3.8 Working with Survey Data

In recent years, vast quantities of photometric data have been obtained by all-sky surveys. Some examples of all-sky surveys are the All-Sky Automated Survey [ASAS, Pojmanski, 2000], Robotic Optical Transient Search Experiment [ROTSE, Akerlof et al., 2000], Trans-Atlantic Exoplanet Survey [TrES, Devor et al., 2008], Lincoln Near-Earth Asteroid Research program [LINEAR, Palaversa et al., 2013], and Catalina Real-Time Transient Survey [CRTS, Drake et al., 2014b] (see Fig. 42).

There are large quantities of contact binaries in each of these surveys, most of which remain unexamined. The main motivation for studying contact binaries in survey data is the sheer number of systems that can be studied simultaneously. Data from large all-sky surveys are very different in nature compared with data taken on a single night with a single telescope. Working with all-sky surveys presents huge advantages to working with traditional light-curve data, but it also has major drawbacks.



Figure 42: Images of the instruments used in six modern surveys. From the top left, SuperWASP [SuperWASP, Norton et al., 2011], ASAS [ASAS, Pojmanski, 2000], [ROTSE, Akerlof et al., 2000], and from the bottom left SDSS [SDSS York et al., 2000], PTF [PTF Law et al., 2009], and CRTS [CRTS Djorgovski et al., 2011].

In “traditional” variable star observing, an observer slews the telescope to the target at the beginning of the night, and then takes a continuous sequence of images (from which she will make photometric measurements) at regularly spaced time intervals, until the star has rotated one full period, or until morning twilight. The observer can only look at one target at once, but the selected target is observed many times in one night.

In all-sky surveys, the observing mode is different. All throughout the night, the telescope moves to a field, takes a few images, and then rapidly moves on to the next field. A given source might only be observed one or two times in a given night. Some sources may go unobserved for months at a time. The survey operates night after night, and after several years, it has amassed hundreds of observations of any point on the sky.

When we look in a survey database for photometric measurements of a known contact binary we often see data that looks like the data in Figure 43.

## CSS\_J051901.4-152919

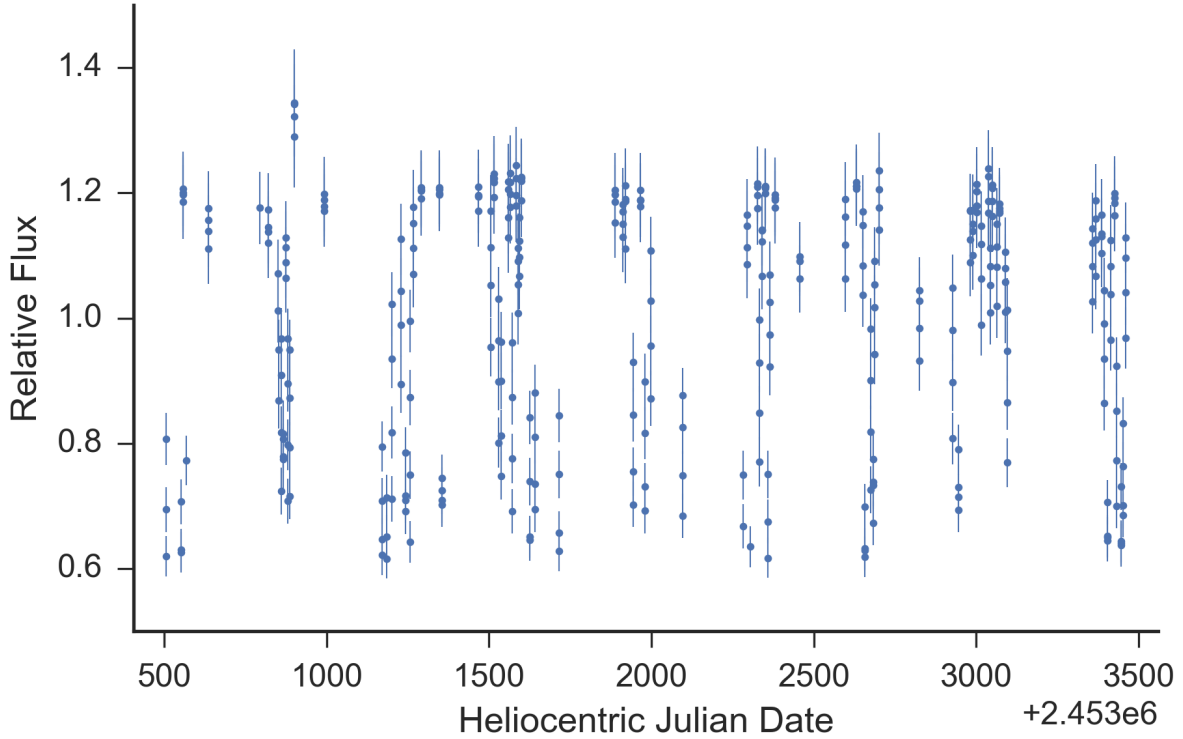


Figure 43: Observations of a contact binary as returned by the CRTS survey. The x-axis is the time of observation (in days), and the y-axis is the relative flux of the observation. Vertical bars about each point denote the uncertainty in the relative flux measurement. Note that the observed flux varies significantly from observation to observation, but we cannot see the periodic nature of the variability with our eyes.

We know that the data in Fig. 43 is not data from a source with constant brightness. The error bar on each point is much smaller than the scatter in the distribution, so we would call this source a significant *variable source*.

Hidden in this data is an underlying periodic function - the light-curve caused by the rotation of the contact binary. This periodic function is hidden in the data, we just need to find it. The data that we have here is a *time-series*: a number of measurements of the flux of a source at many different times. The problem of finding a period in time-series data is usually handled with a *Fourier Transform*.

A Fourier transform decomposes a time dependent signal into a linear combination of sine and cosine terms. The transform returns a power spectral density (or PSD). The frequency at which the light-curve signal has the most power is interpreted as the period.

However, a Fourier Transform cannot be applied to this CRTS data because the obser-

vations are unevenly spaced in time. Instead, we must use the Lomb-Scargle algorithm to return the strongest period in the data Scargle [1982].

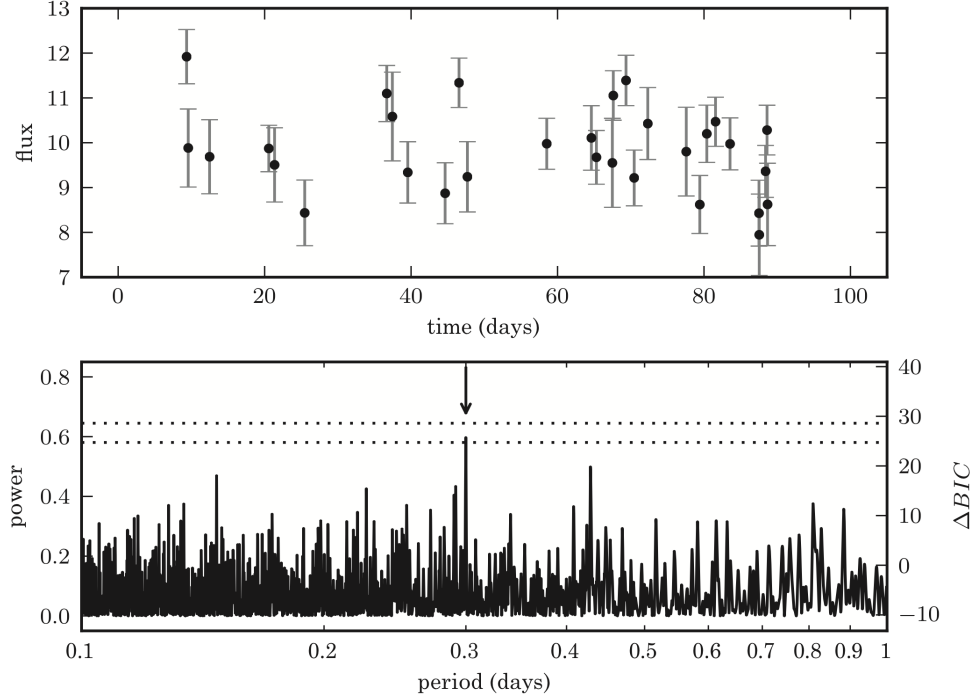


Figure 44: An example of a LS periodogram of unevenly spaced time-series data. The largest peak in the periodogram corresponds to the period that is returned by the algorithm. The arrow marks the location of the true period. (Fig. 10.15 from Ivezić et al. [2014]).

We then calculate the phase of each observation by dividing the time of each observation by the period found in the signal.

$$\theta = \frac{(\text{Time \% Period})}{\text{Period}} \quad (3.6)$$

where (%) is the “modulo” (or remainder operator). We plot the relative flux of each observation of a contact binary as a function of the observation’s phase in Fig. 45.

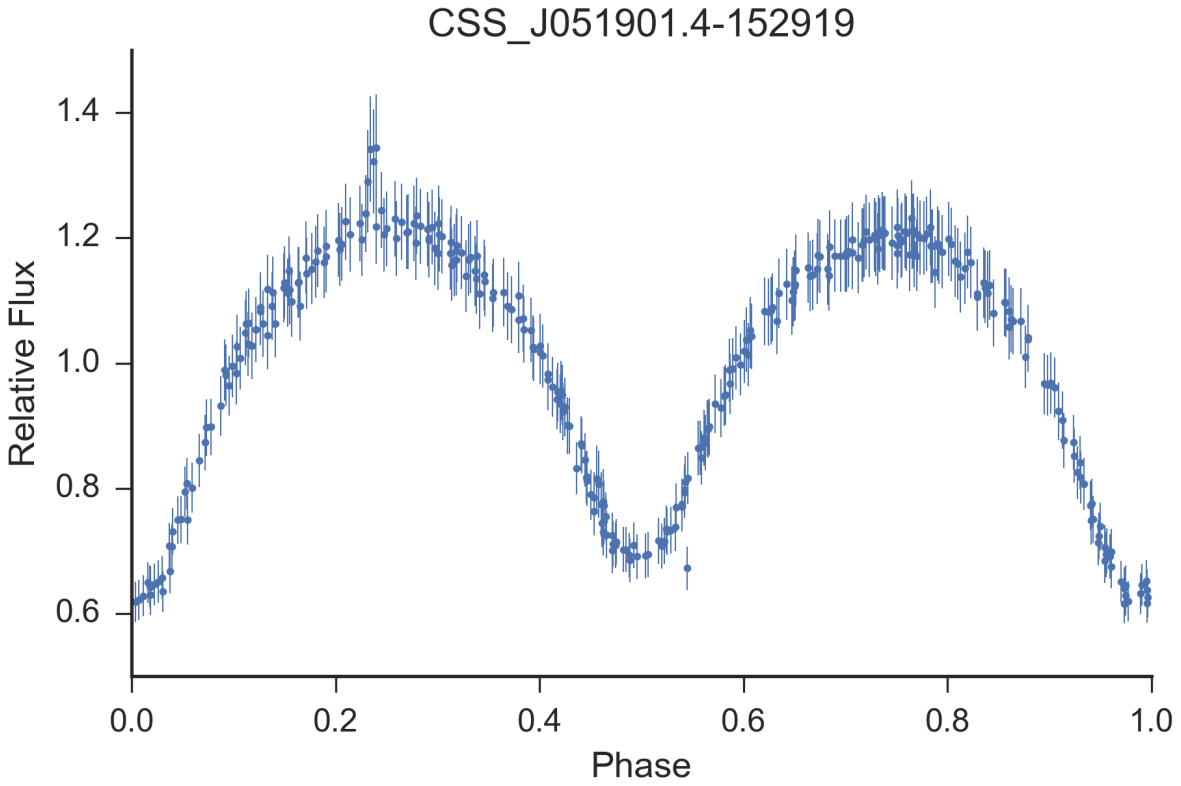


Figure 45: Observations of a contact binary by CRTS, folded by the period as detected by the Lomb-Scargle algorithm. This phase-folded data is similar to what would be produced in a night of single-target observing.

In Figure 45, we see survey data of a contact binary after it has been folded by the orbital period that was returned by the LS algorithm. We see a coherent light-curve with a beautiful shape. A phase-folded light-curve constructed in this way can be analyzed in the same manner as a light-curve taken in a single night of continuous observing.

Once we have phase-folded observations, we can fit these observations with a function in phase. This allows us to describe a light-curve in a way that makes sense, both to humans and computers. Let's consider what our light-curve data actually is: a set of measurements of the flux of a contact binary. These measurements are taken at a certain phase ( $\theta$ ), have a certain value, in our case a measurement of flux ( $F$ ), and this measured value has an associated error ( $e$ ).

Table 3: Format of Phase-folded Data from CRTS

<b>phase (<math>\theta</math>)</b>	<b>flux (<math>F</math>)</b>	<b>error (<math>e</math>)</b>
value	value	value
value	value	value
...	...	...

In the eight years between 2005 and 2013, CRTS observes a given source roughly 350 times. In other words, it reported about 350 phases ( $\theta$ ), 350 fluxes ( $F$ ), and 350 errors ( $e$ ) on those fluxes. So, the raw data comes to us as  $\approx 350 \times 3 = 1050$  individual numbers. These numbers are perfectly valid descriptors of the light-curve, but they are not easily understandable, neither by a human nor a computer.

Thankfully, we can introduce some assumptions that will make the task of succinctly describing our light-curves easier. First, we assume that our light-curve is a *continuous function*. This means that there are no jumps or breaks in the true variation of light. The light-curve has a value at every point in phase and is differentiable at every point in phase. Second, we assume that *the light-curve is periodic*: that the pattern of light variation will exactly repeat itself after some amount of time.

Now, armed with our two new assumptions and light-curve data, we can construct a light-curve function. There are many ways to fit a continuous, periodic function to a set of discrete measurements. The two most popular methods are the polynomial spline fit [Akerlof et al., 1994, Gettel et al., 2006], and the Fourier (or Harmonic) fit [Rucinski, 1997]. There are many other forms that can be used to represent a continuous periodic function - but these are the most obvious choices. Each has its advantages and disadvantages. For example, if the light-curve has large derivatives at some points in the phase (it has “sharp turns”), a polynomial spline fit may be the best choice. For a review of the types of fitting functions, see Andronov [2012].

We have elected to use the harmonic fit, because contact binary light-curves do not typically contain sharp turns [Rucinski, 1993b]. It is easy to implement and can fit the data accurately, provided that there are no sharp turns in the light-curve. By choosing a fitting function, we have turned our raw data from CRTS into a continuous, periodic function, which takes phase ( $\theta$ ) as an input, and returns flux and an associate error:  $F, e = F(\theta)$ . We can use this function to measure geometrical features of the light-curves, as well as check the light-curves for changes over time (Fig. 46).

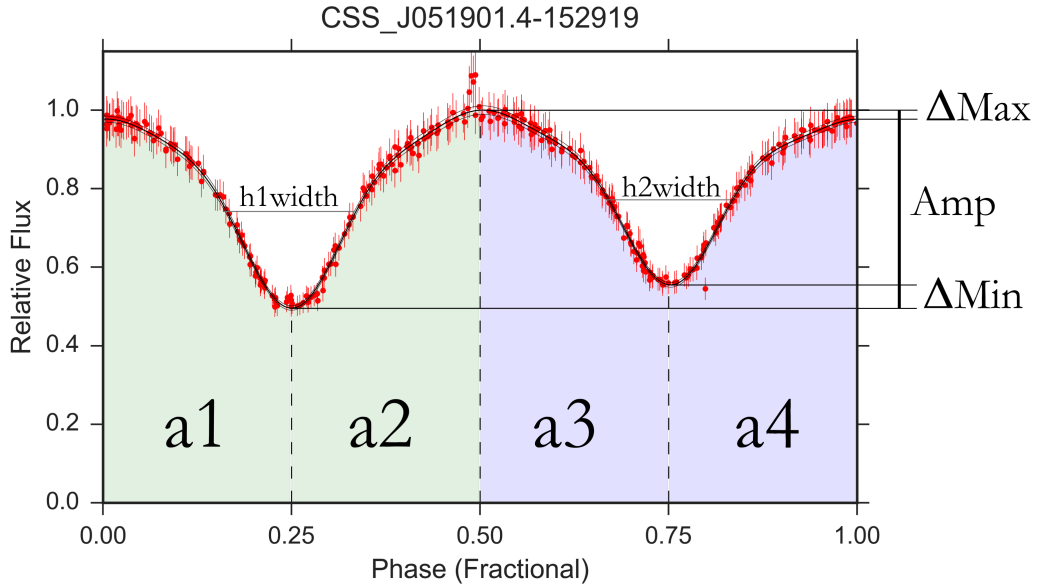


Figure 46: Performing a harmonic fit on light-curve observations allows the light-curve to be measured. The harmonic fit is represented by the black line running through the observations. We have defined various geometrical features (Amp, h1width, a1, etc...) to measure the geometry of this light-curve.

## 4 Motivation

In this section we will motivate this original work on contact binaries using survey data. Since the early 1960's observers have separated contact binaries into two types: A-type and W-type. The Roche geometry of the contact binary systems dictates that the primary (more massive) component of the contact binary has a slightly larger mean gravity. If contact systems obey a normal gravity-brightening law of the form  $T_{\text{eff}} \propto g^{\beta}$ , this would mean that the primary component should have a higher photospheric temperature [Rucinski, 1993a]. The eclipse of the primary component by the cooler, dimmer, secondary should be the deepest eclipse. Contact binaries that conform to this model are called "A-type" systems by observers.

However, binaries are frequently observed that do not fit this model. In "W-type" systems, the eclipse of the primary is the *shallowest* of the two eclipses. "W-type" systems are all of late spectral type (F,G,K,M). There have been many models proposed to explain the "W-type syndrome", which include the system having a hotter secondary component, the presence of large starspots, dark belts in equatorial regions and bright faculae [Rucinski, 1985]. An important feature of contact binary spots is that they are transient - they appear and disappear over a timespan of several years. Some systems have been observed to change from A to W type, leading researchers to believe that, for some systems, the "W-type syndrome" is caused by the presence of large starspots.

There is evidence for magnetic activity cycles with periods ranging from 8 to 11 years on contact binary systems of the solar type [Borkovits et al., 2005, Marsh et al., 2016]. During these activity cycles, the mean starspot coverage of the photosphere increases and decreases. The best model for contact binary light-curve changes is the appearance and disappearance of starspots on the photosphere [Bradstreet and Guinan, 1988]. Dramatic changes in contact binary light-curves have been observed [Rucinski and Paczynski, 2002, Lee et al., 2004]. Data from Doppler imaging of bright contact binaries provides detailed maps of spot coverage (see Fig. 47). However we can only produce these maps for the brightest of contact binary systems. This makes it difficult to understand how the process of starspot evolution changes as a function of system mass or temperature.

The spot model can be tested by repeatedly measuring the luminosity of a given contact binary, checking for the variability associated with the appearance and disappearance of spots. The area of the contact binary that is presented to the observer changes as a function of orbital phase. By monitoring light-curves for changes at certain phases, we can determine where spots are forming on the binaries. If the starspot coverage changes on one component, but does not change on the other, then the light-curve will change shape (see Fig. 48).

By measuring the light-curve shapes of thousands of contact of systems over several years,

we can answer the following questions:

1. Is there more starspot formation on one component, or is the process uniform across the shared photosphere?
2. Do the answers to questions 1 & 2 depend on the temperature of the system?

Relationships between the starspot behavior of the two components provide evidence that the magnetic dynamo in the convective envelope of each component is similar. The magnetic dynamo responsible for starspots in contact binary stars has not yet been studied.

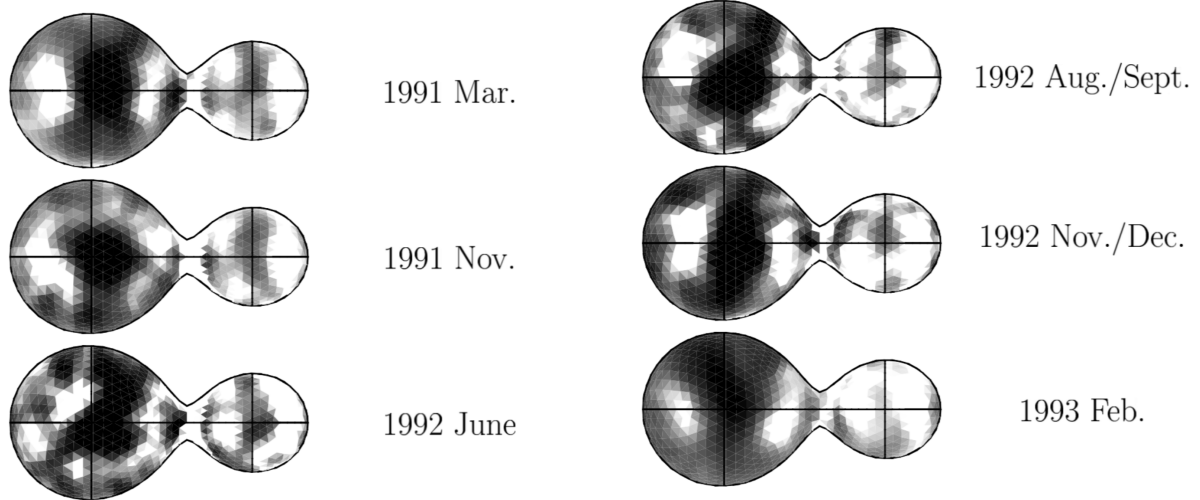


Figure 47: Time-series maps of the starspot coverage on the contact binary VW Cephei, as reconstructed from Doppler imaging. We do not have many time-series maps of starspots like this one, making it difficult to understand how starspot evolution changes as a function of mass, temperature, or other characteristics. (Fig. 12 from Hendry and Mochnacki [2000]).

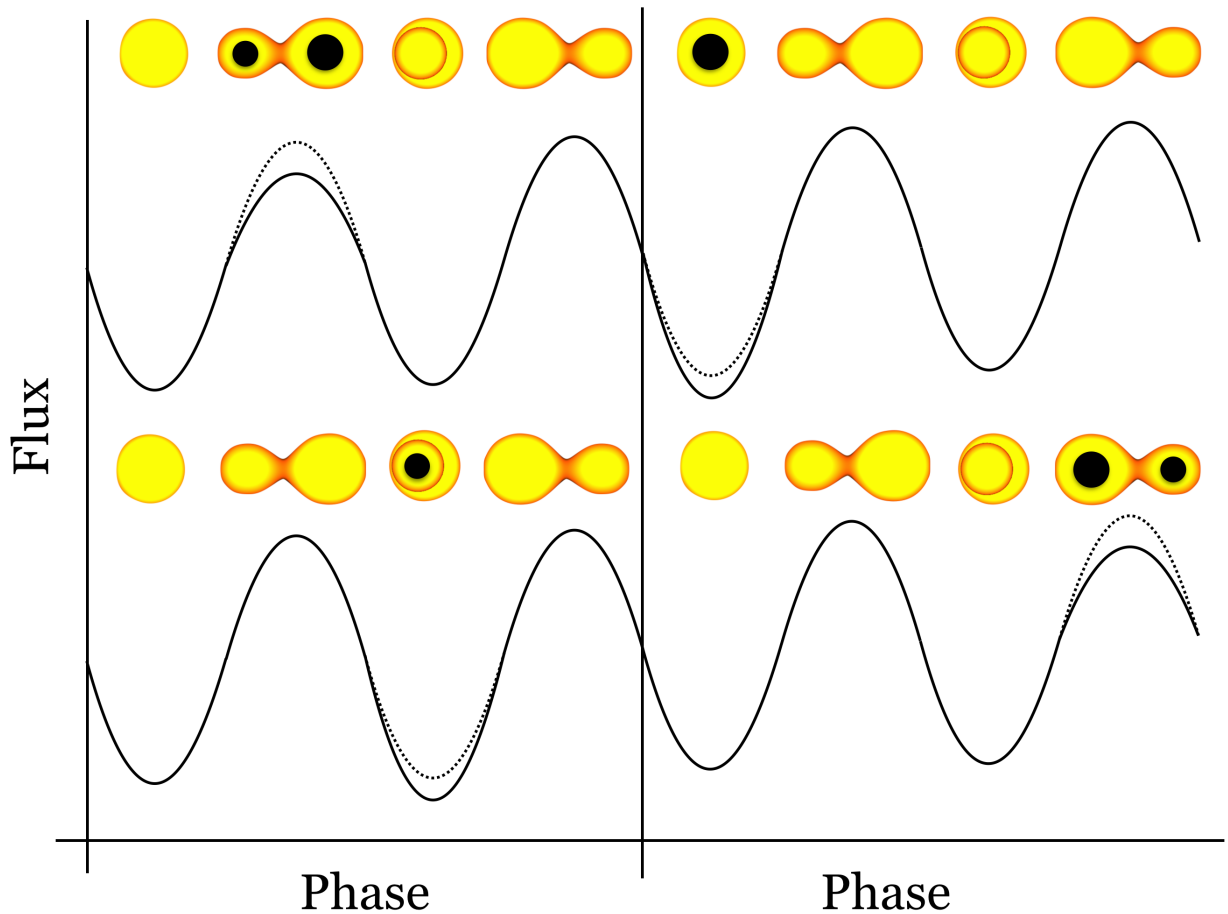


Figure 48: A schematic diagram of light-curve changes that occur when starspots appear on the photosphere of a contact binary, for four different starspot locations. The dotted line is the shape of the light-curve without the presence of the marked starspots, whereas the solid line is the shape of the light-curve with the marked starspots.

## 5 Methods

In §5.1, we describe the data that we will use in this study. We will calculate the photospheric temperature of each binary by using SDSS *ugriz* photometry (§5.2). Then, we will perform a 4, 5, or 6 term harmonic fit on the phase folded light-curve and convert the light-curve into units of flux (§5.3). We will divide the flux curve into four distinct regions based on eclipse full-width at half-minimum (§5.3.1), and perform a linear fit on the harmonic fit residuals as a function of time in each light-curve region (§5.5). We will then construct a uniformity metric (named Region Disagreement) for the set of four brightness trends measured for each binary (§5.6). We will compare this optical variability to UV data by computing the  $FUV - NUV$  color and  $FUV - NUV$  excess of each binary, as compared to a main-sequence star of similar temperature. After each one of the previous steps, we will remove systems with low-quality data from our sample, to ensure that the final sample is clean.

### 5.1 Sample Description

In our study, we use data from two separate surveys: (1) We use CRTS data spanning eight years, which allows for the variation in the luminosity of each system on a decadal timescale to be measured, and (2) we use SDSS data which provides multiband photometric measurements taken within the timespan of a few minutes, allowing the temperature of each binary to be measured.

The Catalina Sky Survey (CSS) uses three (1-meter) telescopes to survey the sky between declinations of -75 and +65 degrees. Although the CSS was originally designed for the detection of Near Earth Asteroids, the CRTS project aggregates time-series photometry for over 500 million stationary “background” sources [Drake et al., 2009, Mahabal et al., 2011, Djorgovski et al., 2011]. CRTS observations are taken in “white light”, i.e. without filters, to maximize survey depth. CRTS can perform photometric measurements on sources with visual magnitudes in the range of  $\sim 13$  to 20. Though we only used eight years of data, CRTS continues collecting data to this day. The CRTS photometry used in this work is publicly accessible through the Catalina Surveys Data Release 2 at [crtsn2.calspace.caltech.edu](http://crtsn2.calspace.caltech.edu).

The number of observations that CSS has collected for the candidate systems that we study ranges from 90 (for the least observed systems) to 540 (for the most observed systems). The median number of CSS observations per candidate system is 336, with a standard deviation of 86 observations. The mean photometric error varies from 0.05 magnitudes to 0.10 magnitudes for most systems, increasing as a function of CRTS magnitude.

The Sloan Digital Sky Survey provides multiband photometry in the  $u, g, r, i$ , and  $z$  bands. Because of its drift-scanning configuration, SDSS is well suited to performing photometry on short-period variable stars ( $P < 1$  day), because all of the bands are exposed within a

short time of each other: there is a delay of roughly 5 minutes between the exposure of the  $g$  and  $r$  images [York et al., 2000]. We use the SDSS DR10 ( $g - r$ ) color to calculate the temperature of the binary systems in this study [Ahn et al., 2014].

The initial set of contact binaries from which we derived our sample was selected as described in Drake et al. [2014b]. The CRTS photometry for this sample can be accessed publicly at <http://nesssi.cacr.caltech.edu/DataRelease/Varcat.html>.

The Drake et al. [2014b] sample was created by selecting data from the Catalina Surveys Data Release 1 (CSDR1), based on the criteria of high Stetson variability index ( $J_{WS}$ ) and large standard deviation of brightness measurements ( $\sigma$ ). Drake performed Lomb-Scargle periodogram analysis [LS, Scargle, 1982] on these variables, testing for significant periods. Candidates that passed a LS significance cutoff along with additional data quality cuts were further processed to determine the best period and were then visually inspected. Approximately half of the inspected candidates passed selection and were classified by type (e.g. EW: contact binary, EA: Algol type, RRab: RR Lyrae, etc.) based on period, light-curve morphology, and color information.

In the Drake et al. [2014b] sample there are 30,743 binaries classified as EW, corresponding to W UMa (contact) binaries. The SDSS photometry was crossmatched to the CRTS photometry by using the Large Survey Database framework [LSD, Juric, 2012]. We searched for SDSS point sources within 3 arcseconds of the coordinates of the CRTS candidates, and when a one-to-one match existed, we correlated the photometry and added the candidate to our sample. When a unique match did not exist between the SDSS and CRTS photometry, we did not add the candidate to our sample. We chose the 3" search radius because CSS pixels subtend 2.5". Out of the 30,743 sources queried, there were 13,551 sources with matching CRTS and SDSS photometry.

Drake et al. [2014b] have shown that 98.3% of the sources classified as contact binaries in CRTS data are also classified as contact binaries in the analysis of LINEAR data in Palaversa et al. [2013]. They have also shown that many of the candidates have SDSS DR10 spectra consistent with known spectral characteristics of contact binaries. Because our contact binary sample is selected from the Drake subset, we expect that it will also have greater than 98% purity.

Our initial sample of contact binaries contains systems for which we have both time-series photometry (provided by CRTS), and a temperature measurement using ( $g - r$ ) color (provided by SDSS). From the 30,743 EW variables (corresponding to contact binaries), we find that 13,390 contain matching SDSS photometry. We elect to further filter these 13,390 systems, including only systems with orbital periods of less than two days ( $P < 2.0d$ ), because orbital periods of longer than two days are not observed for true contact systems. This filter eliminates 161 systems to leave 13,229. We also elect to filter out systems with

a reported mean  $V_{CSS} < 13.5$ , because Marsh et al. [2016] found that inconsistencies in the photometric aperture size chosen for bright sources renders the photometry of these bright sources unreliable. This filter eliminates 948 systems to leave 12,281 in the sample.

## 5.2 Measuring Photospheric Temperature with SDSS

In this section, we describe how we use SDSS  $g$ ,  $r$ , and  $i$  band photometry to estimate the photospheric temperature of each contact binary.

1. We define color cutoffs that eliminate systems with saturated SDSS  $g$  and  $r$  band photometry. A sizable fraction of the SDSS  $g$  band photometry is saturated for  $g < 15$ . To remove the saturated photometry, we define color limits based on the observed distribution of contact binary colors and remove systems outside of those limits (see Fig. 49).

$$\begin{aligned} (g - r) &> 0.02 * g - 0.4 \text{ (Red Limit)} \\ (g - r) &< 0.13 * g - 0.9 \text{ (Blue Limit)} \end{aligned} \quad (5.1)$$

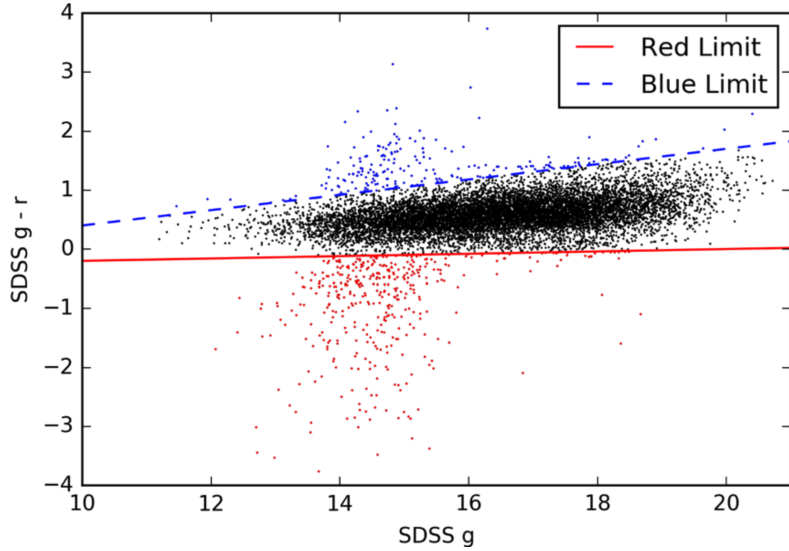


Figure 49: The distribution of the sample in SDSS  $(g-r)$  versus  $g$  color space, dashed lines show the red and blue limits imposed upon the data. These limits were imposed to eliminate systems with evidence of saturated SDSS photometry. (Fig. 4 from Marsh et al. [2016]).

Even though the vast majority of the systems lie far from the galactic plane ( $l > 15^\circ$ ), the contact binaries in the sample are distant because this sample is fainter than the samples of most previous surveys. For this reason, we measure the photospheric temperature of each binary by using extinction corrected SDSS  $(g - r)$  photometry.

2. We begin the extinction correction process by computing the Johnson  $V$  magnitude. Johnson  $V$  can be computed using the maximum  $V_{CSS}$  magnitude, and the uncorrected SDSS  $r$  and  $i$  measurements, by using calibrations from Jester et al. [2005] and Hovatta et al. [2014].

$$(V - R) = 0.96 * (r - i) + 0.21 \quad (5.2)$$

$$V = V_{CSS} + 0.91 \times (V - R)^2 + 0.04 \quad (5.3)$$

3. We compute the distance modulus to each binary by using the period-luminosity correlation calibrated by Rucinski [2006]. This luminosity calibration carries a  $1\sigma$  uncertainty of 20%.

$$M_V = -1.5 - 12\log P \quad (5.4)$$

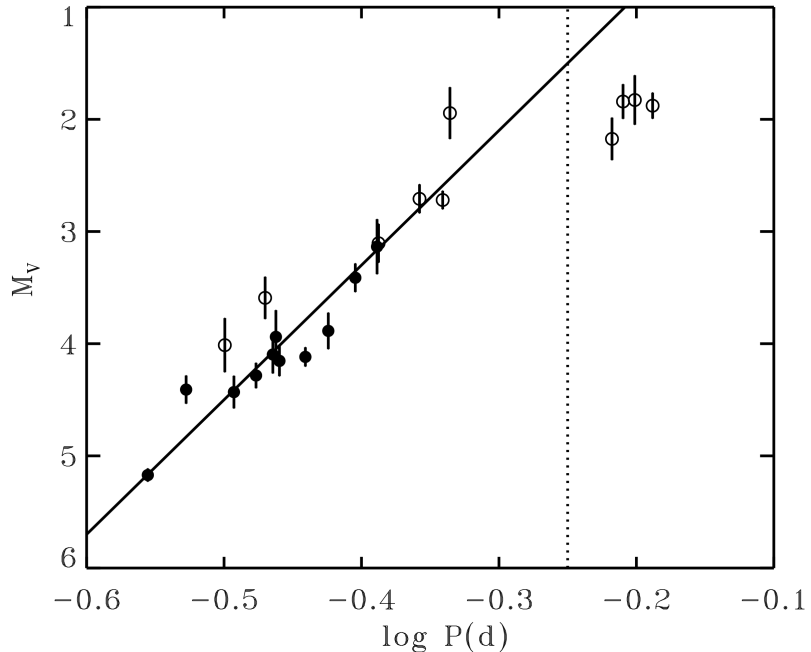


Figure 50: The contact binary period-luminosity relation as calibrated by Rucinski [2006]. Contact binaries with longer orbital periods have a higher luminosity. (Fig. 2 from Rucinski [2006]).

4. We use the Green et al. [2015] three-dimensional dust map (derived from Pan-STARRS1 data) to find a distance and extinction combination such that the sum of the dimming due to distance and  $V$  dimming due to extinction equals the difference between the system's absolute magnitude  $M_V$  and computed  $V$  magnitude.

$$A_V = 3.1 * E(B - V) \quad (5.5)$$

5. We take the  $E(B - V)$  estimated in step 4, and convert it to extinctions in the SDSS  $g$  and  $r$  bands using the calibrations in Schlafly and Finkbeiner [2011].

$$A_g = 3.303 \times E(B - V) \quad A_r = 2.285 \times E(B - V) \quad (5.6)$$

After these extinction corrections are applied, we then use the empirical calibration of SDSS  $g - r$  color to temperature from Fukugita et al. [2011]:

$$T_{\text{eff}}/10^4 K = \frac{1.09}{(g - r) + 1.47} \quad (5.7)$$

This calibration is valid for main-sequence stars with temperatures between 3850K and 8000K. This produces temperature results that have a median error of  $\pm 310$ K.

### 5.2.1 SDSS Photometry Data Cuts

Of the 12,281 systems, 11,782 remained after the cuts effected by applying Eqn. 5.1. We restrict the  $3850K < T_{\text{eff}} < 8000K$ . This filter restricts the binaries to the empirically verified range of Eqn. 5.7. Of 11,782 systems, 11,681 remain after this filter. We then eliminate systems with  $\delta T_{\text{eff}} \geq 500$ K. Of the 11,681 remaining systems, 11,138 remain after this filter.

## 5.3 Light-Curve Harmonic Fitting

We perform a harmonic fit on each set of relative flux measurements (see §3.8), by using the `gatspy` package [Vanderplas, 2015]. We start with six sine terms, and six cosine terms. We then count the number of local maxima and local minima on the fit. In a physical light-curve, we expect to see two local maxima, and two local minima. This has been known since the first viable physical model was used to compute light-curves [Lucy, 1968a].

If the harmonic fit does not have precisely two local maxima and two local minima, we try the fit again, this time with five sine and five cosine terms. If the fit fails yet again, we try with four sine and four cosine terms, and so on. Of the 11,138 light-curves where a fit was attempted, 8,994 were fit by six terms, 901 by five, 523 by four, 635 by three and 87 by two terms.

CRTS photometry is reported in units of Catalina Sky Survey Magnitude ( $V_{CSS}$ ). For each contact binary system, we convert these magnitudes measurements into flux measurements, relative to the mean magnitude of all observations of the system.

$$\text{Relative Flux} = \frac{10^{-\frac{V_{CSS}}{2.5}}}{10^{-\frac{\text{mean}(V_{CSS})}{2.5}}} \quad (5.8)$$

We then shift the contact binary light-curve in phase such that the deepest minimum of the flux (Min1) is located at  $\theta = 0.25$ .

### 5.3.1 Light-Curve Harmonic Fit Filters

Harmonic fits with at least four Fourier terms have been shown to approximate well the true shape of the contact binary light-curve [Rucinski, 1973, 1993b]. However, it is not traditional in previous literature to approximate the shape of the contact binary light-curve with fewer than four Fourier terms.

If a harmonic fit was reduced to three or fewer Fourier terms, the fit and corresponding system were discarded from the sample. From the 11,138 binaries remaining after the filters described in §5.2.1, this filter removed 720 binaries to leave 10,418.

Just because the harmonic fit has two local minima and two local maxima does not mean that it is a good approximation of the data. To separate light-curves that fit the observed data well from erroneous fits, we define a goodness-of-fit criterion:

$$\text{GOF} = \text{standard deviation} \left( \frac{\text{Fit Residual}}{\text{Fit Residual Error}} \right) \quad (5.9)$$

Assuming gaussian residuals, observed data that is completely described by the harmonic fit has  $\text{GOF} = 1$ . We choose to exclude light-curves with  $\text{GOF} < 1.5$  from our study. Increasing the tolerance to  $\text{GOF} < 1.5$  allows for systems with significant variation in their light-curve during the observation timespan to pass through the filter. It does not allow, however for the passage of fits with a large number of distant outlying observations.

After we perform a successful harmonic fit on the phase-folded photometry, we scale the flux measurements such that the maximum value of the harmonic fit has a flux measurement of 1:

$$\text{Normalized Relative Flux} = \frac{\text{Relative Flux}}{\text{Max(Relative Flux)}} \quad (5.10)$$

A light-curve prepared in this way is shown in Fig. 51 as the black line in the top panel.

## 5.4 Division of the Light-Curve

In order to determine if the behavior of the light-curve variation is dependent on orbital phase, we divide the light-curve into four bins in orbital phase. We will check each light-curve for variation in these four regions separately. The boundaries between the light-curve

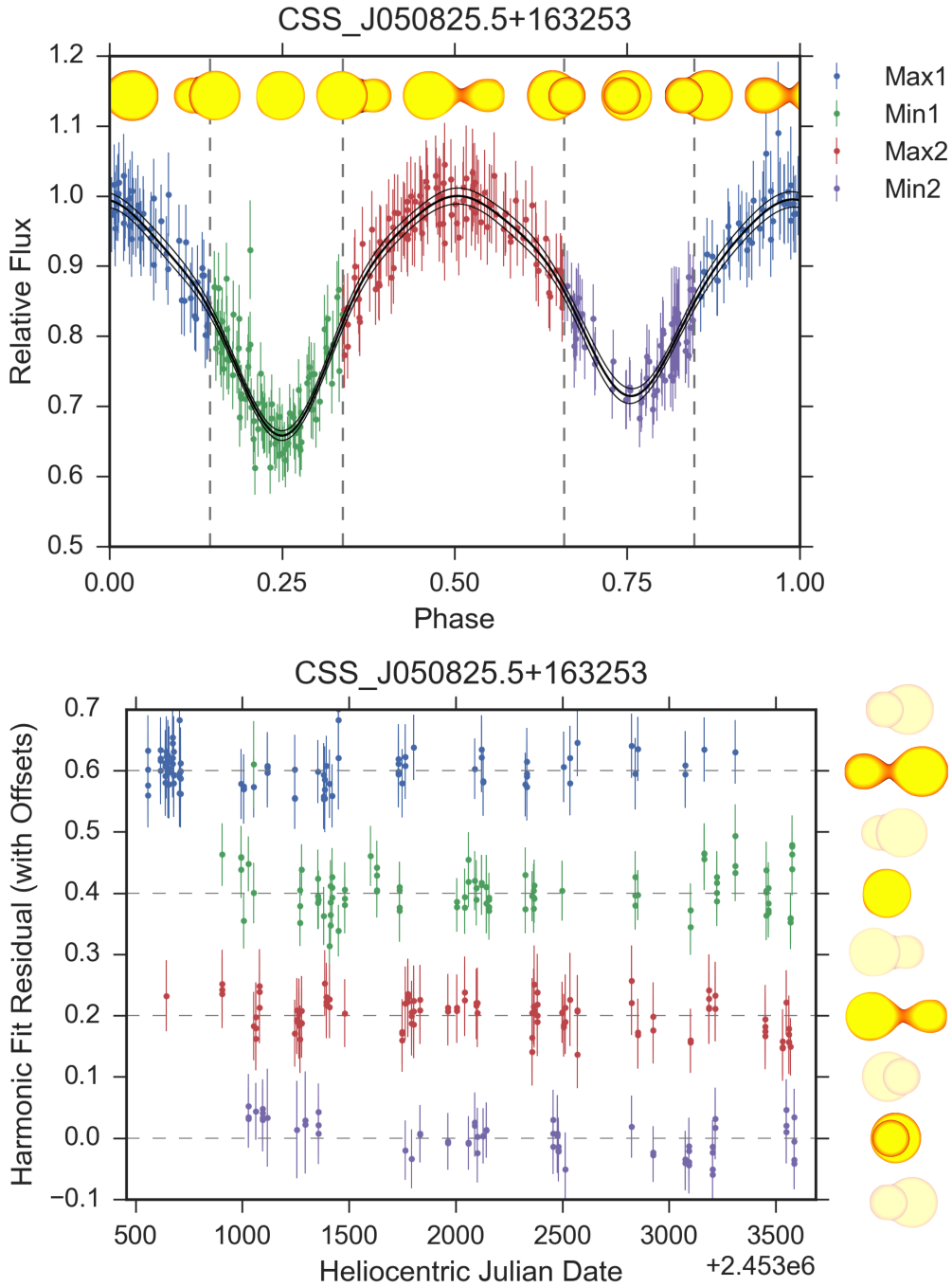


Figure 51: The phased-shifted light-curve of a contact binary as observed by CRTS. In the top panel, we see that the light-curve is normalized in flux such that the maximum value of the harmonic fit (in black) is 1.0. We see that the light-curve has been divided into four distinct regions by phase. In the bottom panel, we see the harmonic fit residuals as a function of observation time. Observations from each one of the four bins have been separated. The light-curve of this contact binary does not change over the eight-year observation timespan, the residuals are centered around 0 for observations in each phase bin. The orbital period of this binary is 0.323716 days. The variability amplitude of this object binary is 0.57 magnitudes.

regions are defined to be the eclipse full-width at half-minima (FWHM). This width is calculated independently for each of the two eclipses. The light-curve region boundaries are not required to be symmetrical about the phases 0.25 and 0.75 (Fig. 51). The half max fluxes are calculated, and then the phase coordinates of the light-curve intersections with that value are recorded. We elect to use four regions because the regions correspond to distinct orientations of the contact binary with respect to the line of sight (see the bottom panel of Fig. 51). The most important feature of this division is that for most contact binaries, it divides the phase into four bins of approximately equal phase-width. The regions of phase that include the eclipse minima (the regions including phase 0.25 and phase 0.75 in Fig. 51) are slightly smaller in phase. We describe each light-curve region:

Min1 At the first minimum, the hotter, brighter component is partially (or completely) blocked by the cooler, dimmer component.

Max1 At the first maximum, the longest axis of the binary is perpendicular to the line of sight. One half of the hotter component and one half of the cooler component are facing the observer.

Min2 At the second minimum, the cooler, dimmer component is partially (or completely) blocked the the hotter, brighter component.

Max2 At the second maximum, the longest axis of the binary is perpendicular to the line of sight. One half of the hotter component and one half of the cooler component are facing the observer, but these are the opposite halves that are visible during Max1.

Given the precision and amount of the CRTS data, we find that these four bins are the most appropriate choice for dividing the light-curve. We could divide the light-curve into more than four bins. However, as the bin size decreases, so will the number of observations in each bin. In order to ascertain trends in the harmonic fit residuals, there must be a large number of observations in each individual bin. Additionally, the choice of these four bins is understandable from a physical standpoint, and the bins are of approximately equal width in phase, so they have an approximately equal number of observations, yielding an approximately equal uncertainty in the trend.

#### 5.4.1 Light-Curve Division Data Quality Cuts

In order to ensure a uniform analysis, we must place constraints on light-curves. We must ensure that there are enough photometric measurements in each bin to describe a brightness trend. We impose the following data quality cuts:

Filter 1. We require that the smallest light-curve region be greater than 0.1 phases wide. We know from physical models that contact binaries are not expected to have eclipse FWHM smaller than 0.1 phases (see the synthesized light-curves in Rucinski [1993b]). From the 10,418 binaries, this filter removes 94, to reduce the sample to 10,324.

Filter 2. We require that all systems have at least 20 observations in each phase bin. This is to ensure that  $\dot{F}$  can be determined robustly by fitting a line to the data. From the 10,324 remaining after Filter 1, this filter removes 445, leaving 9,879. Fig. 52 contains a visual depiction of Filter 2.

Filter 3. We require that the time difference between the first observation and the last observation is at least 2000 days (5.5 years) in each bin. This is to ensure that the observed  $\dot{F}$  is representative of the behavior over the majority of the eight year observation time baseline, and is not an extrapolation of the flux trend in a very small time window. From the 9,879 binaries remaining after Filter 2, this filter removes 228, leaving 9,651. Fig. 53 contains a visual depiction of Filter 3.

If any one of the light-curve regions fails any one of these tests, the binary must be removed from the sample, to ensure for uniform analysis. These filters remove 767 of the 10,418 systems remaining after the cuts in §5.3 to leave 9,651.

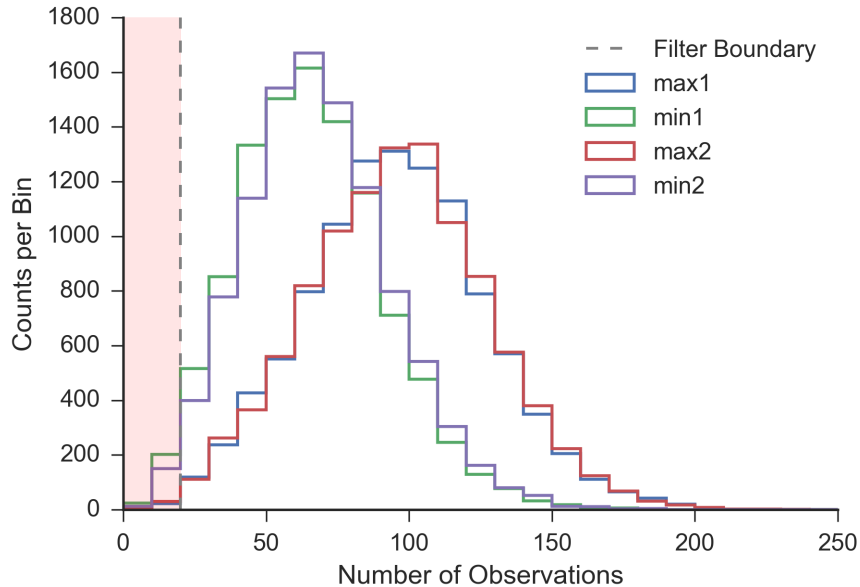


Figure 52: A histogram of the number of observations in each light-curve region. We can see that the maxima regions (Max1, Max2) have a higher median number of observations ( $\approx 100$ ) than the minima regions (Min1, Min2) ( $\approx 60$ ). This is because maxima regions are wider in phase than the minima regions. The filter is shown by the shaded area.

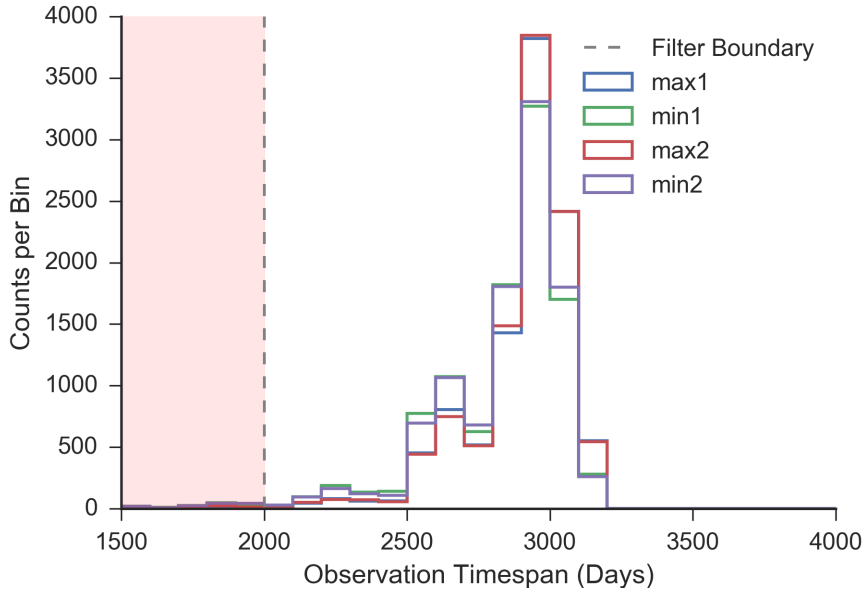


Figure 53: A histogram of the time difference (in days) between the first and last observation of a given light-curve region (Max1, Min1, Max2, Min2). We can see that the distribution of observation timespans is similar across the four light-curve regions. In red, the filter is shown.

## 5.5 Regression of the Residuals

We measure the deviations of the observations with respect to the harmonic fit performed on all CRTS observations in order to detect brightness changes associated with starspot formation. We can consider the harmonic the “average” light-curve of the contact binary during the eight-year CRTS observation timespan. This is because the CRTS measurements are randomly, (but relatively uniformly) sampled in time, and the harmonic fit does not preferentially weight observations by their time of observation.

We subtract the harmonic fit from each observation, propagating the errors by adding in quadrature:

$$\begin{aligned} \text{Residual} &= \text{Observed Flux} - \text{Harmonic Fit} \\ \text{Residual Error} &= \sqrt{\text{Observed Flux Error}^2 + \text{Harmonic Fit Error}^2} \end{aligned} \tag{5.11}$$

The number of measurements used to form the harmonic fit varies from binary to binary, with a median of 348. Because  $348 \gg 1$ , we assume that an individual measurement has

so little influence on the harmonic fit such that the errors are uncorrelated, and we can add the errors in quadrature.

We then perform a linear regression on the fit residuals as a function of observation time (see the bottom panel of Fig. 51). For each light-curve region in every binary, we perform a linear fit of 500 Monte Carlo simulated datasets. The standard deviation of the distribution of the 500 measured slopes is taken to be the  $1\sigma$  uncertainty in  $\dot{F}$  for that light-curve region.

In this work we define  $\dot{F}$  to be the rate of change in flux received in units of the contact binary's maximum flux per year. To aid intuition, we report  $\dot{F}$  as a *percentage* of the contact binary's maximum flux. A  $\dot{F} = 1$  measurement for a particular light-curve region indicates that the region is brightening at a rate of 1% of the contact binary's maximum flux per year.

### 5.5.1 Regression of the Residuals Data Quality Cuts

We require that the maximum  $1\sigma$  error in the  $\dot{F}$  measurement is less than 0.5. This means that  $\dot{F}$  must be known with an uncertainty of less than 0.5% of the maximum flux per year. Of the 9,651 remaining after the cuts described in 5.4.1, this filter removes 1,262, leaving 8,389. This filter is represented visually in Fig. 54.

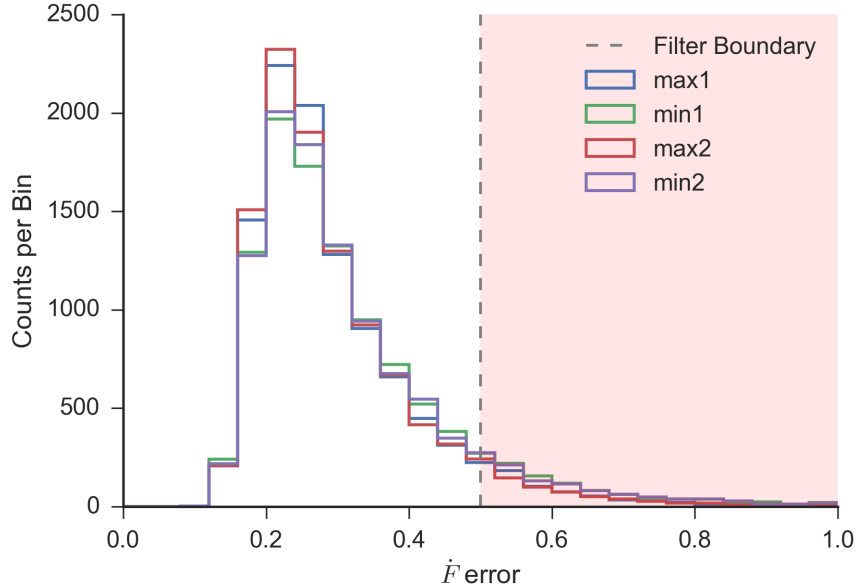


Figure 54: A histogram of the  $\delta \dot{F}$  distribution of a given light-curve region (Max1, Min1, Max2, Min2). We have elected to remove systems with uncertainty in  $\dot{F}$  of greater than 0.5 from the sample.

Again, if any one of the light-curve regions fail this test, the binary must be removed

from the sample. Table 4 summarizes the filters that we have applied to the dataset.

Filter Name	Input	Removed	Removed (%)	Output	Section
SDSS Match (3")	30,743	17,353	56.4%	13,390	5.1
Period < 2.0 d	13,390	161	1.2%	13,229	5.1
Mean $V_{CSS} > 13.5$	13,229	948	7.1%	12,281	5.1
SDSS Photometry	12,281	1,143	9.3%	11,138	5.2.1
Harmonic Fit Filters	11,138	720	6.4%	10,418	5.3.1
Light-Curve Division	10,418	767	7.3%	9,651	5.4.1
Residual Regression	9,651	1,262	13.1%	8,389	5.5.1

Table 4: A summary of the filters applied to the initial sample of 30,743 EW variables. The number of systems input into the filter, the number of systems removed by the filter, and the percentage of the input systems removed by the filter are reported.

## 5.6 Computation of a Uniformity Metric

We would like to establish a metric that determines to what extent the measurements of brightness change ( $\dot{F}$ ) in each of the four regions agree. We take the four measurements of  $\dot{F}(\text{Max1})$ ,  $\dot{F}(\text{Min1})$ ,  $\dot{F}(\text{Max2})$ ,  $\dot{F}(\text{Min2})$  and compute the weighted mean of their values. The weights in this case are the reciprocal of the measurement uncertainties,  $\frac{1}{\delta\dot{F}(\text{Reg.})}$ .

$$\mu = \sum_{\text{Region}=1}^4 \frac{\dot{F}(\text{Region})}{\delta\dot{F}(\text{Region})} \quad (5.12)$$

The weighted mean  $\mu$  is similar to the  $\dot{F}$  that would be measured had observations from all four light-curve regions been fit simultaneously. We use  $\mu$  to compute a uniformity metric which we will name the Region Disagreement, or RD for short. This metric allows for the comparison of the level of disagreement between the four slopes supported by the data. The larger the value of RD metric, the more evidence exists for disparity between the four slopes measured for each light-curve. A light-curve where all four slopes were identical would have a uniformity metric of zero (see Fig. 55).

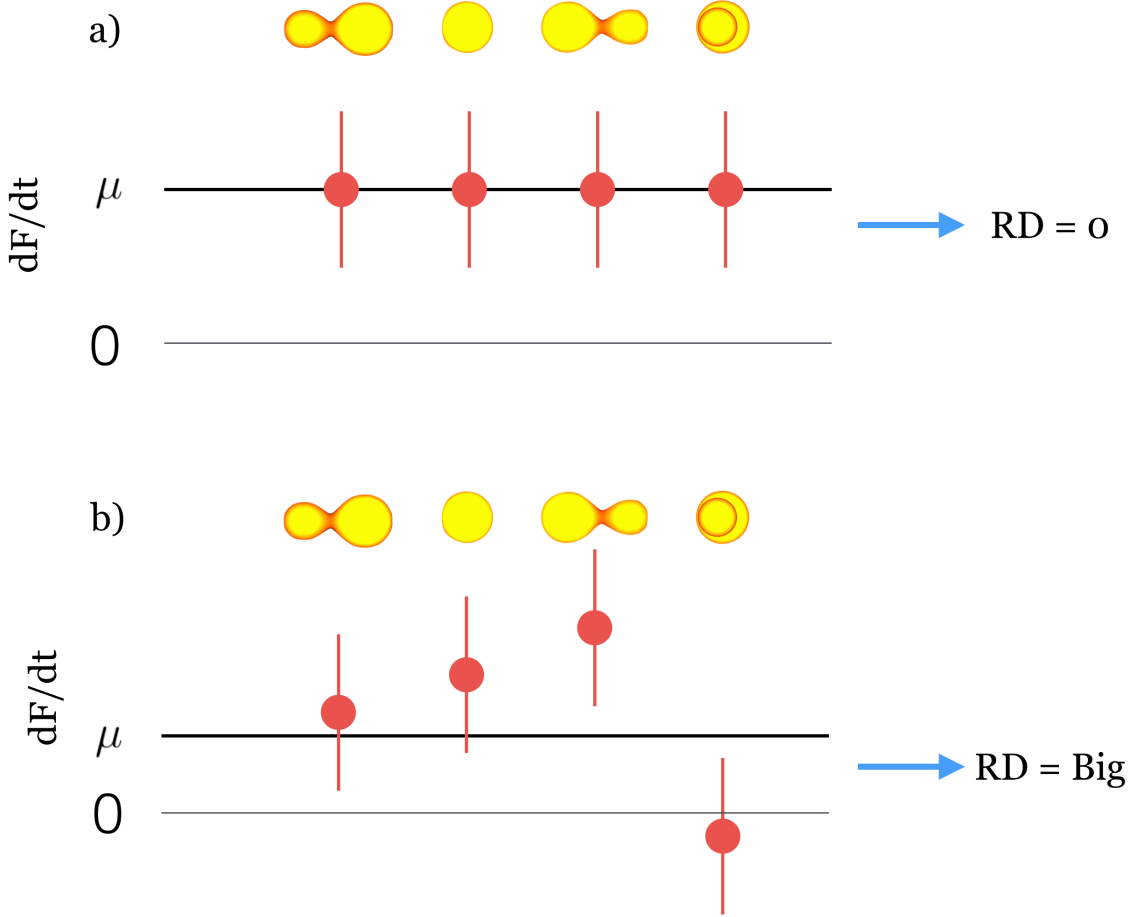


Figure 55: A visual explanation of the Region Disagreement metric. In the top panel (a), all of the  $\dot{F}$  measurements are equal, leading to an RD of zero. In the bottom panel (b), the four  $\dot{F}$  do not agree on a single value, leading to a larger RD value.

$$RD = \frac{|\dot{F}(\text{Max1}) - \mu|}{\delta\dot{F}(\text{Max1})} + \frac{|\dot{F}(\text{Min1}) - \mu|}{\delta\dot{F}(\text{Min1})} + \frac{|\dot{F}(\text{Max2}) - \mu|}{\delta\dot{F}(\text{Max2})} + \frac{|\dot{F}(\text{Min2}) - \mu|}{\delta\dot{F}(\text{Min2})} \quad (5.13)$$

The RD can be described as the sum of the distances of the individual  $\dot{F}$  measurements from the weighted mean  $\mu$ , in units of the  $1\sigma$  uncertainty  $\delta\dot{F}$ . RD provides us a way to rank systems according to the evidence for light-curve changes that are not uniform across all phases.

## 6 Results

### 6.1 $\dot{F}$ and Photospheric Temperature

In this section, we determine which contact binaries exhibit the largest changes in their luminosity. For each binary, we take the weighted mean of the  $\dot{F}$  measurements in the four light-curve regions  $\mu$ . We then bin the binaries by photospheric temperature, calculated by SDSS as described in §5.2. We compute the mean of the  $\mu$  values in bins and plot the mean and  $1\sigma$  standard error of the mean as a function of bin center temperature. In Fig. 56 we see a coherent pattern in mean  $\mu$  as a function of photospheric temperature. Contact binaries with  $T_{\text{eff}} > 6200\text{K}$  show a small mean  $\dot{F}$ , typically around 0.15. The data show that contact binaries with  $5500\text{K} \leq T_{\text{eff}} \leq 6200\text{K}$  are the most variable on decadal timescales. These are the contact binaries with the shallowest convective envelopes. We observe that the mean  $|\dot{F}|$  is the same in minima regions (Min1 and Min2) and maxima (Max1 and Max2) regions (see Fig. 57).

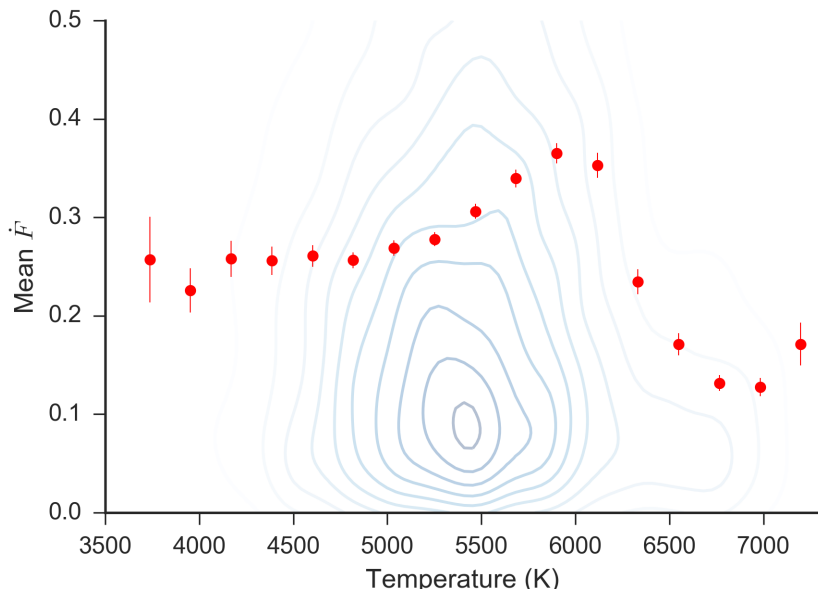


Figure 56: The weighted mean of  $|\dot{F}|$  in each light-curve region, binned as a function of photospheric temperature, represented as red points with error-bars. The light contours show a kernel-density estimate of the underlying distribution.

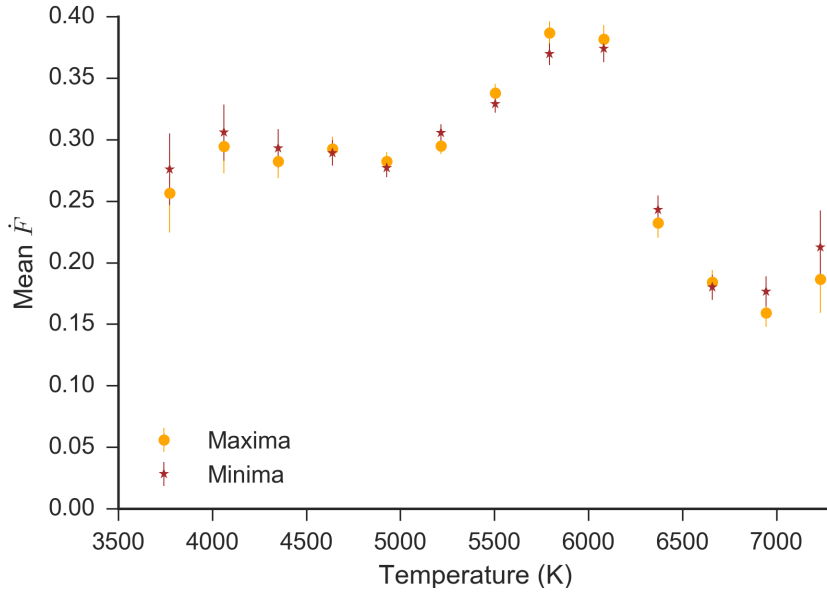


Figure 57: Similar to Fig. 56, except that the weighted mean of  $|\dot{F}|$  is computed separately for the maxima light-curve regions (Max1, Max2, orange circles), and the minima light-curve regions (Min1, Min2, brown stars). We observe that there is no difference in the qualitative behavior of the weighted means.

## 6.2 Region Disagreement and Photospheric Temperature

We must first test the RD metric against instrumental effects. In the magnitude range of this study  $13.5 < V_{CSS} < 19.0$ , mean photometric uncertainty increases monotonically with  $V_{CSS}$ . If photometric uncertainties are measured and propagated incorrectly, the distribution of the Region Disagreement will change as a function of  $V_{CSS}$ . In Fig. 58, we observe that the mean RD metric is stable across the range of  $V_{CSS}$ , indicating that photometric errors and saturation effects do not strongly influence this metric.

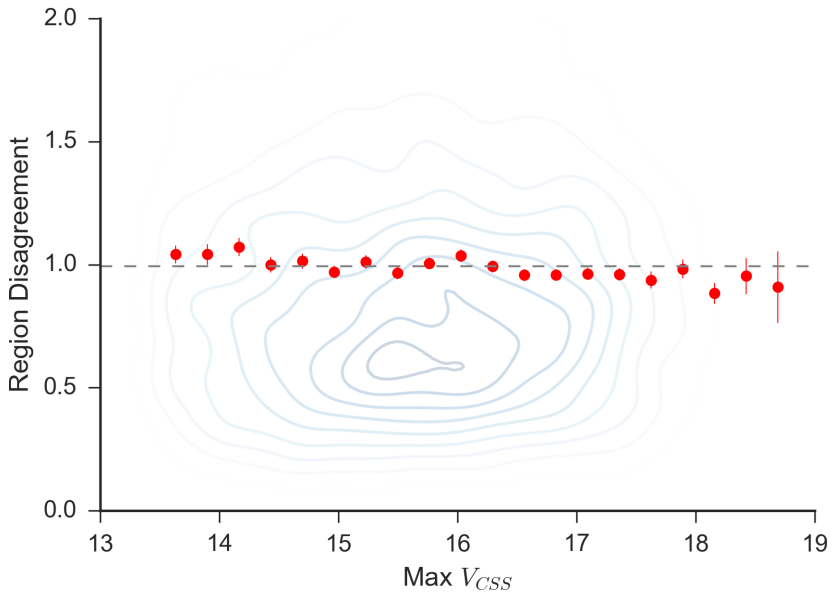


Figure 58: The mean Region Disagreement as a function of binary magnitude  $V_{CSS}$ . The mean of the distribution is very close to 1. We see that this metric has the same mean value across the range of  $V_{CSS}$  by observing the trend of the red points.

In Fig. 59, we see how the mean RD changes as a function of photospheric temperature. For contact binaries with convective envelopes  $T \leq 6200K$ , the mean RD decreases monotonically with increasing temperature. This means that evidence for inhomogeneous spotting increases as the temperature of the contact binary decreases.

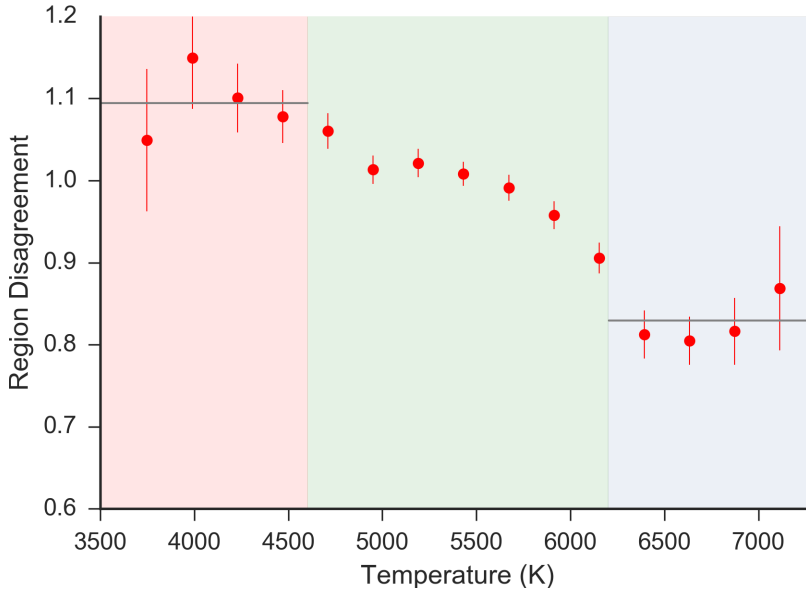


Figure 59: The mean of the Region Disagreement (RD) metric, computed in 15 bins (bin width = 240K). The mean RD is at a constant low value for contact binaries with radiative envelopes ( $T \geq 6200K$ , shaded in light blue). For contact binaries with convective envelopes, mean RD decreases with increasing temperature.

### 6.3 Correlation of Changes between Light-Curve Regions

An initial examination of the  $\dot{F}$  measurements for the four light-curve regions reveals that the  $\dot{F}$  measurements are weakly correlated. In Fig. 60, we see the scatterplot matrix of the  $\dot{F}$  trend for each light-curve region. The resulting Pearson  $R^2$  correlation coefficients can be seen in Fig. 61. Examine the correlation matrix, we see that for the whole sample of 8,389 binaries, the two maxima (Max1, Max2) exhibit the strongest correlation in  $\dot{F}$  ( $R^2 = 0.35$ ). For the whole sample, the two minima (Min1, Min2) regions exhibit the weakest correlation in  $\dot{F}$  ( $R^2 = 0.20$ ). All of the regions containing one minima region and one maxima region had a similar  $R^2$  correlation coefficient of  $\approx 0.3$ .

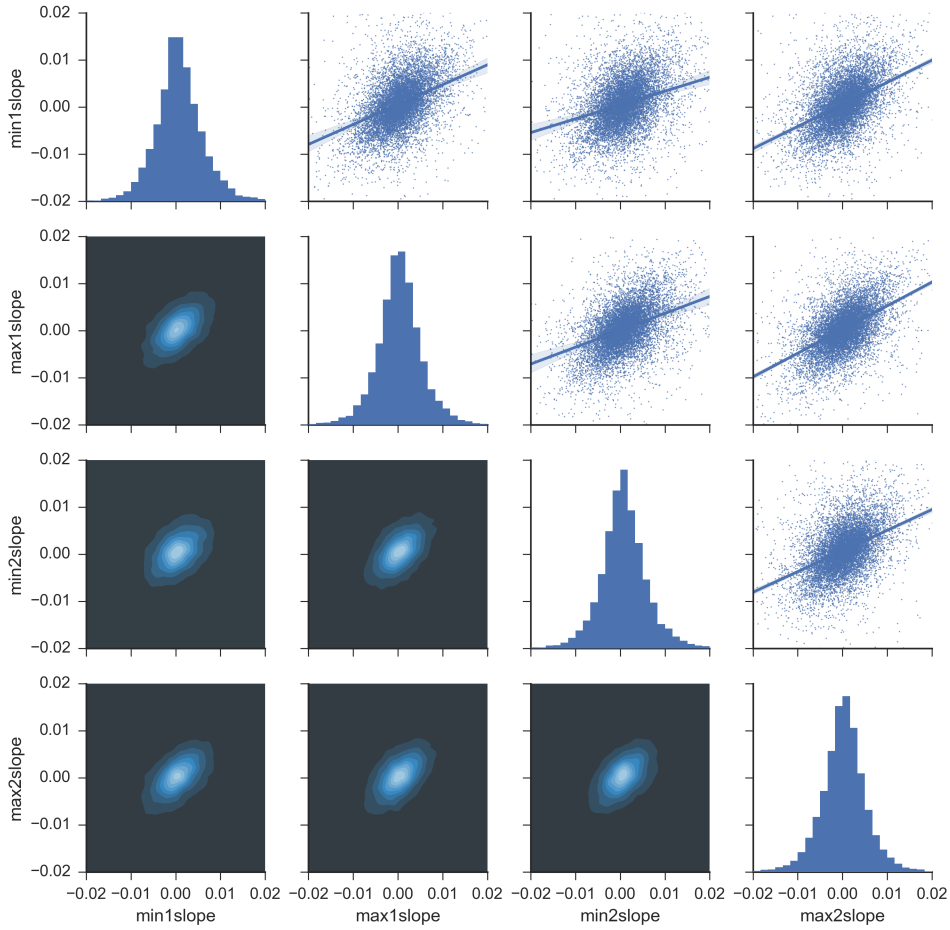


Figure 60: A scatterplot matrix of the  $\dot{F}$  measurements for each light-curve region, computed for 8,389 contact binaries in the final sample. The diagonal subplots are histograms of the univariate distributions. The plots below the diagonal are plots of the gaussian kernel-density estimate. The plots above the diagonal are scatterplots, with the line of best fit overplotted. The Pearson  $R^2$  coefficients for this matrix can be seen in Fig. 61.

Next, we will investigate if the correlation between the light-curve regions depends on the  $T_{\text{eff}}$ , the photospheric temperature of the system. First, we check for differences in the correlation between the minima light-curve regions in sample of 500 binaries of solar temperature, and a sample of 500 cooler binaries (see Fig. 62). Looking at the density plots, it appears that the systems in the solar-temperature sample exhibits much better correlation between  $\dot{F}(\text{Min1})$  and  $\dot{F}(\text{Min2})$ , than the sample of cooler systems.

	Min1	Max1	Min2	Max2
Min1	1.0	0.28	0.2	0.29
Max1	0.28	1.0	0.3	0.35
Min2	0.2	0.3	1.0	0.28
Max2	0.29	0.35	0.28	1.0

Figure 61: Diagonal matrix of the Pearson  $R^2$  correlation coefficient of the  $\dot{F}$  measurement for each light-curve region (Min1, Max1, Min2, Max2), computed for 8,389 contact binaries in the final sample.

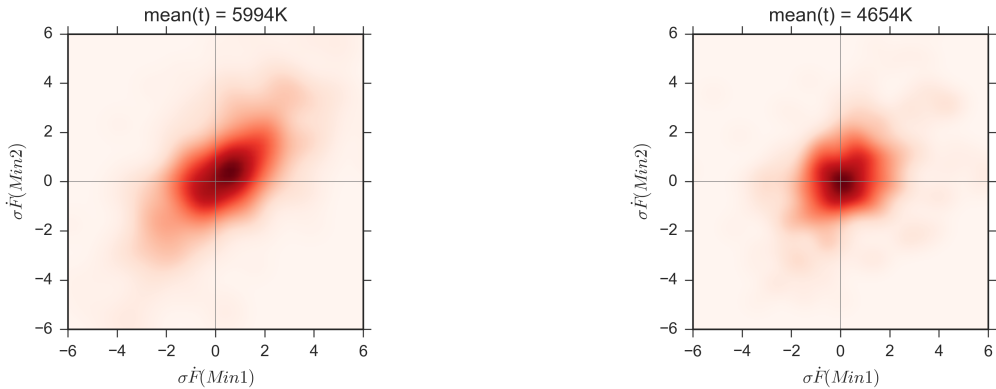


Figure 62: The correlation between  $\dot{F}$  in the light-curve minima for solar-temperature contact binaries (left) and cool contact binaries (right). Note that the solar-temperature contact binaries exhibit a much better correlation between  $\dot{F}$  measurements, while the  $\dot{F}$  measurement for the cool contact binaries are essentially uncorrelated.

Encouraged by this result, we can divide our sample of contact binaries into many subsamples, each with a different temperature, and compute the correlation coefficients to see how the Pearson  $R^2$  coefficient evolves as a function of photospheric temperature (see Fig. 63).

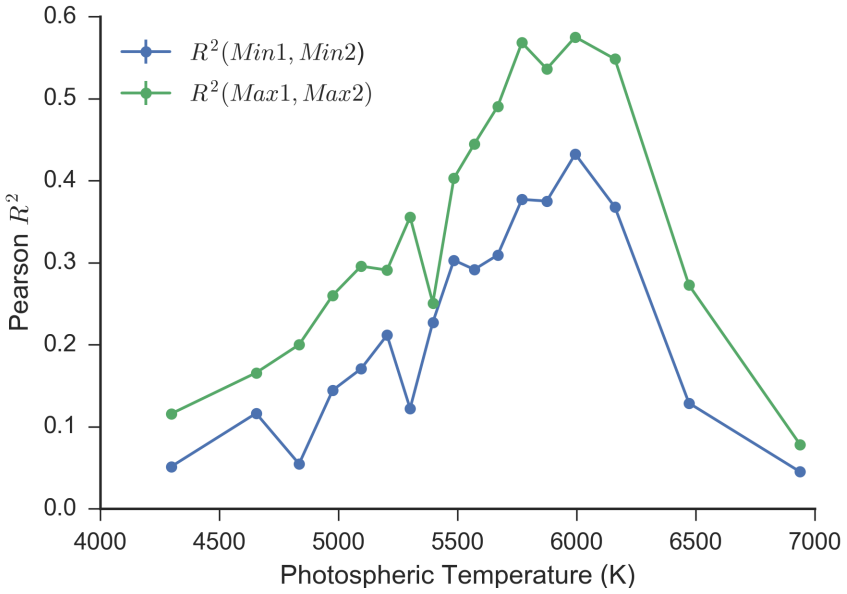


Figure 63: The Pearson  $R^2$  coefficient between the  $\dot{F}$  measurements of light-curve regions Min1, Min2 (in blue), and Max1, Max2 (in green).

We observe that for all values of the temperature, the correlation between the light-curve maxima is stronger than the correlation between the light-curve minima. We observe that both the maxima and the minima correlation follows the same pattern: increasing from low values at low temperature, until a maximum is achieved at  $5800K \leq T \leq 6200K$ . For  $T \geq 6200K$ , the  $R^2$  correlation between light-curve regions rapidly decreases.

We can interpret these results in light of what we have observed about how the mean  $\dot{F}$  changes as a function of photospheric temperature (see Fig. 56). For systems with  $T \geq 6200K$ , the mean  $\dot{F}$  is very low. This means that the light-curves don't change and most of the  $\dot{F}$  measurements for individual light-curve measurements are 0, rendering them uncorrelated. We know that the mean  $\dot{F}$  is large for systems with  $5800K \leq T \leq 6200K$ , we also see that the Pearson  $R^2$  correlation coefficient is also large. This means that contact binaries of solar type form spots, but uniformly across the whole photosphere. Low temperature contact binaries  $T \leq 4500K$  still have a moderate value of  $\dot{F}$ , but the Pearson  $R^2$  correlation between light-curve regions is low. This means that low temperature contact binaries form spots, but not uniformly across the photosphere. This agrees with the conclusion provided by the RD analysis: that evidence of inhomogeneous spot formation increases with decreasing photospheric temperature.

## 6.4 Conclusions

We study the changes in light-curve shape of 8,389 contact binaries in the Catalina Surveys Variable Star Catalogue. We examine white-light photometry taken during the years of 2005 to 2013 for changes in light-curve shape. We find that binaries with photospheric temperatures ranging from  $5700K \leq T_{\text{eff}} \leq 6200K$  have the most variable light-curves. For every light-curve, we compute the change in flux per year for four separate regions in light-curve phase. We compute the  $R^2$  correlation coefficient for all possible combinations of light-curve regions. We find that the flux change in light-curve regions of binaries with  $T_{\text{eff}} \leq 4500K$  are the least correlated, while those of binaries with  $5,700K \leq T_{\text{eff}} \leq 6,000K$  exhibit the strongest correlation. This supports the hypothesis that the uniformity of the photospheric surface brightness distribution increases with increasing photospheric temperature for convective binaries ( $T_{\text{eff}} \leq 6200K$ ).

On contact binaries, we find that the starspot formation can be left-right asymmetric, with starspots forming on one side of the components independently of the spotting behavior on the other side. Starspots can form and disappear independently on the two components. This is especially true for systems with a low effective temperature. Our biggest finding is that starspot behavior changes dramatically as a function of effective temperature of the system. For systems with  $T \leq 4500K$ , the spotting behavior in each of the light-curve regions is largely independent. Starspots can form on one component of the binary, without forming on the other. Starspots can form on the left side of the binary, without forming on the right side. For systems with  $5500K \leq T \leq 6200K$ , the change in brightness of the light-curve regions is highly correlated. If starspots are forming on one component, they will also be forming on the other. If starspots are forming on the left side of the binary, they will also be forming on the right side.

The depth of the binary convective envelope decreases with increasing photospheric temperature. This suggests that for binaries with deep convective envelopes, the dynamo mechanisms for each of the component are independent, whereas for binary with shallow convective envelopes, the dynamo mechanisms are somehow related. Simulations of the common envelope of contact binary systems are needed to determine what this result means for the interior structure and circulation of the envelope.

## 7 The Future

In this section, I'd like to outline a few projects that are possible with existing datasets. I will also summarize a few future surveys that I believe have great potential to improve our understanding of contact binary systems.

### 7.1 Coronal Rotation with GALEX

GALEX is a NASA Small Explorer class ultraviolet survey instrument launched in April 2003. The optical system (a 50cm diameter modified Ritchey-Chretien telescope) focuses starlight onto two photon-counting microchannel-plate (MCP) detectors that can image the sky in Far Ultraviolet (FUV) and Near Ultraviolet (NUV) bands simultaneously. The FUV band spans 134.4nm to 178.6nm with an effective wavelength of 152.8nm. The NUV band spans 177.1nm to 283.1nm with an effective wavelength of 227.1nm. The two detectors produce a point-spread-function with a full-width at half-maximum smaller than 4.5 arcseconds (FUV) and 6.0 arcseconds (NUV) in diameter. GALEX operates in three survey modes: Approximate All-sky (AIS), Medium Imaging (MIS), and Deep Imaging (DIS). The AIS has a  $5\sigma$  limiting magnitude of 19.9 in the FUV Band and 20.8 in the NUV band [Morrissey et al., 2005]. Morrissey et al. [2007] provides a description of the GALEX data product. GALEX catalog photometry can be accessed via the CASJobs framework [O'Mullane et al., 2005] at <https://galex.stsci.edu/casjobs/>.

The GALEX satellite has completed a  $\pi$  steradian (quarter of the sky) imaging survey. GALEX has also completed a deep imaging survey, where a small portion of the sky was imaged for a long time. The two (FUV, NUV) detectors on GALEX are *photon counting*, meaning that they record the time of arrival (to 5 milliseconds) and location (x,y pixel coordinate) of each incident photon. The python package `gphoton` allows the user to easily access and download GALEX photon-counting data (<https://archive.stsci.edu/prepds/gphoton/>). The user can construct light-curves out of the individual photon counts, to perform a periodicity analysis.

McGale et al. [1996] have shown that the coronal rotation rate of convective contact binaries can be measured by using X-ray light-curves. For a sample of hundreds of contact binaries in the CRTS sample, a researcher can compare the orbital period as computed from the UV light-curve with the orbital period computed from the optical light-curve. The differential rotation rate of contact binary coronas can be measured for a sample with a variety of orbital periods, temperatures, and orbital inclinations, which should give insight into the coronal morphology of contact binary systems.

## 7.2 Period Changes with Evryscope

Evryscope is a wide-field, high-entendue survey instrument [Law et al., 2015]. It can perform photometry on the entire visible night-sky, down to magnitude  $V \approx 16$ . This places thousands of known contact binaries within its reach. What makes Evryscope special is its cadence:  $V$ -band photometry will be performed every 2-minutes on every star in the visible sky. The cadence of Evryscope enables complete light-curves to be constructed for each night of observing. The cadence of this data means that traditional  $O - C$  analysis can be used to analyze period changes for thousands bright contact binaries. These analyses will be extremely sensitive to period changes due to tertiary components and imminent merger[Lohr et al., 2015]. One can request Evryscope data by emailing Nick Law at `nmlaw-at-physics-dot-unc-dot-edu`.

## 7.3 H $\alpha$ Fluxes in PTF

The Palomar Transient Facility is an all-sky survey. In addition to taking images in the  $r$  and  $g$  bands, PTF also observes in the narrowband H $\alpha$  [Law et al., 2009]. In the coronas of active stars H $\alpha$  is an emission line. The strength of the H $\alpha$  line is another indicator of coronal activity. Comparing and contrasting H $\alpha$  excesses as observed by PTF with GALEX UV colors and optical variability data from CRTS should yield interesting results.

## 7.4 Future Surveys

We are only beginning to enter the era of all-sky surveys. There are many upcoming surveys that will provide data useful in understanding contact binary systems. Multi-band surveys like Pan-STARRS can provide multi-band light-curves for contact binary stars [Kaiser et al., 2010] . Multi-band light-curves are exciting because they can be used to construct temperature curves, which can in turn be used to measure the difference between the temperature of the two photospheres. Temperature can be used to check that the common-envelope is truly isothermal, and yet have not been collected for large numbers of contact binary stars. Future space-based missions will also contribute to the study of contact binary stars. In addition to being a precise photometer, ESA's Gaia satellite performs parallax-based astrometry for hundreds of contact binaries [De Bruijne, 2012]. The Hipparcos distance measurements were critical to calibrating the contact binary period-luminosity relationships. Gaia will allow for a much better relationship to be calibrated. Future surveys like the Zwicky Transient Facility, or ZTF, will feature better cadence and photometric precision [Smith et al., 2014]. This will make it possible to study photospheric brightness changes in greater detail. The Large Synoptic Survey Telescope, or LSST will be able to see contact binaries at immense

distances [Ivezic et al., 2008]. LSST will produce the largest sample of contact binaries ever observed, and will enable the identification of systems in rare evolutionary states. These upcoming datasets will allow the modern researcher to answer a whole new set of questions about these fascinating systems (Fig. 64). As we can see, the future is bright for contact binary stars!



Figure 64: Four future surveys that will have a big impact on the field of contact binary study. At top left, the camera array for the Zwicky Transient Facility. At top right, the dome for the Pan-STARRS1 telescope. At bottom left, a schematic of the LSST telescope. At bottom right, an illustration of the Gaia spacecraft.



# Characterization of 9380 contact binaries from the CRTS Variable Sources Catalogue

F. M. Marsh,<sup>1</sup> T. A. Prince,<sup>2</sup> A. A. Mahabal,<sup>2</sup> E. C. Bellm,<sup>2</sup> A. J. Drake<sup>2</sup>  
and S. G. Djorgovski<sup>2</sup>

<sup>1</sup>Department of Physics and Astronomy, Pomona College, Claremont, CA 91711, USA

<sup>2</sup>Astronomy Department, California Institute of Technology, Pasadena, CA 91126, USA

Accepted 2016 August 19. Received 2016 August 18; in original form 2016 June 20

## ABSTRACT

We construct a sample of 9380 contact binaries (W UMa systems) by using the Catalina Real-Time Transient Survey Variables Sources Catalogue. By measuring brightness change rates, light-curve statistics, and temperatures for this sample, we improve the understanding of contact binary light-curve characteristics, and luminosity variability on decadal time-scales. We show that binaries with convective outer envelopes have a different distribution of light-curve amplitudes and magnitude differences between eclipse minima than binaries with radiative outer envelopes. We find that more than 2000 binaries exhibit a linear change in mean brightness over the 8-yr timespan of observations with at least  $3\sigma$  significance. We note that 25.9 per cent of binaries with convective outer envelopes exhibit a significant change in brightness, while only 10.5 per cent of radiative binaries exhibit a significant change in brightness. In 205 binaries (2.2 per cent), we find that a sinusoid model better describes the luminosity trend within the 8-yr observation timespan. For these binaries, we report the amplitudes and periods (as estimated using observed half-periods) of this sinusoidal brightness variation and discuss possible mechanisms driving the variation.

**Key words:** surveys – binaries: eclipsing – stars: magnetic field.

## 1 INTRODUCTION

Since their first physical characterization in the late 1960s (Lucy 1968a,b), great advancements have been made in the understanding of contact binary (or W UMa) systems. W UMa systems consist of two main-sequence stars that are so close to each other that they exchange mass and energy through a region of physical contact. Analysis of contact binary light curves reveals that the systems exhibit Roche geometry, where a combination of gravitational and rotational forces combine to give contact systems their characteristic ‘peanut-like’ shapes. These systems are interesting because they provide a unique opportunity to study phenomena such as stellar magnetic activity (Applegate 1992), angular momentum loss (Vilhu & Rahunen 1981), and thermal relaxation oscillations (Wang 1994). A merger of a contact binary system has been observed in time series photometric data (Tylenda et al. 2011), indicating that these systems can rapidly destabilize. Connections of stellar merger events to red novae and blue stragglers have been brought to light in recent literature (Andronov, Pinsonneault & Terndrup 2006). Studies of large numbers of contact systems can provide information about

the mechanisms that cause brightness fluctuations and orbital period changes.

Before the 1990s, studies were limited to small numbers of contact systems because of technological constraints. The light curves necessary for the comparison of different contact systems were time consuming to obtain by using single system photoelectric and CCD photometry, because it took an entire night of observing to obtain a light curve of just one contact system. Still, carefully assembled samples of tens of contact systems with common characteristics allowed for comparative studies to be performed (Davidge & Milone 1984; O’Connell 1951; Qian 2001).

Since the late 1990s, photometric surveys that frequently observe large areas of the sky have come online. Through the careful classification of periodic variable sources in survey data sets, larger and larger samples of contact binary systems have been assembled, making studies of contact binaries as a population possible. Previous surveys have compiled variable star catalogues which include many contact binary systems. Examples of such surveys are the All-Sky Automated Survey (Pojmanski 2000), Robotic Optical Transient Search Experiment (Akerlof et al. 2000), Trans-Atlantic Exoplanet Survey (Devor et al. 2008), Lincoln Near-Earth Asteroid Research program (LINEAR; Palaversa et al. 2013), and Catalina Real-Time Transient Survey (CRTS; Drake et al. 2014a). Researchers have also

\* E-mail: fmarsh@caltech.edu

selected pure samples of contact binary systems from large survey data sets for study. Researchers have previously used data from the Optical Gravitational Lensing Experiment (Rucinski 1996), Super Wide Angle Search for Planets (Norton et al. 2011), and CRTS (Drake et al. 2014b) to construct pure contact binary samples for study. Lee (2015) have used this approach to study a pure sample detached eclipsing binaries from the CRTS Variable Sources Catalogue.

In this work, we perform photometric analysis on a large sample of contact binaries from the CRTS Variable Sources Catalogue, by using both Catalina Sky Survey (CSS) and Sloan Digital Sky Survey (SDSS) data. Our aim is to learn how contact binary light-curve morphology changes with photospheric temperature, and to assess the luminosity variability of contact binaries on decadal time-scales. We do not apply physical models to the contact binaries under study, but instead take a phenomenological approach.

In Section 2, we describe the SDSS and CRTS data that we use. In Section 3, we describe how we constructed our sample set from 30 743 contact binaries published in Drake et al. (2014a). In Section 4, we describe light-curve statistics calculated for the 13 551 binaries that were observed in both SDSS and CRTS data. We describe how the temperature was derived from SDSS colours, including de-reddening. We also describe how some systems were removed from our sample based on SDSS colour and harmonic fit characteristics. In Section 5, we search for variability in the luminosity of the candidates on a decadal time-scale, and apply linear and sinusoidal fits to their mean brightness as a function of time. We also describe how some systems were removed from our sample to remove systematic errors in CRTS photometry. In Section 6, we discuss possible mechanisms responsible for the variability of the candidate systems on a decadal time-scale. In Section 7, we summarize our findings and mention the types of future observations that can be used to learn more about contact binary systems.

## 2 OBSERVATIONS

In this study, we use data from two separate surveys: (1) we use CRTS data spanning 8 yr, which allows us for the variation in the luminosity of each system on a decadal time-scale to be measured, and (2) we use SDSS data which provide multiband photometric measurements taken within the timespan of a few minutes, allowing the temperature of each binary to be measured.

### 2.1 CRTS photometry

The CSS uses three telescopes to survey the sky between declinations of  $-75^\circ$  and  $+65^\circ$ . Although the CSS was originally designed for the detection of near-Earth Asteroids, the CRTS project aggregates time series photometry for over 500 million stationary ‘background’ sources (Drake et al. 2009; Djorgovski et al. 2011; Mahabal et al. 2011). CRTS observations are taken in ‘white light’, i.e. without filters, to maximize survey depth. CRTS can perform photometric measurements on sources with visual magnitudes in the range of  $\sim 13\text{--}20$ . Though we only used 8 yr of data, CRTS continues collecting data to this day.

The CRTS photometry used in this work is publicly accessible through the Catalina Surveys Data Release 2 at [crtscaltech.edu](http://crts.caltech.edu).

The number of observations that CSS has collected for the candidate systems that we study ranges from 90 (for the least observed systems) to 540 (for the most observed systems). The median number of CSS observations per candidate system is 336, with a standard deviation of 86 observations. The mean photometric error varies

from 0.05 to 0.10 mag for most systems, increasing as a function of CRTS magnitude.

### 2.2 SDSS photometry

The SDSS provides multiband photometry in the  $u$ ,  $g$ ,  $r$ ,  $i$ , and  $z$  bands. Because of its drift-scanning configuration, SDSS is well suited to performing photometry on short-period variable stars ( $P < 1$  d), because all of the bands are exposed within a short time of each other: there is a delay of roughly 5 min between the exposure of the  $g$  and  $r$  images (York et al. 2000). We use the SDSS DR10 ( $g - r$ ) colour to calculate the temperature of the binary systems in this study (Ahn et al. 2014).

## 3 CANDIDATE SELECTION

The initial set of contact binaries from which we derived our sample was selected as described in Drake et al. (2014a). The CRTS photometry for this sample can be accessed publicly at <http://nesssi.cacr.caltech.edu/DataRelease/Varcat.html> (Drake et al. 2014a).

The Drake et al. (2014a) sample was created by selecting data from the Catalina Surveys Data Release 1, based on the criteria of high Stetson variability index ( $J_{WS}$ ) and large standard deviation of brightness measurements ( $\sigma$ ). Drake performed Lomb–Scargle periodogram analysis (LS; Scargle 1982) on these variables, testing for significant periods. Candidates that passed an LS significance cutoff along with additional data quality cuts were further processed to determine the best period and were then visually inspected. Approximately half of the inspected candidates passed selection and were classified by type (e.g. EW: contact binary, EA: Algol type, RRab: RR Lyrae, etc.) based on period, light-curve morphology, and colour information.

In the Drake et al. (2014a) sample, there are 30 743 binaries classified as EW, corresponding to W UMa (contact) binaries. The SDSS photometry was cross-matched to the CRTS photometry by using the Large Survey Database framework (Juric 2012). We searched for SDSS point sources within 3 arcsec of the coordinates of the CRTS candidates, and when a one-to-one match existed, we correlated the photometry and added the candidate to our sample. When a unique match did not exist between the SDSS and CRTS photometry, we did not add the candidate to our sample. We chose the 3 arcsec search radius because CSS pixels subtend 2.5 arcsec. Out of the 30 743 sources queried, there were 13 551 sources with matching CRTS and SDSS photometry. We will describe the parameters derived for each of these 13 551 binary candidates in Sections 4 and 5.

Drake et al. (2014a) have shown that 98.3 per cent of the sources classified as contact binaries in CRTS data are also classified as contact binaries in the analysis of LINEAR data in Palaversa et al. (2013). They have also shown that many of the candidates have SDSS DR10 spectra consistent with known spectral characteristics of contact binaries. Because our contact binary sample is selected from the Drake subset, we expect that it will also have greater than 98 per cent purity.

## 4 CALCULATION OF TEMPERATURE AND LIGHT-CURVE STATISTICS

In this section, we describe the light-curve statistics for the sample. We also describe how the photospheric temperature was calculated from SDSS colours for the sample. Our aim is to discover how light curves vary as a function of photospheric temperature.

#### 4.1 Light-curve harmonic fit

We used the period derived in Drake et al. (2014a) to phase-fold the photometry of every system. For every system, we performed a six harmonic (six sine terms, six cosine terms) fit of the phase-folded photometry, by using `gatspy` (Vanderplas 2015; VanderPlas & Ivezić 2015). We chose to use six terms in our model because it provides a balance between flexibility to fit complex light-curve shapes and robustness with sparse data. A model with more than six terms performed better at characterizing well-sampled light curves than models with fewer terms. A six-term model, however, was more likely than a model with fewer terms to produce a non-physical shape when the input light curve was sparsely sampled, or sampled unevenly in phase. At best, the harmonic fit is a good approximation of the true continuous light-curve shape, but sometimes this was not the case. When the range of phases is sparsely or unevenly sampled, the fit is poorly constrained, and often exhibits more than two local maxima and more than two local minima, which is not expected in a physical system with Roche geometry (Lucy 1968b). This also occurs if the variation due to an eclipse has an amplitude comparable to the photometric error.

##### 4.1.1 Harmonic fit filters

If the six-term harmonic fit had more than two local maxima and two local minima, we eliminated the system from the sample, because physical eclipsing binary light curves should only have two maxima and two minima (like the light curve in Fig. 3). Other than this criterion, we did not place any constraints on the goodness of fit. This filter eliminated 3062 of the 13 551 systems in the original sample (22.6 per cent), thereby reducing the sample to 10 488 systems.

We compared the distributions of variability amplitude, and mean CSS magnitude ( $V_{\text{CSS}}$ ) for the 3062 systems rejected by the harmonic fit filters to the distributions for the 10 488 systems that passed through the filter. In the top panel of Fig. 1, we see that systems with low variability amplitude ( $< 0.3$  mag) are more common among the 3062 rejected systems. The harmonic fit filter preferentially rejects bright systems, ( $V_{\text{CSS}} < 13.5$ ), and faint systems ( $V_{\text{CSS}} > 17.0$ ).

A system is likely to be rejected when the variability amplitude is comparable to the photometric errors on individual measurements. Thus, low-amplitude systems, and faint systems (which have large photometric errors) are preferentially rejected by the filter. The preferential rejection of the brightest systems is due to additional light-curve scatter introduced by saturation effects in the CRTS photometry.

It is known that the system geometrical element that most strongly affects contact binary light-curve amplitude is the orbital inclination (Rucinski 1993). It has been shown that orbital inclination can be predicted with a precision of  $\pm 3^\circ$  based on light-curve data alone (Zeraatgari et al. 2015). Therefore, preferentially rejecting low-amplitude systems will preferentially reject highly inclined systems which only partially eclipse. Since inclination is not a property that is intrinsic to the contact binary system, this is not expected to introduce a physical bias into our sample.

The rejection of faint systems preferentially rejects systems that are intrinsically dim, and distant. The rejection of bright systems preferentially rejects systems that are intrinsically more luminous and close. In the bottom panel of Fig. 1, we see that systems at both extremes in brightness are rejected by the filter, but more faint systems are rejected than bright systems. This is expected

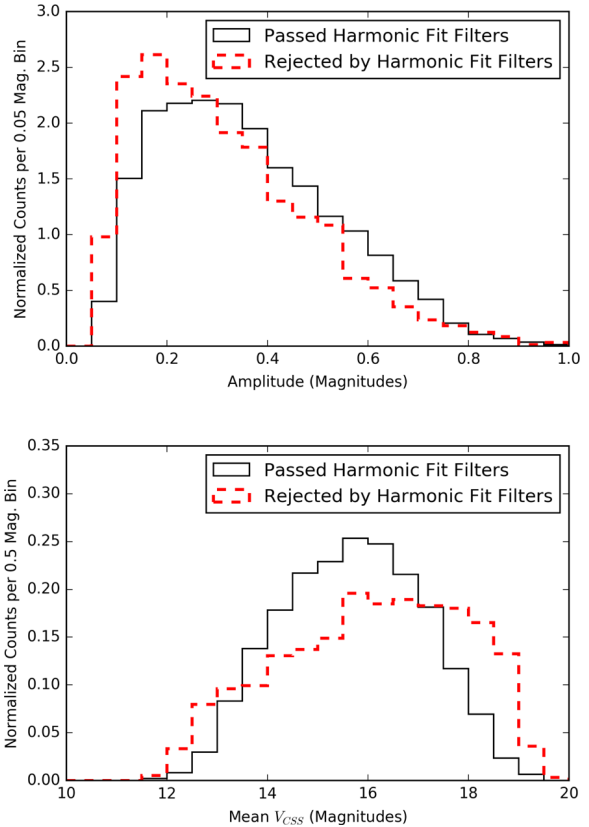


**Figure 1.** Normalized histograms of variability amplitude (top panel), and mean CSS magnitude  $V_{\text{CSS}}$  (bottom panel), for systems retained (black, solid line), and rejected (red, dashed line) by the harmonic fit filters. Systems with low variability amplitude are preferentially rejected by the filters. Systems with mean  $V_{\text{CSS}}$  magnitudes of less than 13.5 (the brightest systems) and mean  $V_{\text{CSS}}$  of greater than 17 (the faintest systems) are preferentially rejected by the filter.

to bias our sample towards more luminous, hotter, more massive contact binaries with longer orbital periods. We note that the initial sample (like all magnitude-limited samples) is biased towards more luminous contact binaries.

We have not attempted to characterize an unbiased population of contact binaries in this work. A complete and unbiased sample of contact binaries is not a requirement for the analysis performed in this work.

#### 4.2 Derived light-curve parameters

For each system in the sample of 10 488, we performed 1000 harmonic fits on Monte Carlo-simulated data sets. Each new simulated photometric measurement was drawn from a normal distribution generated by using the original value of the measurement as the mean, and the reported error as the standard deviation. We sampled these 1000 new harmonic fits at 10 000 uniformly spaced points across their phase, and computed the standard deviation of the fits for each point in phase. This was taken to be the standard error at each point in phase on the harmonic fit (Fig. 2). We then retrieved the magnitude and phase of the relative extrema on the harmonic fits, corresponding to the minima and maxima of the eclipses.

The three light-curve parameters (Fig. 3) that we derive in this analysis are amplitude (Amp), magnitude difference between eclipse minima ( $\Delta \text{Min}$ ), and magnitude difference between

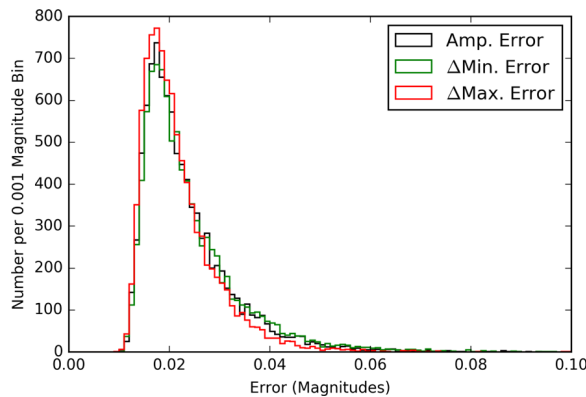


**Figure 2.** The distribution of errors for the parameters derived from the six-term harmonic fit. A characteristic error for Amp,  $\Delta\text{Min}$ , and  $\Delta\text{Max}$  is 0.02 mag.

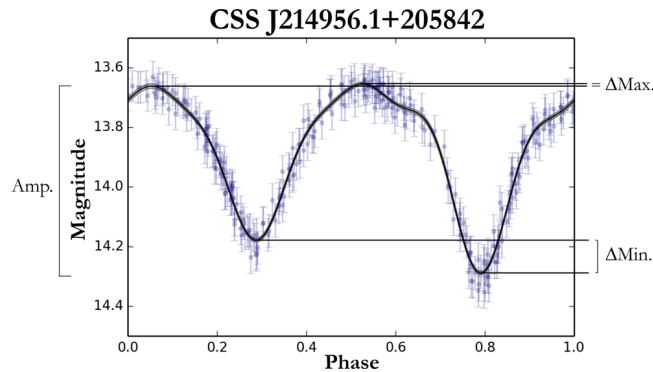


**Figure 3.** A graphical depiction of the light-curve parameters. Note that  $\Delta\text{Max}$  is the very small difference between out-of-eclipse maxima.

out-of-eclipse maxima ( $\Delta\text{Max}$ ). We define these three parameters to be positive.

#### 4.3 Effective temperature

The contact binaries in our sample tended to be further away than those in previous surveys because the contact binaries in our sample were fainter on average than those in previous surveys ( $\sim 13 < V_{\text{CSS}} < 20$ ) and have a limited range ( $2 \lesssim M_V \lesssim 7$ ) of absolute magnitudes (Rucinski & Duerbeck 1997). Consequently, extra care had to be taken with the de-reddening of the SDSS colours.

The recently released 3D dust map derived from Pan-STARRS1 data by Green et al. (2015) has increased the accuracy with which extinction can be calculated, because the extinction is estimated as a function of direction and distance. If a way exists to roughly determine the distance to a contact binary system by using a method not affected by extinction, we can use the 3D dust map to compute the extinction along the line of sight to the estimated distance, and thereby retrieve a more accurate temperature measurement than is possible with a 2D dust map and Galactic latitude correction.

There is a well-known relationship between the period, colour, and absolute magnitude of contact binary systems. Even without colour information, the absolute magnitude of a contact binary system can be calculated based solely upon its period, with a standard error of 0.3 mag. Rucinski (2006) performed a calibration by using the maximum brightness of 21 contact binary systems with  $P < 0.56$  d using *Hipparcos* data and obtained

$$M_V = -1.5 - 12 \log P, \quad (1)$$

where  $P$  is the period in days. This relationship tends to underestimate the absolute magnitude (overestimate the brightness) of systems with  $P > 0.56$  d, by about 0.75 absolute magnitudes. As a result, temperatures will be overestimated for hotter systems. Even with this calibration inaccuracy, the 3D dust map method affords better accuracy than the 2D dust map method, which does not take distance into account at all.

To calculate  $(V - M_V)$ , we used equation (1) and the visual magnitude ( $V$ ) computed from SDSS  $g$  and  $r$  magnitudes via the empirical relationship  $V = g - 0.59 \times (g - r) - 0.01$  (Jester et al. 2005). The SDSS  $g$  and  $r$  measurements used to initially estimate the  $V$ -band magnitude are not corrected for extinction. The difference  $(V - M_V)$  is caused by the dimming due to distance, and the extinction due to reddening. Adopting a ratio of total-to-selective extinction of 3.1, the extinction in the  $V$  band,  $A_V$ , can be expressed as

$$A_V = 3.1 \times E(B - V), \quad (2)$$

where  $E(B - V)$  is the  $(B - V)$  reddening. The Green et al. (2015) dust map allows  $E(B - V)$  to be calculated as a function of distance modulus, i.e.  $E(B - V) = f(D)$ . For each system, we can find a distance modulus such that the sum of the distance modulus and  $V$ -band extinction,  $A_V$ , at that distance modulus is equal to  $(V - M_V)$ , because  $A_V$  is known as a function of distance modulus. In this way, we can find both the extinction and the distance to the system. We find that 90 per cent of the systems had a  $B - V$  reddening,  $E(B - V)$ , of less than 0.20 mag. The median error in  $E(B - V)$  was 0.03 mag.

After the best fit of the distance modulus and  $E(B - V)$  was calculated, we were able to calculate the extinction in each of the SDSS  $ugriz$  bands using the relationships published in Schlafly & Finkbeiner (2011). We converted  $E(B - V)$  to extinctions in each SDSS band. The median extinction in the SDSS  $g$  band was 0.11 mag and the median extinction in the SDSS  $r$  band was 0.08 mag. Approximately 90 per cent of the candidates had an SDSS  $g$  band extinction of less than 0.5 mag. Approximately 90 per cent of the candidates had an SDSS  $r$  band extinction of less than 0.3 mag. The median error in the  $g$  extinction was 0.10 mag and the median error in the  $r$  extinction was 0.07 mag.

We then used an empirical relation (calibrated for main-sequence stars) from Fukugita et al. (2011) to calculate the photospheric temperature of the contact binaries.

$$T_{\text{eff}} / 10^4 \text{ K} = \frac{1.09}{(g - r) + 1.47}. \quad (3)$$

Temperature calculated from  $(g - r)$  colour in this manner carries an uncertainty of 93 K in the empirically verified range of 3850–8000 K, which was added in quadrature to the effects of SDSS photometric error and reddening uncertainties. Over 99 per cent of the systems in the sample lie within the empirically verified range.

We note that SDSS provides a temperature measurement at only one phase of the contact binary rotation. The two component stars of a binary system in true contact have temperatures that are within  $\sim 100$  K of each other. However, this assumption breaks down for semidetached systems with longer orbital periods.

The uncertainty in the SDSS temperature measurement was computed by adding the provided photometric uncertainties, the reddening uncertainties, and the Fukugita et al. (2011) temperature calibration in quadrature. The resulting mean error in the temperature determination was 324 K, with a standard deviation of 153 K. Systems with lower mean magnitudes tended to have a slightly higher error in the SDSS temperature determination. This is

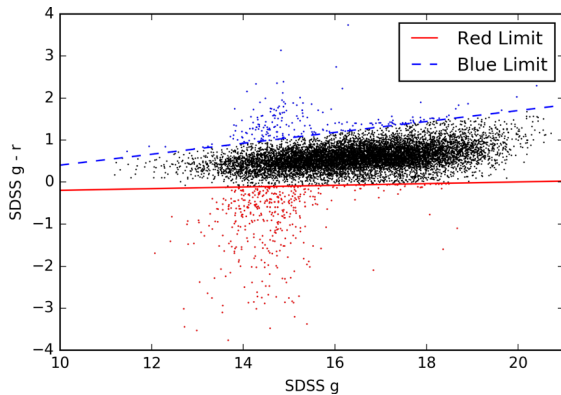


**Figure 4.** The distribution of the sample in SDSS ( $g - r$ ) versus  $g$  colour space, dashed lines show the red and blue limits imposed upon the data. These limits were imposed to eliminate systems with evidence of saturated SDSS photometry. Points in red and blue show the systems rejected by the respective limits. 661 out of the 10 488 systems plotted were eliminated.

because brighter contact binaries are hotter, and hotter binaries tend to have larger temperature errors (because a component of the error is proportional to the temperature).

#### 4.3.1 Colour limits

Some of the 10 488 system remaining after the harmonic fit filters (Section 4.1.1) exhibited colours that are outside the range expected for contact binary systems. The likely cause of this discrepancy is that much of the SDSS  $g$ -band photometry is saturated for  $g < 15$ . Systems with saturated photometry were eliminated by choosing a colour cutoff (Fig. 4). We selected both blue and red limits in SDSS ( $g - r$ ) as a function of SDSS  $g$ . Candidates were selected such that

$$\begin{aligned} (g - r) &> 0.02 \times g - 0.4 \text{ (Red Limit)} \\ (g - r) &< 0.13 \times g - 0.9 \text{ (Blue Limit).} \end{aligned} \quad (4)$$

The  $(g - r)$  colour derived from SDSS photometry has the largest standard deviation in the SDSS  $g$  magnitude range of  $\approx 13\text{--}15$ . Outside of this magnitude range, the systems exhibited a sharp cutoff in  $(g - r)$  colour as a function of temperature. On each end of the distribution, a line was fit by eye to the cutoff in the magnitude ranges of 16–20, which was the source of the red and blue limits. Of the 10 488 binaries in the sample remaining after the first filter, this eliminated 661, for a new total of 9827 systems.

#### 4.4 Light-curve shape and temperature

For each of the 9827 light curves that passed the colour filters (as described in Section 4.3.1), we calculate the amplitude (Amp), difference between eclipse minima ( $\Delta\text{Min}$ ) and the difference between out-of-eclipse maxima ( $\Delta\text{Max}$ ). To generate the plots in this section, we have also filtered out 447 systems that do not pass a criterion described in Section 5.1.1. This is so that the results presented in this section can be compared with those presented in Section 5 (Fig. 5).

The distributions of each of these derived light-curve parameters changes with the effective temperature of the binary system. We find that at certain critical temperatures, many of the characteristics of the systems change.

We discover that the photospheric temperature of 6200 K divides the binaries in multiple parameter distributions (e.g. Figs 6, 7, and 8),

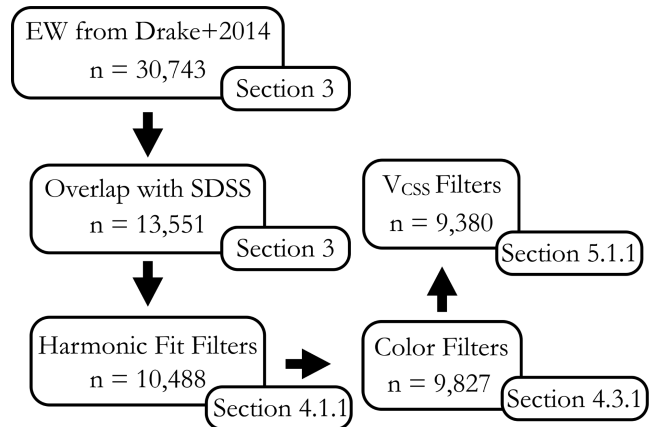


**Figure 5.** A flowchart describing each of the filters applied to the sample. The type of filter is at the top of each box, while the sample size after applying that filter is at the bottom. The section where each filter is described is at the bottom right of each box.

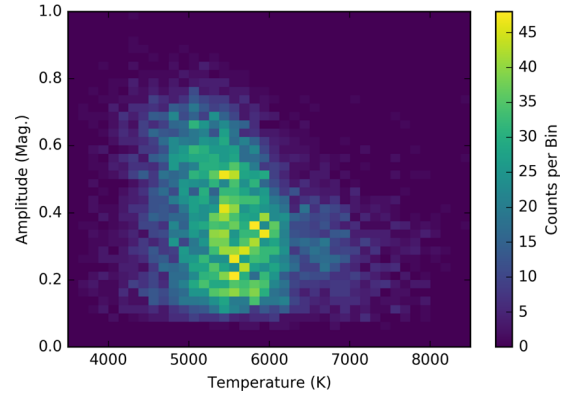


**Figure 6.** A 2D histogram of amplitude and temperature for the sample. Systems with effective temperatures greater than 6200 K generally do not have amplitudes greater than  $\approx 0.5$  mag, while systems with effective temperatures lower than 6200 K do not have amplitudes greater than  $\approx 0.8$  mag. The mean amplitude of the systems cooler than 6200 K is 0.40, with a standard deviation of 0.18. The mean amplitude of the systems hotter than 6200 K is 0.30, with a standard deviation of 0.12.

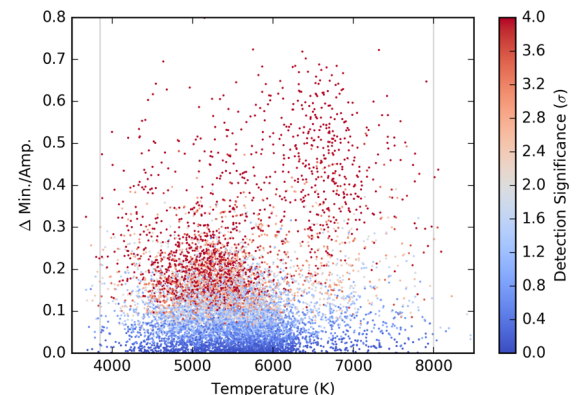


**Figure 7.** The amplitude-normalized  $\Delta\text{Min}$  plotted against temperature. We normalize by amplitude to control for inclination effects. The colour axis describes the significance of the  $\Delta\text{Min}$  measurement.  $\Delta\text{Min}$  measurements that are significant at the greater than  $2\sigma$  level are plotted as red points. Systems with effective temperatures greater than 6200 K can have much larger  $\Delta\text{Min}$  than systems cooler than 6200 K.

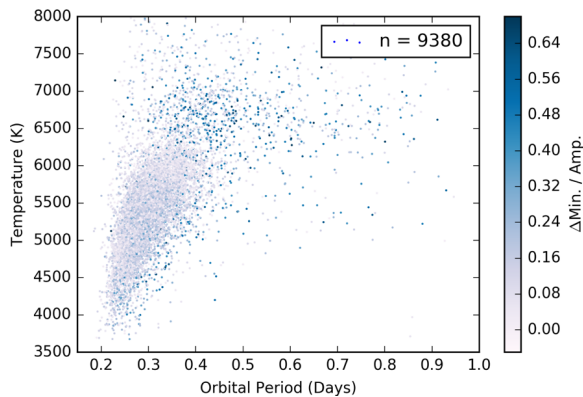


**Figure 8.** The orbital period and temperature of each contact binary system.  $\Delta\text{Min}$  normalized to the eclipse amplitude (Amp) is on the colour axis. We have normalized  $\Delta\text{Min}$  to Amp. to control for inclination effects. Note that radiative binaries ( $T > 6200$  K) tend to have larger differences between eclipse minima.

and this temperature is important physically. The mode of energy transport at the photosphere changes at the temperature of 6200 K (p. 212; Kippenhahn, Weigert & Weiss 1990). Main-sequence stars with temperatures cooler than 6200 K have a convective outer envelope, while stars hotter than 6200 K are radiative at the surface. We will refer to the binary systems hotter than 6200 K as ‘radiative’ and systems cooler than 6200 K as ‘convective’, for short. In our final sample, there are 1381 radiative systems and 7999 convective systems.

Both the system geometry and the inclination of the orbit relative to the earth’s line of sight affect the amplitude of a contact binary light curve. We find that the amplitude distribution of the binaries changes dramatically as a function of temperature, convective systems having a wider distribution of amplitudes (Fig. 6).

The temperatures of the two component stars in a contact binary system affect the magnitude difference between eclipse minima in a contact binary light curve. A temperature difference between the primary and secondary components is the cause of a non-zero  $\Delta\text{Min}$ . We find that the  $\Delta\text{Min}$  distribution changes significantly as a function of temperature (Fig. 7). Radiative systems typically have larger  $\Delta\text{Min}$  than convective systems.

Our data show the well-known period–colour relation (Fig. 8) for contact binaries (Rubenstein 2001). We note that the binaries that are cooler than most other binaries with the same orbital period tend to have larger  $\Delta\text{Min}/\text{Amp}$  than binaries that are in the middle of the period–colour relation. The component stars of a system with a longer orbital period than that of the majority of binaries with similar temperatures are separated by a larger distance, in accordance with Kepler’s Laws. A larger physical separation between the component stars reduces the likelihood that they are in thermal equilibrium. We expect to see a significant  $\Delta\text{Min}$  in systems where the two components are not in thermal equilibrium.

The difference in out-of-eclipse maxima is affected by an asymmetry in the contact binary system (Fig. 9). A contact binary system exhibiting a significant  $\Delta\text{Max}$  is said to exhibit the O’Connell effect (O’Connell 1951). This effect is theorized to be caused by starspots, asymmetric gas impact (Kallrath & Milone 1999), asymmetric distribution of circum-binary matter (Liu & Yang 2003), or Coriolis heating (Zhou & Leung 1990) of the binary’s photosphere. We find that 8862 systems in the sample (94.5 per cent of the sample) do not have  $\Delta\text{Max}$  detectable at greater than  $2\sigma$  significance. We observe that 107 systems (1.1 per cent of the sample) exhibit a  $\Delta\text{Max}$

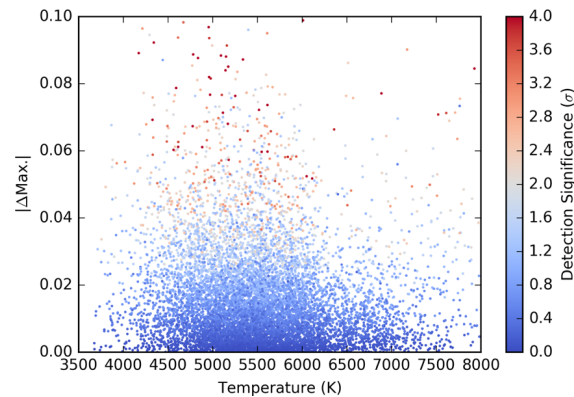


**Figure 9.** The magnitude difference between eclipse maxima plotted against temperature. The colour axis describes the significance of the  $\Delta\text{Max}$  measurement. The vast majority of the systems in the sample do not have a  $\Delta\text{Max}$  detectable at greater than  $2\sigma$ . For light-curve parameters, the typical  $2\sigma$  error is 0.04 mag.

significant at  $3\sigma$ . Drake et al. (2014a) have observed the stability of the O’Connell effect over the 8-yr timespan of CRTS observations in this same sample, providing evidence against the theory that starspots are the cause of the effect. This is because starspots can be observed to appear and disappear during the 8-yr timespan of CRTS observations (Fig. 14). It is likely that the cause of O’Connell effect varies from binary to binary. Wilsey & Beaky (2009) is a review of the possible causes of the O’Connell effect.

## 5 SEARCH FOR LUMINOSITY CHANGES ON A DECADAL TIME-SCALE

### 5.1 Linear brightness parameter

Changes in the mean magnitude of contact binary systems over time-scales of years have previously been attributed to changes in the mean photospheric temperature or mean starspot coverage fraction (Kaszás et al. 1998). To detect luminosity variability on a decadal time-scale, we subtracted the harmonic fit from all of the observations and performed a linear fit on the residuals as a function of time. The six-term harmonic fit effectively eliminated the short-term variability due to the eclipses. When a single harmonic fit is performed on observations with changing mean brightness over the 8-yr timespan of observations, the residuals are minimized for observations in the middle of the time baseline, but the fit is poor for observations at the beginning and end of the time baseline (Fig. 10). We re-fit 1000 Monte Carlo resamplings of the harmonic fit residuals to perform the linear fit error computation (Fig. 11).

#### 5.1.1 Mean magnitude filters

In CRTS data, we find that a systematic error is present in the magnitude derivative calculation. In 2005 and 2006 (the first two years of data in CSDR2), the mean magnitude derivative ( $\dot{V}_{\text{CSS}}$ ) is positive, instead of being close to zero. In the first two years of photometry, a larger photometric aperture was used for the brighter stars in the sample. Light from additional stars within the aperture was added to the calculated flux. When the aperture size was changed in 2006, the light from the additional stars was lost, resulting in an apparent decrease in brightness. This introduces a systematic error when calculating the trend in brightness over time (Fig. 12).

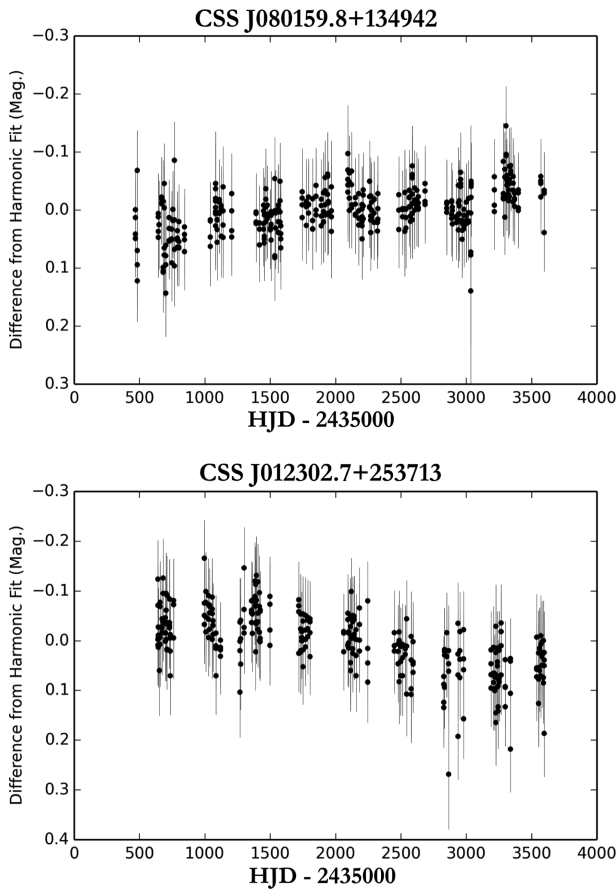


**Figure 10.** The harmonic fit residuals (and  $1\sigma$  error bars) plotted as a function of time for a system with increasing brightness (top), and for a system with decreasing brightness (bottom) over the 8-yr time baseline of CRTS observations. Top panel: CSS\_J080159.8+134942, orbital period = 0.35 d. Bottom panel: CSS\_J012302.7+253713, orbital period = 0.28 d.

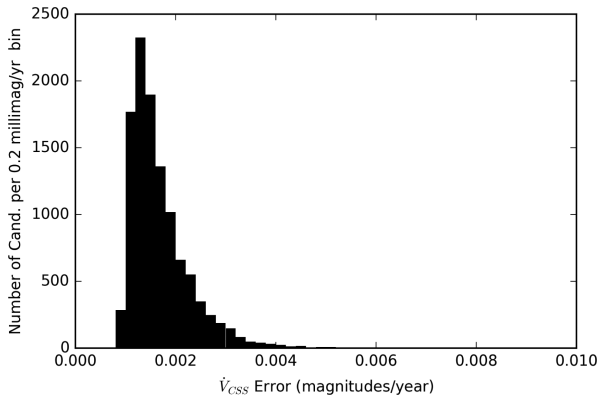


**Figure 11.** Histogram of the estimated error in the magnitude derivative ( $\dot{V}_{\text{CSS}}$ ), if a linear model is assumed. A characteristic error in ( $\dot{V}_{\text{CSS}}$ ) is 0.018 mag per year.

To eliminate this systematic error, we rejected all candidates with a mean  $V_{\text{CSS}}$  of less than 13.5. This ensures that the distribution of magnitude derivatives is symmetric around zero. This filter eliminated 447 systems from the sample of 9827 remaining after the first two filters, to produce the final number of 9380 systems. All of the analysis in Sections 4 and 5 is based on this final sample of 9380. As was previously mentioned, all of the plots in Section 4.4 were generated using the final sample of 9380.

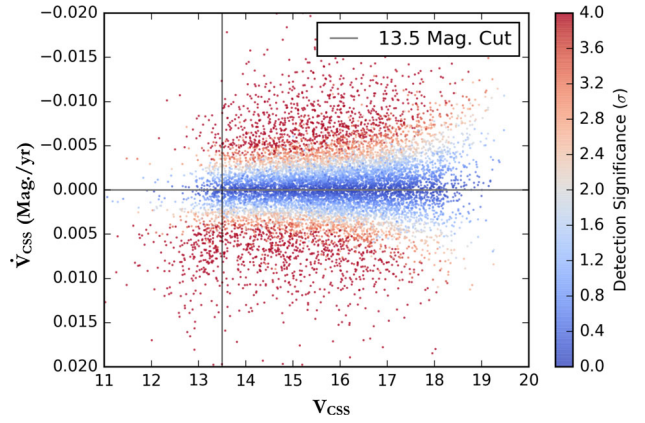


**Figure 12.** The magnitude derivative ( $\dot{V}_{\text{CSS}}$ ) of the systems in the sample during the 8-yr observation time period, plotted as a function of CRTS mean magnitude  $V_{\text{CSS}}$ . The colour axis describes the significance of the  $\dot{V}_{\text{CSS}}$  measurement. For systems brighter than magnitude  $\approx 13.5$ , the distribution of magnitude derivatives is not symmetric around zero, due to changes in the photometric aperture for bright systems. A vertical line is plotted at magnitude 13.5 illustrating the cutoff that we imposed on the data.

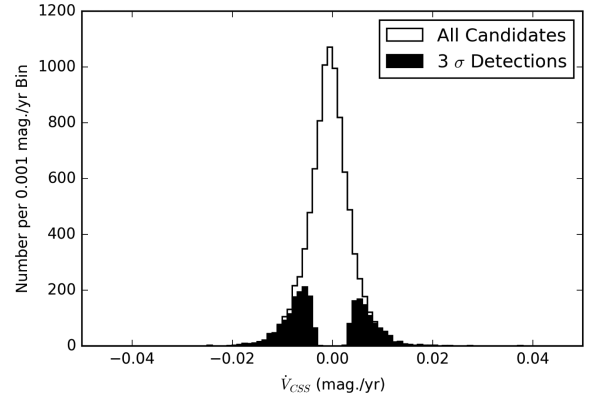


**Figure 13.** Histogram of the magnitude derivative ( $\dot{V}_{\text{CSS}}$ ) in CRTS data. The histogram  $3\sigma$  detections are plotted in black. Of the 9380 systems in the sample, 2219 (23.7 per cent) had linear magnitude changes that were significant at  $3\sigma$ .

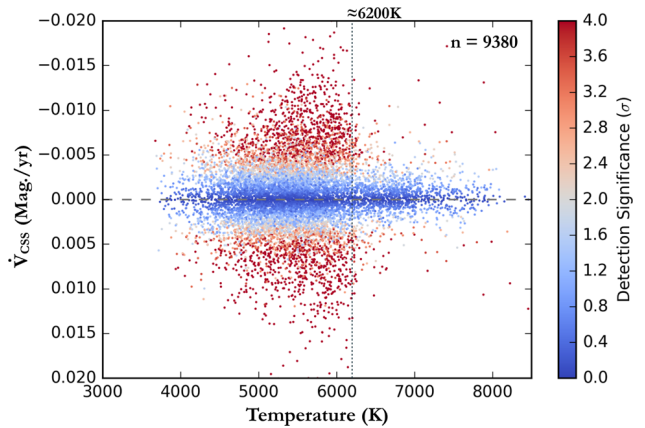


**Figure 14.** The magnitude derivative ( $\dot{V}_{\text{CSS}}$ ) of the systems plotted against their effective temperatures. The colour axis describes the significance of the  $\dot{V}_{\text{CSS}}$  measurement. Systems with effective temperatures greater than  $\approx 6200$  K do not generally exhibit significant changes in their magnitude. A dashed vertical line indicates the temperature of 6200 K.

## 5.2 Linear brightness parameter and temperature

As described in Section 5.1, we fit a line to the residuals of the six-term harmonic fit as a function of time, and assessed the significance of the measured slope (the magnitude derivative). For a  $3\sigma$  detection, the probability of the observed data given the null hypothesis of constant magnitude has to be less than  $1 - 0.997 = 0.003$ . We detected  $3\sigma$  significant magnitude derivatives in 2219 systems (23.7 per cent of the sample). The distribution of magnitude derivatives is symmetric about zero, as ensured by the mean magnitude filter described in Section 5.1.1. We discover that some systems have magnitude derivatives as large as 0.02 mag per year (Fig. 13).

The photospheric temperature of 6200 K separates two distributions of magnitude derivatives. Only 10.5 per cent of the 1381 systems with effective temperatures of greater than 6200 K exhibit brightness changes significant at  $3\sigma$ , while 25.9 per cent of the 7999 systems with effective temperatures of less than 6200 K exhibit  $3\sigma$  significant brightness changes (Fig. 14).

To determine if the luminosity of systems with a large  $\Delta\text{Max}$  (equivalently, systems with a large O'Connell effect) are more likely to vary on a decadal time-scale, we calculated the mean of the  $|\dot{V}_{\text{CSS}}|$  distribution as a function of  $\Delta\text{Max}$  detection significance ( $\sigma$ ) in six discrete bins (Fig. 15). Since the distribution of  $\dot{V}_{\text{CSS}}$  is symmetric about zero, the mean of the absolute value of the distribution is a good way to measure the level of variability. We find that the mean of the  $|\dot{V}_{\text{CSS}}|$  distribution increases smoothly with  $\Delta\text{Max}$  significance ( $\sigma$ ), until the number of systems in each bin is too small to produce reliable statistics. The mean of the  $|\dot{V}_{\text{CSS}}|$  distribution in the  $\Delta\text{Max}(\sigma) = 3\text{--}4$  bin is 1.7 times the mean in the  $\Delta\text{Max}(\sigma) = 0\text{--}1$  bin.

We made an effort to see if the brightness of the systems varied at some orbital phases more than at others. By visually examining the phase-folded light curves of about 20 binaries that exhibited brightness changes significant at  $3\sigma$ , it appears that variable binaries vary at all orbital phases. We observed that some of these light curves varied more on one half of the orbital phase than the other. In this work, we will not comment further on the phase variance of the brightness fluctuations.

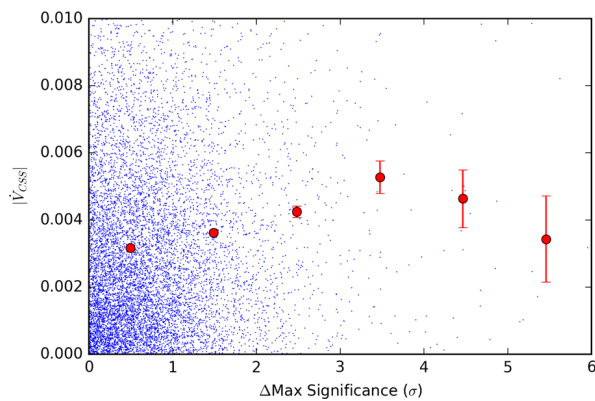


**Figure 15.** The absolute value of the magnitude derivative  $|\dot{V}_{\text{CSS}}|$  plotted against the significance of the O'Connell effect. The mean and standard error of the mean are computed in  $1\sigma$  wide bins, and graphically represented as red points with error bars. The mean of  $|\dot{V}_{\text{CSS}}|$  in the  $\Delta\text{Max}(\sigma) = 3\text{--}4$  bin is  $\approx 0.0053 \text{ mag yr}^{-1}$ , while the mean in the  $\Delta\text{Max}(\sigma) = 0\text{--}1$  bin is  $\approx 0.0032 \text{ mag yr}^{-1}$ . This difference suggests that systems with a large O'Connell effect are more likely to have a variable luminosity on decadal time-scales.

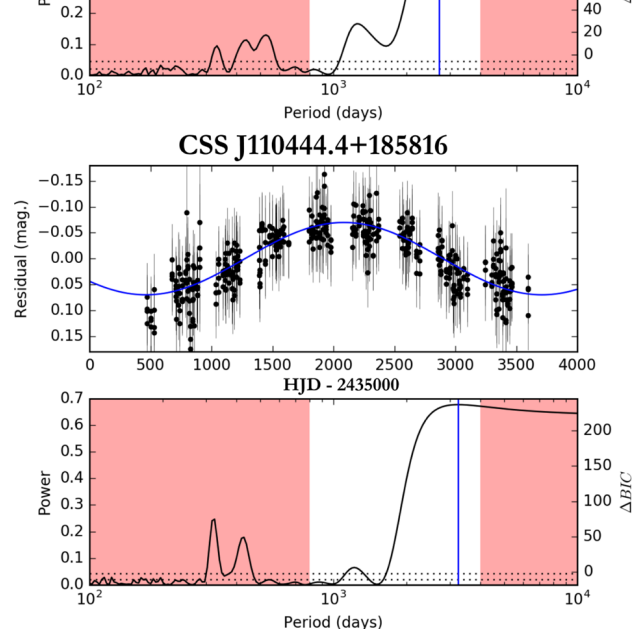
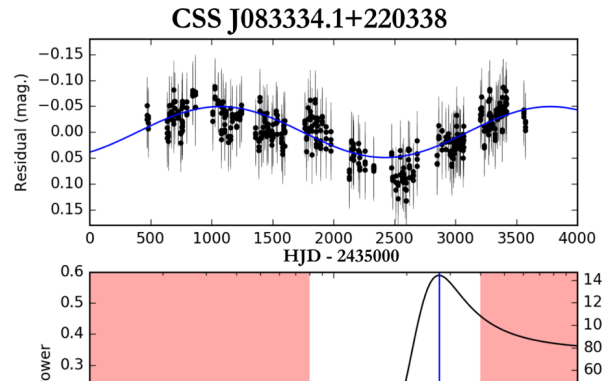


**Figure 16.** Examples of binaries with evidence of sinusoidal variation in luminosity. This figure shows the luminosity trend of the system after the variation due to eclipsing has been subtracted. The harmonic fit residuals are plotted in the top panel of each plot.  $1\sigma$  error bars are plotted for each harmonic fit residual. A Lomb–Scargle periodogram of the residuals is shown in the bottom panel of each plot. The red regions are periods for which the periodogram is influenced by aliases caused by the sampling pattern of the survey. The two dashed lines near the bottom of the Lomb–Scargle plots are the  $1\sigma$  and  $3\sigma$  significance levels for the periodogram, as computed by Monte Carlo resampling. Top panel: CSS\_J10444.4+185816, orbital period = 0.32 d. Bottom panel: CSS\_J083334.1+220338, orbital period = 0.31 d.

## 5.3 Sinusoidal brightness parameters

We find that for some candidates, the trend in harmonic fit residuals as a function of time is not well described by a linear model. While many systems (like those in Fig. 10) exhibit a monotonic increase or decrease in brightness over the 8-yr CRTS time baseline, many others exhibit one or two points of inflection, where the brightness trend reverses in direction (Fig. 16).

In some cases, the trend in the harmonic fit residuals as a function of time appear to be well described by a sinusoid model. This was especially true for systems whose trends have two points of inflection. In order to quantify the number of systems that exhibited sinusoidal trends in brightness over a decadal time-scale, we performed LS periodogram analysis on all of the harmonic fit residuals as a function of time.

We cannot say definitively if the luminosity variation of these systems is truly periodic, because in each case, our observations do not capture multiple ‘cycles’ of the variation. If the variation proves to be truly periodic, we can estimate the period and amplitude of this variation based on observed half-periods. The following analysis assumes that a sinusoid model describes the luminosity variation over time periods longer than the time period of observation. While there are physical reasons to expect that this should be the case (discussed in Section 6), we cannot prove that the luminosity variation is periodic by using CRTS data alone.

The sampling of the CRTS survey and its limited time baseline place limits on the range of luminosity variation periods that we can search. All of the systems are randomly, but uniformly sampled in time, except for gaps that occur every year when the system is only above the horizon in the day and is therefore unobservable by the CSS. This leaves a strong signature in the periodogram of any CSS source (with peaks corresponding to periods of 1 and 2 yr), and thus periodic signals shorter than roughly two years (we chose the cutoff of 800 d) were unable to be measured. The total time baseline of the CRTS survey up to Catalina Surveys Data Release 2 is about 8 yr. Because at least half of a period must be observed to see an inflection point, the 8-yr time baseline sets an upper limit on the longest periods detectable. We chose to filter out all systems with periods of brightness variation that were longer than 11 yr.

A system had to pass several tests to be marked as sinusoidally variable.

(1) The period of the long term luminosity variation as determined by an LS periodogram must be greater than 800 d but less than 4000 d.

(2) The sinusoid model must have a Bayesian information criterion (BIC) of greater than 15, indicating strong evidence for the sinusoid model as compared to the null hypothesis of constant system brightness (Schwarz et al. 1978).

(3) The peak LS power must be five times the  $3\sigma$  power as predicted by 1000 Monte Carlo resamplings – this ensures that only systems with amplitudes large compared to the variation caused by photometric errors alone are considered (VanderPlas, Fouesneau & Taylor 2014).

If a system passed these three tests, a sinusoid model with a period (in years) and an amplitude (in magnitudes) was fit to the harmonic fit residuals as a function of time (Fig. 16).

205 systems in the 9380 binary sample exhibited oscillating brightness variations as discovered by the LS analysis described in Section 5.3. A sinusoid model was fit to the brightness variations with two parameters: (1) period (in years) and (2) amplitude (in magnitudes). We did not compute errors for the parameters of the sinusoid model. From a visual inspection of the LS periodograms, the lower limit on the error in the period determination can be estimated to be 2–3 yr. From a visual inspection of the residuals, we can say that the amplitude is only known to a 30 per cent–40 per cent level, at best. These errors, though large, will not affect the very broad conclusions that we are able to draw from this analysis.

From the difference in magnitude between the system at maximum brightness and the system at minimum brightness, we were able to calculate the difference between the maximum and minimum luminosities (Fig. 17). By assuming that the binaries radiate isotropically, we can calculate the fractional luminosity variance:

$$\frac{|\Delta L|}{L} = \frac{|\Delta F|}{F} = \frac{F_{\max} - F_{\min}}{\bar{F}}. \quad (5)$$

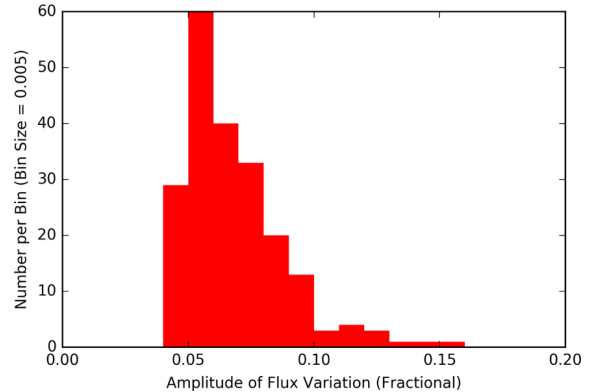


**Figure 17.** A histogram of the fractional flux (equivalently, the fractional luminosity) variation for the 205 binaries in the sinusoid sample. For a given source, the amplitude errors are at least 30 per cent, as discussed in Section 5.3.

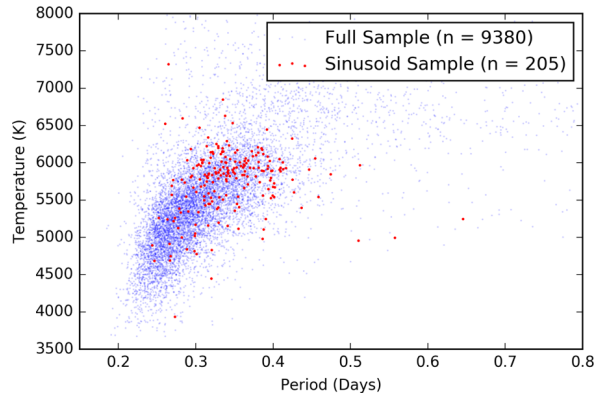


**Figure 18.** The orbital period and temperature of the 9380 systems in the total sample, and the period and temperature of the 205 systems that exhibit significant sinusoidal variation in their brightness detectable on a decadal time-scale. Systems in the sinusoid sample tend to have higher temperatures and longer periods than systems in the remaining sample.

In general, we observe luminosity variability at the 4 per cent level (the lower limit of detection) to the 16 per cent level. We can state that 2.2 per cent of the contact binaries in the whole sample have luminosities that vary by more than 4 per cent on a decadal time-scale, making this a rare phenomenon. If the variable binaries are assumed to be isotropically radiating perfect blackbodies of constant shape and size, then a fluctuation of the mean photospheric temperature with peak to trough amplitudes ranging from 50 to 150 K can explain the observed flux variations.

We note that binaries with temperatures ranging from 5600 to 6300 K are more likely to exhibit periodic luminosity variation (above the 4 per cent level, with a period of less than 11 yr) than binaries outside that temperature range. Very few binaries hotter than 6300 K exhibit this luminosity variation, leading us to speculate that convective activity is responsible for driving the luminosity variation (Figs 18 and 19).

In general, systems with photospheric temperatures of less than  $\approx 4500$  K did not exhibit significant luminosity variation with periods of less than 11 yr. There are two possible explanations: (1) Binaries with temperatures of less than  $\approx 4500$  K could have luminosity variation periods that are longer than 11 yr window or, (2) binaries with temperatures of less than  $\approx 4500$  K could luminosity variation with amplitudes of less than 4 per cent.

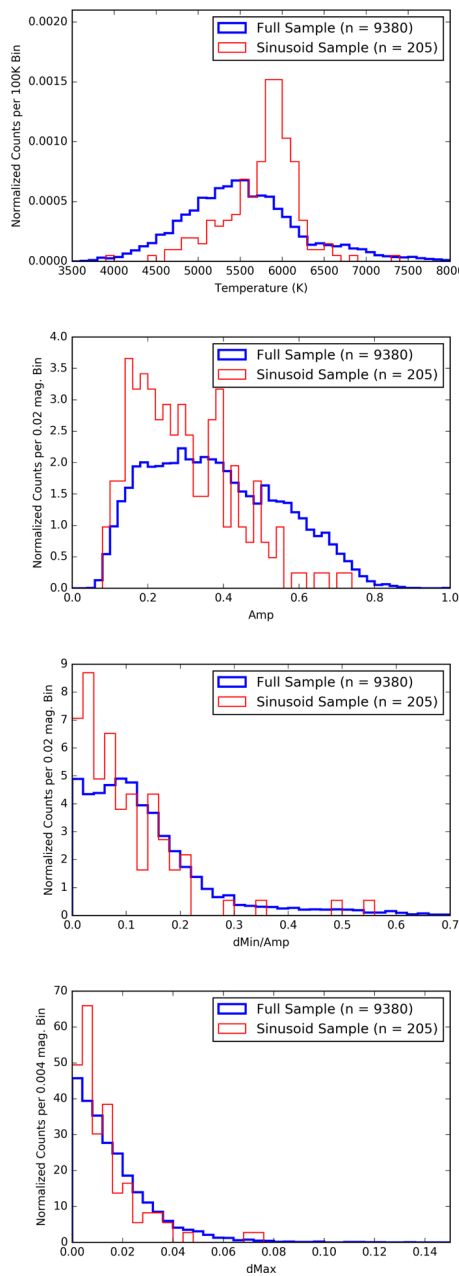


**Figure 19.** Normalized histograms of the temperature, Amp, dMin, dMax, distribution of systems in the whole sample, and systems in the sinusoid sample showing the overabundance of variable systems in the 5600–6300 K temperature range. Systems in the sinusoid sample have a lower mean Amp, and lower dMin/Amp as compared to systems in the full sample of 9380.

Binaries in the sinusoid sample have a lower mean light-curve amplitude (Amp) than binaries in the full sample of 9380 (Fig. 19). This could be a selection effect: binaries with low amplitudes were better fit by the six-term sinusoid model, resulting in smaller errors in the fit residuals. This allowed systems with smaller decadal luminosity variations to pass through the filters as described earlier in Section 5.3. The light-curve amplitude of a contact binary is affected strongly by its orbital inclination with respect to the observer, a property not intrinsic to the binary. Thus, it is unlikely that the difference in the light-curve amplitude distribution has a physical cause.

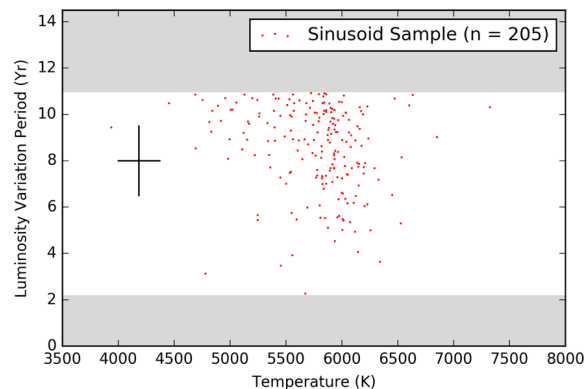


**Figure 20.** The temperature and luminosity variation period of the 205 systems in the sinusoidal sample. In grey are periods that are not detectable in our analysis. Periods shorter than two years are not detectable due to the annual gaps in sampling due to solar conjunction. A representative error bar is included in black.

We searched for a relationship between the photospheric temperature of the binary and the period of the luminosity variation for the 205 binaries in the sinusoid sample (Fig. 20). Given the large errors, there is no clear relationship in the data, except for the slight suggestion that hotter convective binaries (with temperatures closer to 6200 K) exhibit a wide range of luminosity variation periods and are capable of having shorter luminosity variation periods than cooler convective binaries.

We found that four binaries in the sinusoid sample had photospheric temperatures greater than 6200 K at greater than  $1\sigma$  significance. We examined the SDSS imagery manually for these four binaries. Three out of these four binaries had another star of similar brightness within 5 arcsec. It is possible that the varying brightness of the nearby source is causing the binary to be marked as sinusoidally variable. Another explanation is that an error in the de-reddening procedure could have caused a large error in the temperature measurement – causing an overestimate of the temperature of the star. If the variation is intrinsic to the star and our temperature estimate is accurate, a non-convective mechanism must be causing the luminosity variation in these cases.

## 6 DISCUSSION

In this section, we discuss two possible theories that can explain the decadal luminosity changes observed in 2219 binary systems (23.7 per cent of the 9380), with a particular focus on explaining the sinusoidal luminosity variation detected in 205 binary systems (2.2 per cent of the 9380).

### 6.1 The Applegate mechanism

Applegate (1992) has suggested that orbital period modulations of amplitude  $\Delta P/P \approx 10^{-5}$  can be explained by the gravitational coupling of the orbit to variations in the shape of a magnetically active star in the system. Applegate has predicted that the active star be variable at the  $\Delta L/L \approx 0.1$  level, the period of this variability matching the period of the orbital period modulation. This luminosity variation should be entirely caused by a temperature variation since large changes in the radius of the star are ruled out by energetics. Under Applegate's model, the period of the luminosity variation is the same as the period of the magnetic activity cycle of the magnetically active star in the system. A detailed discussion of magnetically driven period changes can be found in Lanza (2006).

We detected luminosity variation at the  $0.04 \leq (\Delta L/L) \leq 0.16$  level in 205 contact binaries. While the period of the luminosity variation is poorly constrained in our data, based on observed half-periods, we can speculate that these 205 binaries have luminosity variation periods ranging from 4 to 11 yr, similar to the solar magnetic activity cycle period of 11 yr. We estimate that fluctuations of the mean photospheric temperature with amplitudes in the range of 50–150 K can explain the observed flux variations for the binaries in our sample. The vast majority of the variable binaries have photospheric temperatures of less than  $\approx 6200$  K, indicating that the mode of energy transport near their surfaces is convective. We do not detect decadal variability above the  $(\Delta L/L) > 0.04$  level in binaries cooler than  $\approx 4500$  K.

The observed behaviour in these 205 contact binaries matches the predictions made by Applegate's theory. If the Applegate mechanism is indeed responsible for the luminosity variation, this study would add to the evidence for short period magnetic activity cycles on W UMa stars (Kaszás et al. 1998; Shengbang & Qingyao 2000; Lee et al. 2004; Zhang & Zhang 2004; Borkovits et al. 2005; Qian et al. 2007; Yang, Qian & Soonthornthum 2012).

## 6.2 Variable starspot coverage

It is possible that starspots are responsible for the variation in brightness observed by CRTS. Doppler imaging techniques have confirmed the presence of large starspots on the surface of some contact binaries (Barnes et al. 2004). The evolution and migration of starspots on contact binaries has been tracked with doppler imaging (Hendry & Mochnacki 2000) and more recently, in *Kepler* data (Tran et al. 2013; Balaji et al. 2015). Starspots are magnetic phenomenon, and so their occurrence is related to the magnetic activity of their host star (Berdyugina 2005). On the sun, the sunspot count varies with the magnetic field strength at the solar surface, which is expected to be true of main-sequence stars in general. As one of the component stars of the contact binary progresses through its magnetic activity cycle, the mean starspot coverage fraction varies, changing the luminosity of the whole system. At this point, we are unsure if the mean photospheric temperature fluctuation of 50–150 K is caused by spots, or is truly a uniform global variation. The fact that luminosity variation can be seen to some extent at all the orbital phases of the 20 phase-folded light curves that we examined by eye leads us to believe that the temperature variation cannot be caused by a localized, large spot, but instead must be caused by many smaller spots distributed evenly on the contact binary surface.

Under either the Applegate model, or the variable spot coverage model, the luminosity variation has a period that is the same as the magnetic activity cycle of one of the stars in the system. If the luminosity variation is caused by either model, we can measure the magnetic activity cycle period of large numbers of contact binaries by measuring their luminosity variation period. In contrast, magnetic activity cycle periods are challenging to measure (Vaughan 1983) in single stars.

## 7 CONCLUSIONS

The photospheric temperature of 6200 K separates binaries into two classes: binaries with convective envelopes ( $T < 6200$  K), and binaries with radiative envelopes ( $T > 6200$  K). We find that radiative binaries generally have larger brightness differences between eclipse minima, indicative of temperature and/or mass differences between the primary and secondary component stars. We find that convective binaries have a larger range of eclipse amplitudes than

radiative binaries. We discover  $3\sigma$  significant brightness changes on a decadal time-scale in roughly 20 per cent of the sample. We find that 23.7 per cent of binaries with convective outer envelopes exhibited a significant change in brightness, while only 10.5 per cent of radiative binaries exhibited a significant change in brightness, leading us to believe that the outer convective envelope of the binary is primarily responsible for driving brightness changes. We have detected luminosity variation at the  $0.04 \leq (\Delta L/L) \leq 0.16$  level in 205 contact binaries (2.2 per cent of the sample). If this luminosity variation proves to be cyclic, we estimate luminosity variation periods ranging from 4 to 11 yr. The characteristics of the observed luminosity variation agree well with the predictions of the Applegate Mechanism, in which a luminosity change at the  $\Delta L/L \approx 0.1$  level can be explained by the gravitational coupling of the orbit to variations in the shape of a magnetically active star in the system. Alternatively, the luminosity variation can be explained by a variation in the mean starspot coverage fraction of the binary photosphere with the same period as the magnetic activity cycle of the primary. Under either model, the luminosity variation period has the same period as the magnetic activity cycle of one of the stars in the system. If the magnetic interpretation of the brightness variation is correct, measuring the period of decadal luminosity variation will also yield the period of its magnetic activity cycle.

Observations of the 205 sinusoidally variable stars over a time baseline of longer than 8 yr will allow us for a more accurate measurement of the period and amplitude of the luminosity variation on a decadal time-scale. Measurements of the temperature history of variable contact binaries over a multiyear time period will help determine if the Applegate Mechanism is a viable explanation of this phenomenon.

We have included the data used in this study in an online table named Marsh et al 2016 Data.csv, accessible via the online version of this work. This table includes the following for each binary: celestial coordinates, the measured orbital period, the light-curve shape parameters described in Section 4.4 and associated errors, the linear brightness parameter described in Section 5.1 and associated errors, the sinusoidal brightness parameters described in Section 5.3 and associated significance levels, the computed photospheric temperature, and the computed levels of extinction in each SDSS band.

## ACKNOWLEDGEMENTS

This work made use of data products from the CSS survey. The CSS survey is funded by the National Aeronautics and Space Administration under Grant No. NNG05GF22G issued through the Science Mission Directorate Near-Earth Objects Observations Program. The CRTS survey is supported by the US National Science Foundation under grants AST-0909182, AST-1313422, AST-1413600, and AST-1518308.

This work made use of data products from the SDSS-III survey. Funding for SDSS-III has been provided by the Alfred P. Sloan Foundation, the Participating Institutions, the National Science Foundation, and the US Department of Energy Office of Science. The SDSS-III web site is <http://www.sdss3.org/>.

SDSS-III is managed by the Astrophysical Research Consortium for the Participating Institutions of the SDSS-III Collaboration including the University of Arizona, the Brazilian Participation Group, Brookhaven National Laboratory, Carnegie Mellon University, University of Florida, the French Participation Group, the German Participation Group, Harvard University, the Instituto de Astrofísica de Canarias, the Michigan State/Notre Dame/JINA

Participation Group, Johns Hopkins University, Lawrence Berkeley National Laboratory, Max Planck Institute for Astrophysics, Max Planck Institute for Extraterrestrial Physics, New Mexico State University, New York University, Ohio State University, Pennsylvania State University, University of Portsmouth, Princeton University, the Spanish Participation Group, University of Tokyo, University of Utah, Vanderbilt University, University of Virginia, University of Washington, and Yale University.

I would like to acknowledge the California Institute of Technology Summer Undergraduate Research Fellowship program for their financial support. I thank an anonymous reviewer for providing comments which greatly improved the paper. I thank James Davenport and Lynne Hillenbrand for their helpful comments, Jake VanderPlas for his help with `gatspy`, and John McBride for his help preparing the manuscript.

## REFERENCES

- Ahn C. P. et al., 2014, *ApJS*, 211, 17  
 Akerlof C. et al., 2000, *AJ*, 119, 1901  
 Andronov N., Pinsonneault M., Terndrup D., 2006, *ApJ*, 646, 1160  
 Applegate J. H., 1992, *ApJ*, 385, 621  
 Balaji B., Croll B., Levine A. M., Rappaport S., 2015, *MNRAS*, 448, 429  
 Barnes J., Lister T., Hilditch R., Cameron A. C., 2004, *MNRAS*, 348, 1321  
 Berdyugina S. V., 2005, *Living Rev. Sol. Phys.*, 2, 8  
 Borkovits T., Elkhatib M., Csizmadia S., Nuspl J., Biró I., Hegedüs T., Csorvási R., 2005, *A&A*, 441, 1087  
 Davidge T., Milone E., 1984, *ApJS*, 55, 571  
 Devor J., Charbonneau D., O'Donovan F. T., Mandushev G., Torres G., 2008, *AJ*, 135, 850  
 Djorgovski S. et al., 2011, in Mihara T., Serino M., eds, *The First Year of MAXI: Monitoring Variable X-ray Sources*. Special Publ. IPCR-127, p. 263  
 Drake A. et al., 2009, *ApJ*, 696, 870  
 Drake A. et al., 2014a, *ApJS*, 213, 9  
 Drake A. et al., 2014b, *ApJ*, 790, 157  
 Fukugita M., Yasuda N., Doi M., Gunn J. E., York D. G., 2011, *AJ*, 141, 47  
 Green G. M. et al., 2015, *ApJ*, 810, 25  
 Hendry P. D., Mochnacki S. W., 2000, *ApJ*, 531, 467  
 Jester S. et al., 2005, *AJ*, 130, 873  
 Juric M., 2012, *Astrophysics Source Code Library*, record ascl: 1209.003  
 Kallrath J., Milone E., 1999, Springer-Velag, New York  
 Kaszás G., Vinkó J., Szatmáry K., Hegedus T., Gal J., Kiss L., Borkovits T., 1998, *A&A*, 331, 231  
 Kippenhahn R., Weigert A., Weiss A., 1990, *Stellar Structure and Evolution*. Springer-Verlag, Berlin  
 Lanza A. F., 2006, *MNRAS*, 369, 1773  
 Lee J. W., Kim C.-H., Han W., Kim H.-I., Koch R. H., 2004, *MNRAS*, 352, 1041  
 Lee C.-H., 2015, *MNRAS*, 454, 2946  
 Liu Q.-Y., Yang Y.-L., 2003, *Chin. J. Astron. Astrophys.*, 3, 142  
 Lucy L., 1968a, *ApJ*, 151, 1123  
 Lucy L., 1968b, *ApJ*, 153, 877  
 Mahabal A. et al., 2011, *Bull. Astron. Soc. India*, 39, 387  
 Norton A. J. et al., 2011, *A&A*, 528, A90  
 O'Connell D., 1951, *Publ. Riverview Coll. Obs.*, 2, 85  
 Palaversa L. et al., 2013, *AJ*, 146, 101  
 Pojmanski G., 2000, *Acta Astron.*, 50, 177  
 Qian S., 2001, *MNRAS*, 328, 635  
 Qian S.-B., Yuan J.-Z., Soonthornthum B., Zhu L.-Y., He J.-J., Yang Y.-G., 2007, *ApJ*, 671, 811  
 Rubenstein E. P., 2001, *AJ*, 121, 3219  
 Rucinski S., 1993, *PASP*, 105, 1433  
 Rucinski S. M., 1996, *AJ*, 113, 1112  
 Rucinski S. M., 2006, *MNRAS*, 368, 1319  
 Rucinski S. M., Duerbeck H. W., 1997, in Perryman M. A. C., Bernacca P. L., Battick B., eds, *ESA SP-402: Absolute Magnitude Calibration for the W UMa-type Contact Binary Stars*. ESA, Noordwijk, p. 457  
 Scargle J. D., 1982, *ApJ*, 263, 835  
 Schlafly E. F., Finkbeiner D. P., 2011, *ApJ*, 737, 103  
 Schwarz G. et al., 1978, *Ann. Stat.*, 6, 461  
 Shengbang Q., Qingyao L., 2000, *Ap&SS*, 271, 331  
 Tran K., Levine A., Rappaport S., Borkovits T., Csizmadia S., Kalomeni B., 2013, *ApJ*, 774, 81  
 Tylenda R. et al., 2011, *A&A*, 528, A114  
 VanderPlas J., 2015, `gatspy`: General tools for Astronomical Time Series in Python. Available at: <http://dx.doi.org/10.5281/zenodo.14833>  
 VanderPlas J. T., Ivezić Ž., 2015, *ApJ*, 812, 18  
 VanderPlas J., Fouesneau M., Taylor J., 2014, *Astrophysics Source Code Library*, record ascl:1407.018  
 Vaughan A., 1983, in Stenflo J. O., ed., *Solar and Stellar Magnetic Fields: Origins and Coronal Effects*. Reidel, Dordrecht, p. 113  
 Vilhu O., Rahunen T., 1981, in Sugimoto D., Lamb D. Q., Schramm D. N., eds, *Proc. IAU Symp. 93, Fundamental Problems in the Theory of Stellar Evolution*. Kluwer, Dordrecht, p. 181  
 Wang J.-M., 1994, *ApJ*, 434, 277  
 Wilsey N. J., Beaky M. M., 2009, *Society for Astronomical Sciences Annual Symposium*, 28, 107  
 Yang Y.-G., Qian S.-B., Soonthornthum B., 2012, *AJ*, 143, 122  
 York D. G. et al., 2000, *AJ*, 120, 1579  
 Zeraatgari F., Abedi A., Farshad M., Ebadian M., Riazi N., 2015, *Contrib. Astron. Obs. Skalnaté Pleso*, 45, 5  
 Zhang X., Zhang R., 2004, *MNRAS*, 347, 307  
 Zhou D.-Q., Leung K.-C., 1990, *ApJ*, 355, 271

## SUPPORTING INFORMATION

Supplementary data are available at [MNRAS](#) online.

[Marshetal2016Data.csv](#)

Please note: Oxford University Press is not responsible for the content or functionality of any supporting materials supplied by the authors. Any queries (other than missing material) should be directed to the corresponding author for the article.

This paper has been typeset from a  $\text{\TeX}$ / $\text{\LaTeX}$  file prepared by the author.

# Index

- $L_2$ , 55  
 $\beta$  Lyrae, 44  
Algol, 45  
angular momentum loss, AML, 31  
black holes, 40  
blue straggler, 38  
CNO-cycle, 8  
convective envelope, 86  
corona, 47  
density, 39  
Early-Type, 23, 40  
Einstein (satellite), 47  
equations of stellar structure, 7  
fill-out factor  $f$ , 15, 36, 48  
Fourier Transform, 58  
frequency, 39  
globular cluster, 38  
gphoton, 87  
Hertzsprung-Russell Diagram, 6  
hydrostatic equilibrium, 17  
Initial Mass Function, 40  
Inner Jacobi Equipotential, 14  
Jacobi equipotentials, 14  
Kempf, Paul Friedrich Ferdinand, 4  
Kozai-Lidov mechanism, 32  
Late-type, 23  
light-curve, 45  
Lomb-Scargle algorithm, 59  
Müller, Karl Hermann Gustav, 4  
Magellanic clouds, 40  
mass ratio  $q$ , 15, 50  
mass transfer, 31  
opacity  $\kappa$ , 7, 22  
orbital period, 26  
period-color relation, 26  
photon, 8  
photon counting, 87  
Potsdam Observatory, 4  
pp-chain, 8, 10  
radial mixing, 24  
red nova, 37  
Roche equipotential, 14  
solar metallicity, 11  
solar wind, 31  
solar-stellar connection, 1  
standard candle, 2  
supernova, 1  
TAMS, Terminal-Age Main-Sequence, 9, 11, 35  
Tau Ceti, 9  
Thermal Relaxation Oscillation, TRO, 20, 56  
time-series, 58  
transients, 1  
Wilson-Devinney Code, 50  
Zöllner's photometer, 4  
ZAMS, Zero-Age Main-Sequence, 9, 11, 20, 27, 28, 30

## References

- Christopher P Ahn, Rachael Alexandroff, Carlos Allende Prieto, Friedrich Anders, Scott F Anderson, Timothy Anderton, Brett H Andrews, Éric Aubourg, Stephen Bailey, Fabienne A Bastien, et al. The tenth data release of the Sloan Digital Sky Survey: First spectroscopic data from the SDSS-III Apache Point Observatory Galactic Evolution Experiment. *The Astrophysical Journal Supplement Series*, 211(2):17, 2014.
- C Akerlof, S Amrose, R Balsano, J Bloch, D Casperson, S Fletcher, G Gisler, J Hills, R Kehoe, B Lee, et al. Rotse all-sky surveys for variable stars. i. test fields. *The Astronomical Journal*, 119(4):1901, 2000.
- Carl Akerlof, C Alcock, R Allsman, T Axelrod, DP Bennett, KH Cook, K Freeman, K Griest, S Marshall, H-S Park, et al. Application of cubic splines to the spectral analysis of unequally spaced data. *The Astrophysical Journal*, 436:787–794, 1994.
- Ivan L Andronov. Phenomenological modeling of the light curves of Algol-type eclipsing binary stars. *Astrophysics*, 55(4):536–550, 2012.
- N Andronov, MH Pinsonneault, and DM Terndrup. Mergers of close primordial binaries. *The Astrophysical Journal*, 646(2):1160, 2006.
- EA Antokhina, M Srinivasa Rao, and M Parthasarathy. Light curve analysis of Hipparcos data for the massive O-type eclipsing binary UW CMA. *New Astronomy*, 16(3):177–182, 2011.
- James H Applegate. A mechanism for orbital period modulation in close binaries. *The Astrophysical Journal*, 385:621–629, 1992.
- B Arbutina. Possible solution to the problem of the extreme mass ratio W UMa-type binaries. *Monthly Notices of the Royal Astronomical Society*, 394(1):501–509, 2009.
- NS Awadalla and MA Hanna. Absolute parameters and mass-radius-luminosity relations for the sub-types of W UMa binaries. *Journal of Korean Astronomical Society*, 38:43–57, 2005.
- Bhaskaran Balaji, Bryce Croll, Alan M Levine, and Saul Rappaport. Tracking the stellar longitudes of starspots in short-period Kepler binaries. *Monthly Notices of the Royal Astronomical Society*, 448(1):429–444, 2015.
- André Balogh, Hugh Hudson, Kristóf Petrovay, and Rudolf Steiger. *The Solar Activity Cycle: Physical Causes and Consequences*, volume 53. Springer, 2015.

JR Barnes, TA Lister, RW Hilditch, and A Collier Cameron. High-resolution doppler images of the spotted contact binary ae phe. *Monthly Notices of the Royal Astronomical Society*, 348(4):1321–1331, 2004.

Svetlana V Berdyugina. Starspots: a key to the stellar dynamo. *Living Rev. Solar Phys.*, 2:8, 2005.

Marvin Bolt, Thomas Hockey, JoAnn Palmeri, Virginia Trimble, Thomas R Williams, Katherine Bracher, Richard Jarrell, Jordan D Marché, and F Jamil Ragep. *Biographical encyclopedia of astronomers*. Springer Science & Business Media, 2007.

T Borkovits, MM Elkhateeb, Sz Csizmadia, J Nuspl, IB Biró, T Hegedüs, and R Csorvási. Indirect evidence for short period magnetic cycles in w uma stars-period analysis of five overcontact systems. *Astronomy & Astrophysics*, 441(3):1087–1097, 2005.

David H Bradstreet and Edward F Guinan. Mapping of surface activity on the w uma-type system vw cephei. 1988.

Bradley W Carroll and Dale A Ostlie. *An introduction to modern astrophysics and cosmology*, volume 1. 2006.

Xiaodian Chen, Richard de Grijs, and Licai Deng. Contact binaries as viable distance indicators: New, competitive (v) jhks period-luminosity relations. *arXiv preprint arXiv:1609.02267*, 2016.

D Coker, S Özdemir, C Yeşilyaprak, SK Yerli, N Aksaker, and BB Güçsav. A study on w ursae majoris-type systems recognised by the rotse-iiid experiment. *Publications of the Astronomical Society of Australia*, 30:e013, 2013.

RG Cruddace and AK Dupree. Contact binary stars. i-an x-ray survey. *The Astrophysical Journal*, 277:263–273, 1984.

JHJ De Bruijne. Science performance of gaia, esa’s space-astrometry mission. *Astrophysics and Space Science*, 341(1):31–41, 2012.

Osman Demircan and Göksel Kahraman. Stellar mass-luminosity and mass-radius relations. *Astrophysics and Space Science*, 181(2):313–322, 1991.

Jonathan Devor, David Charbonneau, Francis T O’Donovan, Georgi Mandushev, and Guillermo Torres. Identification, classifications, and absolute properties of 773 eclipsing binaries found in the trans-atlantic exoplanet survey. *The Astronomical Journal*, 135(3):850, 2008.

SG Djorgovski, AJ Drake, AA Mahabal, MJ Graham, C Donalek, R Williams, EC Beshore, SM Larson, J Prieto, M Catelan, et al. The catalina real-time transient survey (crts). *arXiv preprint arXiv:1102.5004*, 2011.

AJ Drake, SG Djorgovski, A Mahabal, E Beshore, S Larson, MJ Graham, R Williams, E Christensen, M Catelan, A Boattini, et al. First results from the catalina real-time transient survey. *The Astrophysical Journal*, 696(1):870, 2009.

AJ Drake, SG Djorgovski, D García-Álvarez, MJ Graham, M Catelan, AA Mahabal, C Donalek, JL Prieto, G Torrealba, S Abraham, et al. Ultra-short period binaries from the catalina surveys. *The Astrophysical Journal*, 790(2):157, 2014a.

AJ Drake, MJ Graham, SG Djorgovski, M Catelan, AA Mahabal, G Torrealba, D García-Álvarez, C Donalek, JL Prieto, R Williams, et al. The catalina surveys periodic variable star catalog. *The Astrophysical Journal Supplement Series*, 213(1):9, 2014b.

Antoine Duquennoy and Michel Mayor. Multiplicity among solar-type stars in the solar neighbourhood. ii-distribution of the orbital elements in an unbiased sample. *Astronomy and Astrophysics*, 248:485–524, 1991.

Olin J Eggen. Contact binaries, ii. *Memoirs of the Royal Astronomical Society*, 70:111, 1967.

Z Eker, S Bilir, E Yaz, O Demircan, and M Helvaci. New absolute magnitude calibrations for w ursa majoris type binaries. *arXiv preprint arXiv:0807.4989*, 2008.

Masataka Fukugita, Naoki Yasuda, Mamoru Doi, James E Gunn, and Donald G York. Characterization of Sloan Digital Sky Survey stellar photometry. *The Astronomical Journal*, 141(2):47, 2011.

Qing Gao, Yu Xin, Ji-Feng Liu, Xiao-Bin Zhang, and Shuang Gao. White-light flares on close binaries observed with Kepler. *arXiv preprint arXiv:1602.07972*, 2016.

K Gazeas and K Stępień. Angular momentum and mass evolution of contact binaries. *Monthly Notices of the Royal Astronomical Society*, 390(4):1577–1586, 2008.

KD Gazeas. Physical parameters of contact binaries through 2-d and 3-d correlation diagrams. *Communications in Asteroseismology*, 159:129–130, 2009.

KD Gazeas and PG Niarchos. Masses and angular momenta of contact binary stars. *Monthly Notices of the Royal Astronomical Society: Letters*, 370(1):L29–L32, 2006.

KD Gazeas, PG Niarchos, and G-P Gradoula. Modeling the 2004.5 brightening of the contact binary v839 oph. In *Close Binaries in the 21st Century: New Opportunities and Challenges*, pages 123–125. Springer, 2006.

Sara J Gettel, Michael T Geske, and Tim A McKay. A catalog of 1022 bright contact binary stars. *The Astronomical Journal*, 131(1):621, 2006.

Gregory M Green, Edward F Schlafly, Douglas P Finkbeiner, Hans-Walter Rix, Nicolas Martin, William Burgett, Peter W Draper, Heather Flewelling, Klaus Hodapp, Nicholas Kaiser, et al. A three-dimensional map of milky way dust. *The Astrophysical Journal*, 810(1):25, 2015.

L Hambálek and T Pribulla. The reliability of mass-ratio determination from light curves of contact binary stars. *Contributions of the Astronomical Observatory Skalnate Pleso*, 43: 27–46, 2013.

Paul D Hendry and Stefan W Mochnacki. Detection of tertiary components in w ursae majoris systems. *The Astrophysical Journal*, 504(2):978, 1998.

Paul D Hendry and Stefan W Mochnacki. Doppler imaging of vw cephei: distribution and evolution of starspots on a contact binary. *The Astrophysical Journal*, 531(1):467, 2000.

RW Hilditch, ID Howarth, and TJ Harries. Forty eclipsing binaries in the small magellanic cloud: fundamental parameters and cloud distance. *Monthly Notices of the Royal Astronomical Society*, 357(1):304–324, 2005.

T Hovatta, V Pavlidou, OG King, A Mahabal, B Sesar, R Dancikova, SG Djorgovski, A Drake, R Laher, D Levitan, et al. Connection between optical and  $\gamma$ -ray variability in blazars. *Monthly Notices of the Royal Astronomical Society*, page stt2494, 2014.

Bruce J Hrivnak. Radial velocity studies and absolute parameters of contact binaries. ii-oo aquilae. *The Astrophysical Journal*, 340:458–467, 1989.

VA Hughes and BJ McLean. Radio observations of w ursae majoris stars. *The Astrophysical Journal*, 278:716–720, 1984.

Zeljko Ivezić, JA Tyson, B Abel, E Acosta, R Allsman, Y AlSayyad, SF Anderson, J Andrew, R Angel, G Angel, et al. Lsst: from science drivers to reference design and anticipated data products. *arXiv preprint arXiv:0805.2366*, 2008.

Željko Ivezić, Andrew J Connolly, Jacob T VanderPlas, and Alexander Gray. *Statistics, Data Mining, and Machine Learning in Astronomy: A Practical Python Guide for the Analysis of Survey Data*. Princeton University Press, 2014.

Sebastian Jester, Donald P Schneider, Gordon T Richards, Richard F Green, Maarten Schmidt, Patrick B Hall, Michael A Strauss, Daniel E Vanden Berk, Chris Stoughton, James E Gunn, et al. The Sloan Digital Sky Survey view of the Palomar-Green Bright Quasar Survey. *The Astronomical Journal*, 130(3):873, 2005.

Mario Juric. LSD: Large Survey Database Framework. *Astrophysics Source Code Library*, 1: 09003, 2012.

H Kähler. On the structure of contact binaries. *Astronomy & Astrophysics*, 395(3):907–913, 2002.

H Kähler. The structure of contact binaries. *Astronomy & Astrophysics*, 414(1):317–333, 2004.

Nick Kaiser, William Burgett, Ken Chambers, Larry Denneau, Jim Heasley, Robert Jedicke, Eugene Magnier, Jeff Morgan, Peter Onaka, and John Tonry. The Pan-STARRS Wide-Field Optical/NIR Imaging Survey. In *SPIE Astronomical Telescopes+ Instrumentation*, pages 77330E–77330E. International Society for Optics and Photonics, 2010.

A Kalimeris, H Rovithis-Livaniou, and P Rovithis. On the orbital period changes in contact binaries. *Astronomy and Astrophysics*, 282:775–786, 1994.

A Kalimeris, H Rovithis-Livaniou, and P Rovithis. Starspots and photometric noise on observed minus calculated (o-c) diagrams. *Astronomy & Astrophysics*, 387(3):969–976, 2002.

Josef Kallrath and Eugene F Milone. *Eclipsing binary stars: modeling and analysis*. Springer, 2009.

Josef Kallrath, EF Milone, Dirk Terrell, and Andrew T Young. Recent improvements to a version of the Wilson-Devinney program. *The Astrophysical Journal*, 508(1):308, 1998.

G Kaszás, J Vinkó, K Szatmáry, T Hegedus, J Gal, LL Kiss, and T Borkovits. Period variation and surface activity of the contact binary VW Cephei. *Astronomy and Astrophysics*, 331:231–243, 1998.

R Kippenhahn and H-C Thomas. A simple method for the solution of the stellar structure equations including rotation and tidal forces. In *Stellar Rotation*, pages 20–29. Springer, 1970.

Rudolf Kippenhahn, Alfred Weigert, and Achim Weiss. *Stellar structure and evolution*, volume 44. Springer, 1990.

Zdenek Kopal. Close binary systems. *The International Astrophysics Series, London: Chapman & Hall*, 1959, 1959.

Kevin Krisciunas. A brief history of astronomical brightness determination methods at optical wavelengths. *arXiv preprint astro-ph/0106313*, 2001.

M Kubiak, A Udalski, and MK Szymanski. Period changes of contact binaries in ogle database. *Acta Astronomica*, 56:253–265, 2006.

LV Kuhi. A possible flare on w ursae majoris. *Publications of the Astronomical Society of the Pacific*, 76(453):430–432, 1964.

Antonino F Lanza. Internal stellar rotation and orbital period modulation in close binary systems. *Monthly Notices of the Royal Astronomical Society*, 369(4):1773–1779, 2006.

Nicholas M Law, Shrinivas R Kulkarni, Richard G Dekany, Eran O Ofek, Robert M Quimby, Peter E Nugent, Jason Surace, Carl C Grillmair, Joshua S Bloom, Mansi M Kasliwal, et al. The palomar transient factory: system overview, performance, and first results. *Publications of the Astronomical Society of the Pacific*, 121(886):1395–1408, 2009.

Nicholas M Law, Octavi Fors, Jeffrey Ratzloff, Philip Wulfken, Dustin Kavanagh, David J Sitar, Zachary Pruett, Mariah N Birchard, Brad N Barlow, Kipp Cannon, et al. Evryscope science: exploring the potential of all-sky gigapixel-scale telescopes. *Publications of the Astronomical Society of the Pacific*, 127(949):234, 2015.

C-H Lee, J Koppenhoefer, S Seitz, R Bender, A Riffeser, M Kodric, U Hopp, J Snigula, C Gössl, R-P Kudritzki, et al. Properties of m31. v. 298 eclipsing binaries from pandromeda. *The Astrophysical Journal*, 797(1):22, 2014.

Jae Woo Lee, Chun-Hwey Kim, Wonyong Han, Ho-Il Kim, and Robert H Koch. Period and light variations for the cool, overcontact binary bx pegasi. *Monthly Notices of the Royal Astronomical Society*, 352(3):1041–1055, 2004.

Lifang Li, Fenghui Zhang, Zhanwen Han, and Dengkai Jiang. Formation and evolution of w ursae majoris contact binaries. *The Astrophysical Journal*, 662(1):596, 2007.

ME Lohr, AJ Norton, UC Kolb, DR Anderson, Francesca Faedi, and Richard G West. Period decrease in three superwasp eclipsing binary candidates near the short-period limit. *Astronomy & Astrophysics*, 542:A124, 2012.

ME Lohr, AJ Norton, SG Payne, RG West, and PJ Wheatley. Orbital period changes and the higher-order multiplicity fraction amongst superwasp eclipsing binaries. *arXiv preprint arXiv:1505.00941*, 2015.

J Lorenzo, I Negueruela, AKF Val Baker, Miriam García, Sergio Simón-Díaz, P Pastor, and M Méndez Majuelos. My camelopardalis, a very massive merger progenitor. *Astronomy & Astrophysics*, 572:A110, 2014.

SH Lubow and FH Shu. On the structure of contact binaries. ii-zero-age models. *The Astrophysical Journal*, 216:517–525, 1977.

LB Lucy. The light curves of w ursae majoris stars. *The Astrophysical Journal*, 153:877, 1968a.

LB Lucy. The structure of contact binaries. *The Astrophysical Journal*, 151:1123, 1968b.

LB Lucy and RE Wilson. Observational tests of theories of contact binaries. *The Astrophysical Journal*, 231:502–513, 1979.

AA Mahabal, SG Djorgovski, AJ Drake, C Donalek, MJ Graham, RD Williams, Y Chen, B Moghaddam, M Turmon, E Beshore, et al. Discovery, classification, and scientific exploration of transient events from the catalina real-time transient survey. *Bull. Astr. Soc. India*, 39:387–408, 2011.

FM Marsh, TA Prince, AA Mahabal, EC Bellm, AJ Drake, and SG Djorgovski. Characterization of 9,380 contact binaries from the crts variable sources catalogue. *Monthly Notices of the Royal Astronomical Society*, page stw2110, 2016.

Mario Mateo, Hugh C Harris, James Nemec, and Edward W Olszewski. Blue stragglers as remnants of stellar mergers—the discovery of short-period eclipsing binaries in the globular cluster ngc 5466. *The Astronomical Journal*, 100:469–484, 1990.

PA McGale, JP Pye, and ST Hodgkin. Rosat pspc x-ray spectral survey of w uma systems. *Monthly Notices of the Royal Astronomical Society*, 280:627–637, 1996.

SW Mochnacki. Contact binary stars. *The Astrophysical Journal*, 245:650–670, 1981.

SW Mochnacki. Accurate integrations of the roche model. *The Astrophysical Journal Supplement Series*, 55:551–561, 1984.

SW Mochnacki and NA Doughty. A model for the totally eclipsing w ursae majoris system aw uma. *Monthly Notices of the Royal Astronomical Society*, 156(1):51–65, 1972.

Lawrence A Molnar, Daniel M Van Noord, Karen Kinemuchi, Jason P Smolinski, Cara E Alexander, Evan M Cook, Byoungchan Jang, Henry A Kobulnicky, Christopher J Spedden, and Steven D Steenwyk. Prediction of a red nova outburst in kic 9832227. 2017.

Patrick Morrissey, David Schiminovich, Tom A Barlow, D Christopher Martin, Brian Blakkolb, Tim Conrow, Brian Cooke, Kerry Erickson, James Fanson, Peter G Friedman, et al. The on-orbit performance of the galaxy evolution explorer. *The Astrophysical Journal Letters*, 619(1):L7, 2005.

Patrick Morrissey, Tim Conrow, Tom A Barlow, Todd Small, Mark Seibert, Ted K Wyder, Tamás Budavári, Stephane Arnouts, Peter G Friedman, Karl Forster, et al. The calibration and data products of galex. *The Astrophysical Journal Supplement Series*, 173(2):682, 2007.

G Muller and P Kempf. A new variable star unusually short period. *The Astrophysical Journal*, 17:201–211, 1903.

Andrew J Norton, SG Payne, T Evans, Richard G West, Peter J Wheatley, DR Anderson, SCC Barros, OW Butters, A Collier Cameron, Damian Joseph Christian, et al. Short period eclipsing binary candidates identified using superwasp. *Astronomy & Astrophysics*, 528:A90, 2011.

William O’Mullane, Nolan Li, Maria Nieto-Santisteban, Alex Szalay, Ani Thakar, and Jim Gray. Batch is back: Casjobs, serving multi-tb data on the web. In *IEEE International Conference on Web Services (ICWS’05)*, pages 33–40. IEEE, 2005.

Lovro Palaversa, Željko Ivezić, Laurent Eyer, Domagoj Ruždjak, Davor Sudar, Mario Galin, Andrea Kroflin, Martina Mesarić, Petra Munk, Dijana Vrbanec, et al. Exploring the variable sky with linear. iii. classification of periodic light curves. *The Astronomical Journal*, 146(4):101, 2013.

Laura R Penny, Cynthia Ouzts, and Douglas R Gies. Tomographic separation of composite spectra. xi. the physical properties of the massive close binary hd 100213 (tu muscae). *The Astrophysical Journal*, 681(1):554, 2008.

G Pojmanski. The all sky automated survey. catalog of about 3800 variable stars. *Acta Astronomica*, 50:177–190, 2000.

DM Popper. Masses of hot main-sequence stars. *The Astrophysical Journal*, 220:L11–L14, 1978.

T Pribulla, JM Kreiner, and J Tremko. Catalogue of the field contact binary stars. *Contributions of the Astronomical Observatory Skalnate Pleso*, 33:38–70, 2003.

Theodor Pribulla and Slavek M Rucinski. Contact binaries with additional components. i. the extant data. *The Astronomical Journal*, 131(6):2986, 2006.

- James Edward Pringle and Richard Alan Wade. Interacting binary stars. 1985.
- D Shanti Priya, K Sriram, KY Shaju, and P Vivekananda Rao. Photometric study of hot contact binaries in smc. *Bull. Astr. Soc. India*, 41:159–172, 2013.
- A Prsa, EF Guinan, EJ Devinney, SG Engle, M DeGeorge, GP McCook, PA Maurone, J Pepper, DJ James, DH Bradstreet, et al. Fully automated approaches to analyze large-scale astronomy survey data. *arXiv preprint arXiv:0904.0739*, 2009.
- A Prša, P Degroote, K Conroy, S Bloemen, K Hambleton, J Giamarco, and H Pablo. Physics of eclipsing binaries: Motivation for the new-age modeling suite. *EAS Publications Series*, 64:259–268, 2013.
- Andrej Prsa, EF Guinan, EJ Devinney, M DeGeorge, DH Bradstreet, JM Giamarco, CR Alcock, and SG Engle. Artificial intelligence approach to the determination of physical properties of eclipsing binaries. i. the ebai project. *The Astrophysical Journal*, 687(1):542, 2008.
- S-B Qian, J-Z Yuan, B Soonthornthum, L-Y Zhu, J-J He, and Y-G Yang. Ad cancri: A shallow contact solar-type eclipsing binary and evidence for a dwarf third component and a 16 year magnetic cycle. *The Astrophysical Journal*, 671(1):811, 2007.
- S-B Qian, J-J Wang, L-Y Zhu, B Soonthornthum, L-Z Wang, EG Zhao, X Zhou, W-P Liao, and N-P Liu. Optical flares and a long-lived dark spot on a cool shallow contact binary. *The Astrophysical Journal Supplement Series*, 212(1):4, 2014.
- Shengbang Qian. Orbital period changes of contact binary systems: direct evidence for thermal relaxation oscillation theory. *Monthly Notices of the Royal Astronomical Society*, 328(3):914–924, 2001.
- Frederic A Rasio. The minimum mass ratio of w ursae majoris binaries. *arXiv preprint astro-ph/9502028*, 1995.
- Eric P Rubenstein. The effect of stellar evolution on population ii contact binaries in the period-color relation. i. equal-mass, marginal contact systems. *The Astronomical Journal*, 121(6):3219, 2001.
- Slavek M Rucinski. Eclipsing binaries in the ogle variable star catalog. iw uma-type systems as distance and population tracers in baade’s window. *The Astronomical Journal*, 113: 407, 1997.
- Slavek M Rucinski. Contact binaries of the galactic disk: Comparison of the baade’s window and open cluster samples. *The Astronomical Journal*, 116(6):2998, 1998.

Slavek M Rucinski. The photometric amplitude and mass ratio distributions of contact binary stars. *The Astronomical Journal*, 122(2):1007, 2001.

Slavek M Rucinski. Luminosity function of contact binaries based on the all sky automated survey (asas). *Monthly Notices of the Royal Astronomical Society*, 368(3):1319–1322, 2006.

Slavek M Rucinski. The short-period end of the contact binary period distribution based on the all-sky automated survey. *Monthly Notices of the Royal Astronomical Society*, 382(1):393–396, 2007.

SM Rucinski. The w uma-type systems as contact binaries. i. two methods of geometrical elements determination. degree of contact. *Acta Astronomica*, 23:79, 1973.

SM Rucinski. Activity of contact binary systems. In *Interacting binaries*, pages 13–49. Springer, 1985.

SM Rucinski. Can full convection explain the observed short-period limit of the w uma-type binaries? *The Astronomical Journal*, 103:960–966, 1992.

SM Rucinski. The realm of interacting binary stars, 1993a.

SM Rucinski. A simple description of light curves of w uma systems. *Publications of the Astronomical Society of the Pacific*, pages 1433–1440, 1993b.

SM Rucinski and B Paczynski. A contact binary systematically changing its brightness. *Information Bulletin on Variable Stars*, 5321:1, 2002.

Jeffrey D Scargle. Studies in astronomical time series analysis. ii-statistical aspects of spectral analysis of unevenly spaced data. *The Astrophysical Journal*, 263:835–853, 1982.

Edward F Schlafly and Douglas P Finkbeiner. Measuring reddening with sloan digital sky survey stellar spectra and recalibrating sfd. *The Astrophysical Journal*, 737(2):103, 2011.

HV Senavci, MB Dogruel, RH Nelson, M Yilmaz, and SO Selam. Precise orbital solutions for kepler eclipsing binaries of w uma type showing total eclipses. *Publications of the Astronomical Society of Australia*, 33, 2016.

Qian Shengbang and Liu Qingyao. A possible connection between the variation of light curve and thechange of the orbital period in the contact binary ck bootis. *Astrophysics and Space Science*, 271(4):331–339, 2000.

Marc Van Der Sluys. Roche potential, 2006. URL <http://hemel.waarnemen.com/Informatie/Sterren/hoofdstuk6.html#h6.2>.

Roger M Smith, Richard G Dekany, Christopher Bebek, Eric Bellm, Khanh Bui, John Cromer, Paul Gardner, Matthew Hoff, Stephen Kaye, Shrinivas Kulkarni, et al. The zwicky transient facility observing system. In *SPIE Astronomical Telescopes+ Instrumentation*, pages 914779–914779. International Society for Optics and Photonics, 2014.

Klaus Staubermann. The trouble with the instrument: Zöllner’s photometer. *Journal for the History of Astronomy*, 31:323, 2000.

K Stepień. Evolutionary status of late-type contact binaries. *Acta Astronomica*, 56:199–218, 2006a.

K Stepień. The low-mass limit for total mass of w uma-type binaries. *Acta Astronomica*, 56:347–364, 2006b.

K Stepień and K Gazeas. Evolutionary scenario for w uma-type stars. *Proceedings of the International Astronomical Union*, 4(S252):427–428, 2008.

K Stepień, JHMM Schmitt, and W Voges. Rosat all-sky survey of w ursae majoris stars and the problem of supersaturation. *Astronomy & Astrophysics*, 370(1):157–169, 2001.

Dirk Terrell. Eclipsing binary stars: Past, present, and future. *Journal of the American Association of Variable Star Observers (JAAVSO)*, 30:1, 2001.

Dirk Terrell and RE Wilson. Photometric mass ratios of eclipsing binary stars. In *Zdeněk Kopal’s Binary Star Legacy*, pages 221–230. Springer, 2005.

K Tran, A Levine, S Rappaport, T Borkovits, Sz Csizmadia, and B Kalomeni. The anti-correlated nature of the primary and secondary eclipse timing variations for the kepler contact binaries. *The Astrophysical Journal*, 774(1):81, 2013.

R Tylenda, M Hajduk, T Kamiński, A Udalski, I Soszyński, MK Szymański, M Kubiak, G Pietrzynski, R Poleski, K Ulaczyk, et al. V1309 scorpii: merger of a contact binary. *Astronomy & Astrophysics*, 528:A114, 2011.

W Van Hamme and RE Wilson. A contribution on the problem of empirical masses for contact binaries. *Astronomy and Astrophysics*, 152:25–32, 1985.

Jake Vanderplas. gatspy: General tools for astronomical time series in python, 2015. URL <http://dx.doi.org/10.5281/zenodo.14833>.

F Vilardell, I Ribas, and C Jordi. Eclipsing binaries suitable for distance determination in the andromeda galaxy. *Astronomy & Astrophysics*, 459(1):321–331, 2006.

Osmi Vilhu and Frederick M Walter. Chromospheric-coronal activity at saturated levels. *The Astrophysical Journal*, 321:958–966, 1987.

Osmi Vilhu, Jean-Pierre Caillault, and John Heise. Simultaneous exosat and vla observations of the contact binaries vw cephei and xy leonis-quiescent emission and a flare on vw cephei. *The Astrophysical Journal*, 330:922–927, 1988.

RF Webbink. Contact binaries. In *3D Stellar Evolution*, volume 293, page 76, 2003.

RE Wilson. Binary star morphology and the name overcontact. *Information Bulletin on Variable Stars*, 2001.

Robert E Wilson and Edward J Devinney. Realization of accurate close-binary light curves: application to mr cygni. *The Astrophysical Journal*, 166:605, 1971.

Y-G Yang, S-B Qian, and B Soonthornthum. Deep, low-mass ratio overcontact binary systems. xii. ck bootis with possible cyclic magnetic activity and additional companion. *The Astronomical Journal*, 143(5):122, 2012.

Mutlu Yıldız and T Doğan. On the origin of w uma type contact binaries—a new method for computation of initial masses. *Monthly Notices of the Royal Astronomical Society*, page stt028, 2013.

Donald G York, J Adelman, John E Anderson Jr, Scott F Anderson, James Annis, Neta A Bahcall, JA Bakken, Robert Barkhouser, Steven Bastian, Eileen Berman, et al. The Sloan digital sky survey: Technical summary. *The Astronomical Journal*, 120(3):1579, 2000.

FZ Zeraatgari, A Abedi, M Farshad, M Ebadian, N Riazi, J Nedoroščík, M Vaňko, T Pribulla, D Kjurkchieva, V Popov, et al. Neural network analysis of w uma eclipsing binaries. *Contrib. Astron. Obs. Skalnaté Pleso*, 45:5–16, 2015.

XB Zhang and RX Zhang. Long-term photometric study of the w uma binary star v523 cas. *Monthly Notices of the Royal Astronomical Society*, 347(1):307–315, 2004.

M Zhao, D Gies, JD Monnier, N Thureau, E Pedretti, F Baron, A Merand, T Ten Brummelaar, H McAlister, ST Ridgway, et al. First resolved images of the eclipsing and interacting binary  $\beta$  lyrae. *The Astrophysical Journal Letters*, 684(2):L95, 2008.